Search for Stable Stau Production at the LHC

Dissertation
zur Erlangung des Doktorgrades
des Department Physik
der Universität Hamburg

vorgelegt von
Kolja Kaschube
aus Wunstorf

Hamburg
2011

Gutachter der Dissertation:	Prof. Dr. Peter Schleper Prof. Dr. Johannes Haller
Gutachter der Disputation:	Prof. Dr. Peter Schleper Dr. Jenny List
Datum der Disputation:	22. September 2011
Vorsitzender des Prüfungsausschusses:	Dr. Georg Steinbrück
Vorsitzender des Promotionsausschusses:	Prof. Dr. Peter Hauschildt
Dekan der MIN-Fakultät:	Prof. Dr. Heinrich Graener

Abstract

In this thesis, a search for heavy stable charged particle production, in particular a quasi-stable supersymmetric tau lepton ("stau") arising in gauge-mediated supersymmetry breaking (GMSB) models, is presented. This stable stau would cross detectors without decaying, resembling a muon, and produce signatures of high momentum or high ionization energy loss. The energy loss measurement represents a direct handle on the particle mass via the Bethe-Bloch formula. Proton-proton collisions at 7 TeV center-of-mass energy produced by the Large Hadron Collider and recorded by the CMS detector are investigated. Low-momentum collision data tracks are used to predict the background of highly ionizing tracks at high momenta. A high signal-to-background ratio is achieved by separating the search into channels with differing muon or stau multiplicities and by using the transverse momentum and energy loss measurement as the discriminating variables. Using 35.8 pb^{-1} of data recorded in the 2010 LHC run, no excess is observed with respect to the expected Standard Model background. As a result, upper limits on the mass of stable staus are derived within the context of the investigated GMSB models.

Zusammenfassung

In dieser Arbeit wird die Suche nach neuen schweren stabilen geladenen Teilchen, genauer gesagt einem quasi-stabilen supersymmetrischen Tau-Lepton ("Stau"), das in Gauge-Mediated Supersymmetry Breaking (GMSB) Modellen vorhergesagt wird, präsentiert. Dieses stabile Stau durchdringt Detektoren ohne zu zerfallen, ähnlich einem Myon, und hat dabei großen Impuls oder großen Energieverlust durch Ionisation. Die Energieverlustmessung ermöglicht eine direkte Bestimmung der Masse eines Teilchens über die Bethe-Bloch-Formel. Untersucht werden Proton-Proton-Kollisionen mit einer Schwerpunktsenergie von 7 TeV, die vom Large Hadron Collider produziert und vom CMS-Detektor aufgenommen wurden. Teilchenspuren mit niedrigen Impulsen aus Kollisionsdaten werden verwendet, um den Untergrund von Spuren mit hohem Energieverlust bei hohen Impulsen vorherzusagen. Ein gutes Signal-zu-Untergrund-Verhältnis wird erzielt, indem die Suche nach Myon- oder Stau-Multiplizität unterteilt wird und entweder der Transversalimpuls oder der Energieverlust durch Ionisation als diskriminierende Observable verwendet wird. Mit einer Datenmenge von 35.8 pb^{-1}, aufgenommen zwischen März und November 2010, wird kein Überschuss in den Daten gegenüber dem erwarteten Untergrund aus dem Standard-Modell beobachtet. Daher werden obere Grenzen auf die Masse des stabilen Staus im Zusammenhang mit den untersuchten GMSB-Modellen abgeleitet.

Contents

1 Introduction **3**

2 Theoretical Background **5**

2.1 Standard Model of Particle Physics 5

2.1.1 Particles and Forces 5

2.1.2 Gauge Theories and Couplings 11

2.1.3 Beyond the Standard Model 12

2.2 Cross Sections 13

2.3 Proton-Proton Scattering at the LHC 16

2.4 Supersymmetry 19

2.5 Quasi-stable Stau in GMSB 22

2.6 Heavy Stable Charged Particles 26

3 The CMS Experiment at the LHC **29**

3.1 The Large Hadron Collider 29

3.2 The Compact Muon Solenoid Experiment 30

3.2.1 Silicon Tracker 31

3.2.2 Electromagnetic Calorimeter 36

3.2.3 Hadronic Calorimeter 37

3.2.4 Superconducting Magnet 40

3.2.5 Muon System 40

3.2.6 Trigger System 43

3.2.7 Luminosity Monitoring 43

4 Event Simulation and Reconstruction **45**
4.1 Event & Detector Simulation . . . 45
4.2 Physics Object Reconstruction . . . 46
4.2.1 Hits, Tracks, and Energy Loss . . . 47
4.2.2 Muons . . . 49
4.2.3 Jets . . . 50
4.2.4 Missing Transverse Energy . . . 52
4.2.5 Software . . . 52

5 Stable Stau Search **53**
5.1 Stable Stau Signal in CMS . . . 53
5.2 Standard Model Backgrounds . . . 56
5.3 Datasets . . . 57
5.4 Event Selection . . . 59
5.4.1 Triggers . . . 60
5.4.2 Primary Vertex . . . 60
5.4.3 Muons . . . 62
5.4.4 Jets . . . 66
5.4.5 Control Selection . . . 67
5.5 dE/dx Background Estimation from Data . . . 75
5.6 Final Selection . . . 82
5.6.1 Single-muon Channel . . . 82
5.6.2 Multi-muon Channel . . . 88
5.6.3 Discussion of Results . . . 95

6 Systematic Uncertainties **97**
6.1 Experimental Uncertainties . . . 97
6.2 Signal Prediction Uncertainties . . . 98
6.3 Background Prediction Uncertainties . . . 101
6.4 Total Systematic Errors . . . 103

7 Results **105**

8 Conclusion **109**

A CLs Method **113**

B GMSB Mass Spectra **115**

Bibliography **132**

Chapter 1

Introduction

The field of high-energy physics is at a crossroads. Two of the most important theories of particle physics proposed in the early second half of last century, the electroweak theory and quantum chromodynamics, have been tested and confirmed time and again by high-energy physics (HEP) experiments. There is now a great understanding of *what is known*. The final missing piece of the Standard Model of particle physics, the Higgs boson, may be on the verge of being discovered at the Large Hadron Collider (LHC). But what comes next? The big looming questions in particle physics concern *the unknown*. What is the nature of dark matter, making up about 25 % of the universe's energy density? Is there a single, unified force at very high energies? Which role does gravity play at those energies? These questions seem to be inaccessible with the experimentally confirmed theory of particle physics. A large array of theories beyond the Standard Model (SM) have been devised, and the search for new phenomena is at the center of the LHC experiments' physics programs. The biggest question is certainly whether new phenomena show up at the energies probed at the LHC. If not, will it be possible to increase the energy of colliders beyond the TeV level in the near future or will other ways of detecting heavy particles have to be utilized? Or will precision measurements of properties such as CP-violation unveil more about the nature of the universe? If so, can the data be interpreted in a meaningful way or will new experiments be necessary for a good understanding of physics beyond the Standard Model? Obviously, the road that will be taken in the near future depends very much on the outcome of observations made at the Large Hadron Collider.

In this work, the data of the CMS experiment at the LHC are scoured for new, heavy, leptonic particles that may give an indirect hint at the composition of dark matter. These

heavy stable charged particles (HSCPs) are introduced in the supersymmetric extension of the SM, with the model of gauge-mediated supersymmetry breaking (GMSB) prescribing the complete phenomenology. The lightest supersymmetric particle (LSP) in these models is always a gravitino, the superpartner of the graviton. The gravitino is a suitable candidate for cold dark matter, but it is undetectable by collider experiments because it only interacts gravitationally. On the other hand, the next-to-lightest supersymmetric particle (NLSP) can be a stable, scalar tau lepton ("stau") having a mass of 100 or more GeV, depending on the parameters of the GMSB model. In R-parity conserving models, the NLSP will always decay into the gravitino, but depending on the model parameters, the lifetime of NLSP can be arbitrarily high. Therefore, the stable stau is the subject of this search. Stable staus do not invoke electromagnetic of hadronic showers but, unlike muons, possibly leave large deposits of ionization energy loss in the silicon detectors of the inner tracker while having momenta of over 100 GeV. In the SM, the signature of high energy loss (dE/dx) is only expected at particle energies of below a few GeV; therefore the dE/dx measurement is a great observable for new physics searches.

The data analyzed correspond to 35.8 pb^{-1} of proton-proton collisions produced by the LHC in 2010. Events with highly energetic muon candidates and at least two well-measured hadronic jets are compared with simulations of SM and GMSB processes in order to search for stable stau leptons. Observed energy loss and transverse momentum distributions of muon candidates are investigated and compared with the expectations from the SM and GMSB processes. Muon candidates having either high momentum or high energy loss will be stau candidates, leading to further investigation. The analysis is performed in three different search channels depending on the number of muon candidates in the final state in order to optimize the signal-to-background ratio.

This thesis continues with an overview of theoretical fundamentals in Chapter 2, where the Standard Model and supersymmetry are introduced from a phenomenological perspective. The experimental setup, being the LHC and the CMS experiment, is described in Chapter 3. Aspects of the simulation and reconstruction of proton-proton collisions with the CMS detector are outlined in Chapter 4. In Chapter 5, the selection of collision events with signatures of stable charged leptonic particles is presented in detail, followed by a discussion of systematic uncertainties in Chapter 6. An interpretation of the results from the analysis presented in the preceeding two chapters is given in Chapter 7. The thesis closes with a summary and concluding remarks in Chapter 8.

Chapter 2

Theoretical Background

In this chapter, the theoretical framework needed to understand the possible origin and phenomenology of new, heavy particles is introduced. Beginning with a phenomenological overview of the Standard Model of particle physics, the concepts of gauge theories and interaction rates are discussed. Then, the supersymmetric expansion of the Standard Model is outlined, followed by the model of gauge-mediated supersymmetry breaking (GMSB) which gives rise to a quasi-stable scalar τ lepton. This particle is classified as a heavy stable charged particle (HSCP), the experimental implications of which are explained in the closing section of this chapter.

2.1 Standard Model of Particle Physics

The Standard Model (SM) of particle physics comprises the mathematical description of the interactions and properties of the known elementary particles.

2.1.1 Particles and Forces

Particles that visible matter is made of are fermions, meaning they have half-integer spin and obey the Fermi-Dirac statistical principle which implies that in a quantum-mechanical system (such as an atom), no two fermions can occupy the same state. The interactions of fermions are mediated by bosonic particles having integer spin. Possible interactions of a particle depend on its mass and a number of conserved properties such as total spin, electric charge, color charge, and weak isospin. Particles with an electric charge underlie

the electromagnetic force which is transferred by the photon, while particles with color charge underlie the strong interaction, mediated by the gluon. All fermions have weak isospin and partake in the weak interaction, which is carried by the massive $W^{\pm}$ and Z^0 bosons [1].

Fermions are divided into two classes: leptons, one of which is the electron, and quarks, which carry color charge. All leptons and quarks are thought to be point-like particles, and at best, only upper limits on the size of these particles have been established. There are three charged leptons with differing masses, the electron (e), muon (μ), and tau (τ), which are grouped with a neutrino partner (ν_e, ν_μ, and ν_τ, respectively) into a generation. Neutrinos are stable and electrically neutral, meaning they only participate in the weak interaction. They have very small masses which as yet have not been measured experimentally [2][1]. The six quarks (u, d, c, s, t, b) carry both electric and color charge. Being the only known particles with fractional charges, three quarks have electric charge $q = +\frac{2}{3}$ while the other three have $q = -\frac{1}{3}$. Two quarks with differing charges form a generation and each generation contains lighter quarks than the next one.

The three fundamental forces are described by *gauge theories* which rely on the principle that they are invariant under local transformations, as explained in the next section. The consequence of this is that the quantum number associated with a force (e.g. electric charge for the electromagnetic force) is a conserved quantity.

The electromagnetic force is carried by the massless, spin-1 photon and therefore has infinite reach. Furthermore, photons have no $flavor$, meaning they cannot change the particle type of a particle they interact with.

The weak interaction governs the decay of fermions, which is the reason behind the sorting of particles into generations. In analogy to the electric charge, the weak isospin I_3 determines how a particle participates in the weak interaction. Weak isospin depends on the helicity-configuration of a particle: in the limit of infinite momentum, fermions have two spin-configurations with respect to their direction of flight, parallel and anti-parallel, which are called right- and left-handed (R, L) helicity states, respectively. The left-handed partners of one generation form a *weak isodoublet* and have $I_3 = +1/2$ and $I_3 = -1/2$, respectively, as shown in Tab. 2.1. Apparently, right-handed fermions have $I_3 = 0$, since

[1]Neutrino oscillations - in-flight change of lepton flavor - have been observed, putting upper limits on neutrino masses of a few eV. For measurements at colliders, it is acceptable to set the neutrino masses to zero.

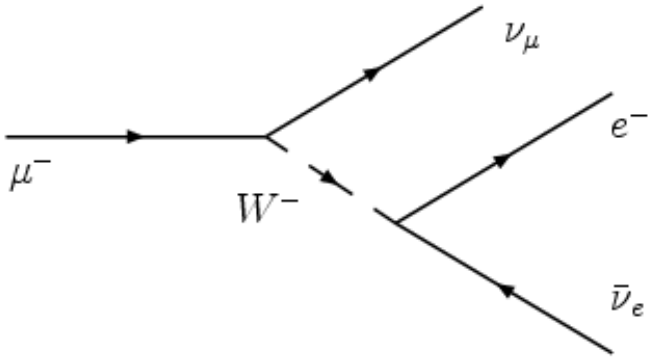

Figure 2.1: Feynman diagram of the muon decay at leading order.

no weak interactions involving this helicity state have been observed. Thus, right-handed fermions are isospin singlets. Weak isospin is conserved in all interactions [1].

Charged leptons decay by emitting a virtual W boson while simultaneously being converted into their neutrino partner. The produced W decays into other particles whose combined mass cannot exceed the mass of the original decaying lepton. A diagram of the decay of a muon is shown in Fig. 2.1. The lightest charged lepton, the electron, cannot decay because there are no lighter charged particles into which the W could decay. This, coupled with the conservation of electric charge, is the reason that the electron is stable. For quarks, flavor is not conserved in weak decays which means that no quark is stable, except for the lightest one, the up-quark. The likelihoods for flavor-changing quark decays have been measured experimentally and are summarized in the CKM-Matrix. Furthermore, there are no vertices converting leptons into quarks and vice versa in the SM. This means that the total lepton (L) and baryon (B) numbers are unchanged in any interaction [1]. All quarks have baryon number 1/3 for reasons explained below.

Due to the high mass of the $W^{\pm}$ of 80.4 GeV, which exceeds the mass of, for instance, the muon by many orders of magnitude, the latter's conversion into W and ν_μ violates energy-momentum conservation. According to Heisenberg's uncertainty principle, this is possible for a very short time $t \sim \hbar/\Delta E$ after which the W must decay into lighter particles. With $\Delta E \sim M_X c^2$ for a particle with mass M_X, the range of the exchanged particle is approximately $r \sim \hbar/M_X c$, which is about 10^{-18} m for the W boson. This is a very short distance compared to the approximate size of a proton of 10^{-15} m. In addition to the charged W bosons, the weak interaction is mediated by the neutral Z^0 boson, which has a mass of 91.2 GeV. The Z^0 gives rise to interactions of neutrinos in which the neutrino

Fermion Generations			I_3
e_L^-	μ_L^-	τ_L^-	-1/2
$\nu_{e,L}$	$\nu_{\mu,L}$	$\nu_{\tau,L}$	+1/2
u_L	c_L	t_L	+1/2
d_L	s_L	b_L	-1/2
e_R^-	μ_R^-	τ_R^-	0
$\nu_{e,R}$	$\nu_{\mu,R}$	$\nu_{\tau,R}$	0
u_R	c_R	t_R	0
d_R	s_R	b_R	0

Table 2.1: Weak isospin I_3 of Standard Model fermions. Antiparticles have opposite values of isospin.

does not change into its charged leptonic partner. However, this is highly unlikely at neutrino energies below the mass of the Z boson. Furthermore, all interactions in which a photon is exchanged can in principle also be mediated by the Z^0, because all fermions participate in the weak interaction. These interactions cannot be distinguished, although the contribution of the Z^0 becomes relevant only at center-of-mass energies close to the Z^0 mass. Thus, at such energies, the electromagnetic and weak interaction unify into the *electroweak interaction*.

Quarks also carry color charge, making them subject to the strong interaction, which is mediated by the massless, electrically neutral gluon. In contrast to the photon, which itself is neutral with respect to the conserved quantity it couples to (electric charge), gluons have color - the conserved quantity of the strong interaction - causing them to interact with other gluons [1]. The dynamics of color exchange are described by *quantum chromodynamics*, a gauge theory built around three color states, called R, G, and B (red, green, blue). Quarks have one color and anti-quarks (denoted $\bar{q}$) have an anti-color ($\bar{R}$, $\bar{G}$, or $\bar{B}$). Quarks can change color by interacting with a gluon which carries one color and one anti-color. The three colors and anti-colors lead to eight physical gluon states, six of which have net color (e.g. $R\bar{B}$), while the other two are linear superpositions of the color-neutral states $R\bar{R}$, $G\bar{G}$, and $B\bar{B}$. Analogous to photons in QED, gluons are flavor-neutral with respect to quarks, meaning that the six quarks have a common coupling strength to gluons and that strong interactions do not change the flavor of quarks [1].

The self-interaction of gluons is the reason behind the phenomenon of confinement which affects colored particles. As the distance between two colored particles increases, the force between them increases, as well[2]. Phenomenologically, this can be explained with an increasing number of higher-order gluon interactions taking place, thereby "gluing" the particles together. At a certain distance between two colored particles, it is energetically favorable to create a pair of quarks in between them such that the potential energy of the system decreases. This process is known as the *fragmentation* of colored particles. Furthermore, no colored states have ever been observed in nature, leading to the notion that quarks and gluons *hadronize* to form composite particles called *hadrons*, which are bound states of quarks [1].

Two types of hadrons are known: *mesons*, which consist of a quark and an anti-quark, and *baryons*, which consist of three quarks[3]. Mesons have spin 0, baryon number 0, and are unstable since quarks decay weakly into lighter quarks until the u-quark is reached. The lightest meson, the π^0 ($u\bar{u}$), can decay electromagnetically into two photons. Thus, there are no stable mesons. The lightest baryon is the proton, a bound state of two u-quarks and one d-quark, which is stable[4]. Its partner in atomic nuclei, the neutron (udd), has a finite lifetime of about 15 minutes when it is free, i.e. not bound in an atomic nucleus. Baryons are fermions with spin 1/2 and baryon number 1. Baryons with heavy quarks are unstable for the same reason as mesons. Many excited states of mesons and baryons exist, which are usually very short-lived as they can decay via the strong interaction into their ground states. Besides being color-neutral, all hadrons have integer electric charges. The fact that only multiples of the elementary charge $e = 1.6 \times 10^{-19}$ C have been observed experimentally is another indication that free quarks do not exist in nature. The fragmentation and hadronization processes have not been quantified by perturbation theory and existing models have been tuned to the observed hadronization products measured by experiments.

The heaviest quark, the top, has a special position among quarks in so far that it has not been observed in a bound hadronic state. The reason for this is its high mass: the top-quark decays into a b-quark and a W boson with a mean lifetime of $\lesssim 5 \cdot 10^{-25}$ s, which

[2]The weak gauge bosons W and Z also self-interact, but due to their high masses there is no confining effect in the weak interaction.

[3]Searches for *pentaquarks*, bound states of five quarks, have all been negative [2].

[4]The uuu-state, Δ^{++}, has spin 3/2, charge 2, and a mass of 1.23 GeV. It decays into a proton and a pion.

Particle	Mass [GeV]	Charge	Spin	Mean lifetime [s]
e^-	$5.11 \cdot 10^{-4}$	-1	1/2	stable
ν_e	≈ 0	0	1/2	stable
μ^-	0.106	-1	1/2	$2.2 \cdot 10^{-6}$
ν_μ	≈ 0	0	1/2	stable
τ^-	1.78	-1	1/2	$2.9 \cdot 10^{-13}$
ν_τ	≈ 0	0	1/2	stable
u	$\approx 2.4 \cdot 10^{-3}$	2/3	1/2	hadronize
d	$\approx 4.8 \cdot 10^{-3}$	-1/3	1/2	hadronize
c	≈ 1.3	2/3	1/2	hadronize
s	≈ 0.1	-1/3	1/2	hadronize
t	172	2/3	1/2	$< 5 \cdot 10^{-25}$
b	≈ 4.2	-1/3	1/2	hadronize
γ	0	0	1	stable
$W^\pm$	80.4	± 1	1	$3.1 \cdot 10^{-25}$
Z^0	91.2	0	1	$2.6 \cdot 10^{-25}$
g	0	0	1	hadronize

Table 2.2: Particle content of the Standard Model. All numbers taken from [2].

is apparently shorter than the fragmentation and hadronization processes lasting around 10^{-23} s [3].

The intrinsic properties of all known SM particles are listed in Tab. 2.2. Neutrino masses are set to zero for the purpose of this work. Not included in the particle table is the last missing piece of the Standard Model, the Higgs boson. The process of electroweak symmetry breaking gives masses to the weak gauge bosons and introduces a massive, neutral, spin-0 particle, the Higgs boson. This *Higgs-mechanism* is accepted widely in the particle physics community, therefore the Higgs boson is considered part of the SM. Through Yukawa couplings which are proportional to mass, the interaction of particles with the Higgs is thought to be the origin of their masses. Experimental searches for the Higgs boson have failed so far, excluding masses below 114.4 GeV [4] and between 158 and 173 GeV [5] at 95 % confidence level.

2.1.2 Gauge Theories and Couplings

The kinematics of relativistic elementary particles are described by quantum field theory. The equation of motion for fermions is the Dirac equation

$$(\gamma^\mu \partial_\mu - m)\,\psi = 0 \tag{2.1}$$

where a fermion with mass m is assigned a wave function $\psi = Ne^{-\mathrm{i}px}$ which depends on its four-momentum p, space-time position x, and an unspecified normalization factor N [3]. The momentum operator ∂_μ is the covariant space-time derivative, making Eq. 2.1 an energy-momentum relation for relativistic fermions[5]. An external force, or "perturbation", acting on the particle is introduced by adding potential terms $V(x)$ to Eq. 2.1, such that

$$(\gamma^\mu \partial_\mu - m - V(x))\,\psi = 0. \tag{2.2}$$

Each of the three fundamental interactions introduces different potential terms that act on particles in a distinct way. While the explicit potential terms will not be discussed here it is important to note that the choice (or 'gauge') of the potential $V(x)$ should not change the validity of Eq. 2.2. Substituting $V(x)$ for

$$V'(x) = V(x) + \frac{\partial}{\partial x} f(x), \tag{2.3}$$

where $f(x)$ is an arbitrary scalar function, leaves Eq. 2.2 invariant if the fermion wave function ψ is simultaneously transformed such that

$$\psi' = e^{iqf(x)}\,\psi, \tag{2.4}$$

where q is a conserved quantity to which the potential $V(x)$ couples. Theories for which the local transformations[6] (2.3) and (2.4) keep Eq. 2.2 valid are called *gauge theories*. Each of the three fundamental forces discussed in the previous section is described by a gauge theory: quantum electrodynamics (QED) for the electromagnetic force, where q is the electric charge; electroweak theory, where q is the weak isospin; and quantum chromodynamics (QCD), where q is the color-charge.

The coupling strength α_i $(i = 1, 2, 3)$ of each interaction is common to all interactions of its type. However, additional fermion or boson loops, shown in Fig. 2.2, in an interaction cannot be measured directly since only the initial and final states are accessible

[5] Four-vector notation: $x = (t, x, y, z)$, $p = (E, p_x, p_y, p_z)$.

[6] These transformations are called *local* because they depend on the space-time position x.

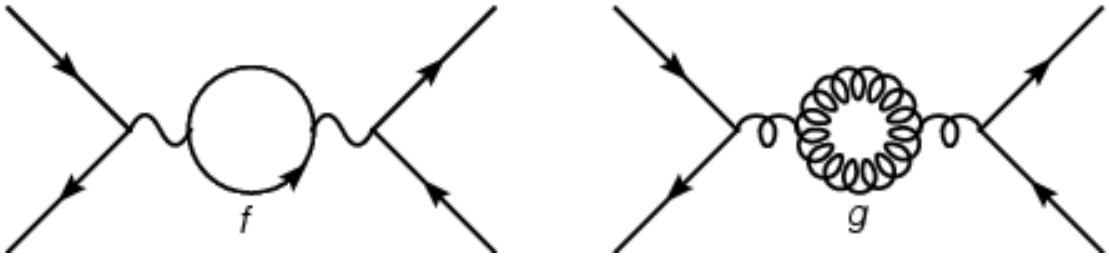

Figure 2.2: Feynman diagrams of fermion and boson loop corrections.

experimentally. These higher order corrections do not significantly change the final state, though, and can be "absorbed" by the couplings α_i. As the initial state energy increases, the probability of higher order corrections increases, leading to an energy dependence of the couplings. This is called *renormalization* of the couplings.

2.1.3 Beyond the Standard Model

Although the Standard Model, excluding the Higgs boson, has been measured and verified by many experiments, there are several issues that are not covered or addressed satisfactorily by the theory.

A purely theoretical problem is the lack of a quantum theory of gravitation, which would complete the SM in its description of all fundamental forces of nature. The exchange of gravitation is thought to be mediated by a massless spin-2 boson, called *graviton*. The effect of gravitation of course depends on the masses of the interacting particles. For elementary particles, gravitation becomes relevant (i.e. the coupling strength of gravitation becomes roughly as large as that of the other three forces) only at the Planck scale of about 10^{19} GeV.

A unified theory describing all forces at some high energy scale is also precluded by the present structure of the SM. The three gauge couplings do not converge at a common value up to energies of about 10^{16} GeV [3]. However, the extrapolation of the couplings assumes that the particle content is exactly that of the SM and that no new particles arise at energies between the electroweak scale ($\simeq$ 100 GeV) and 10^{16} GeV, spanning about fourteen orders of magnitude. The latter seems to be an unlikely proposition in itself and it referred to as the *hierarchy problem*.

Cosmological observations show that only slightly less than five percent of the total en-

ergy density of the universe comes from baryonic matter. Meanwhile, about 23 % should come from as yet unobserved, gravitationally interacting "dark" matter, whereas the remaining 72 % originate from some unknown source, called "dark energy". The SM does not offer any solution towards the nature of dark matter and dark energy [3].

The so-called *fine tuning problem* concerns fermion-loop corrections to the Higgs mass, which depend quadratically on the energy scale Λ at which they arise:

$$m_H^2 \simeq m_{H,0}^2 - \frac{\lambda_f^2}{8\pi^2}\Lambda^2, \tag{2.5}$$

where $m_{H,0}$ is the uncorrected Higgs mass, and λ_f is the Yukawa coupling of a fermion to the Higgs. Assuming that the SM should be correct up to the GUT scale ($\Lambda \simeq 10^{16}$ GeV), along with a physical Higgs mass of around $m_H = 100$ GeV, leads to the necessity of knowing the bare Higgs mass with a relative accuracy of 10^{-26} [3]. This fine-tuning is a very artificial solution that seems to be highly improbable.

Many extensions and modifications of the SM have been brought forth in order to solve its shortcomings, but none have been verified experimentally so far. The most studied and detailed extension to the SM is called supersymmetry (SUSY). It addresses some of the aforementioned problems by introducing a plethora of new particles while keeping the structure of the SM intact. These aspects are discussed in later sections of this chapter.

2.2 Cross Sections

The interaction of two particles depends on their momenta and spins, as well as on their gauge quantum numbers, electric charge, weak isospin, and color charge. The exchange of these properties between the two particles is carried by a gauge boson of the corresponding interaction. A Feynman diagram of electron-electron scattering is shown in Fig. 2.3, where the exchanged particle can be either a photon or a Z^0. The second figure shows the annihilation and subsequent production of e^+ and e^-, a process which is possible for two particles with opposite electrical charges but otherwise identical quantum numbers. The scattering diagram is called t-channel while the annihilation is called s-channel. A third process, called u-channel, exists where the outgoing particles exchange places. These three processes comprise all possible elastic[7] interactions of oppositely charged electrons

[7]Elastic refers to unchanged particles between the initial and final state. Inelastic interactions change the particle type and/or number.

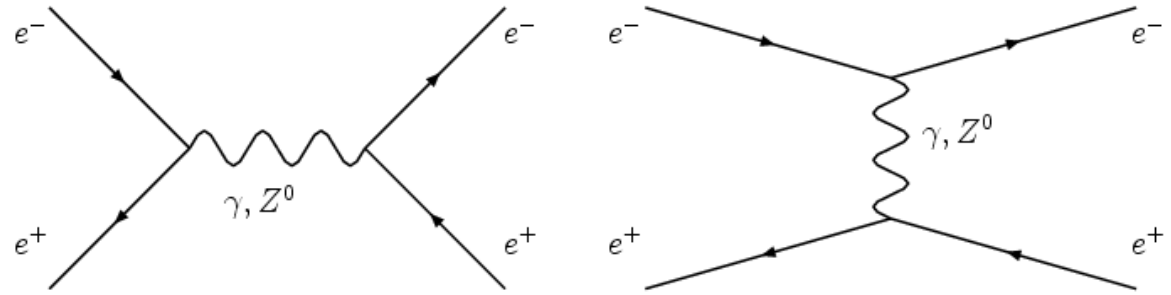

Figure 2.3: Feynman diagrams of e^+e^- interactions: annihilation (left) and scattering (right) at lowest order. Time advances from left to right.

at leading order. Higher orders include additional boson radiation or loops at any time in the process. The corresponding diagrams for quarks are identical except for the added possibility of gluon exchange instead of a photon or a Z-boson, because quarks participate in all interactions.

The transition of an initial particle state into a state after an interaction with another particle is quantified by the *scattering amplitude*. Let us assume one particle with an initial state $\psi_i = Ne^{-\mathrm{i}p_i x}$ interacts with a potential $V(x)$ which is caused by another particle that is at rest, then the transition rate to a final state $\psi_f = Ne^{-\mathrm{i}p_i x}$ is approximated by

$$\mathrm{d}N_f = N^2 \rho(p_f) | \int \mathrm{d}^4 p \, \psi_f^* \, V(x) \psi_i |^2, \tag{2.6}$$

where $\rho(p_f)$ is the density of possible final states, which depends on the spins and momenta of the scattered particles. Equation 2.6 represents the *Born approximation*, the quantum-mechanical transition rate at leading order in perturbation theory [1]. Substituting the initial and final state wave functions of our relativistic particle leads to

$$\mathrm{d}N_f = N^2 \rho(p_f) | \int \mathrm{d}^4 p \, V(x) e^{i(p_i - p_f)x} |^2, \tag{2.7}$$

which can be written as

$$\mathrm{d}N_f = N^2 \rho(p_f) |M_{if}|^2, \tag{2.8}$$

where the scattering amplitude M_{if} is given by

$$M_{if} = \int \mathrm{d}^4 p V(x) e^{i(p_i - p_f)x}. \tag{2.9}$$

The reaction rate of any process into a an element of the solid angle $\mathrm{d}\Omega = \mathrm{d}\cos\Theta \mathrm{d}\phi$ is given by the *differential cross section*

$$\frac{\mathrm{d}\sigma}{\mathrm{d}\Omega}. \tag{2.10}$$

The differential cross section for an energetic particle interacting with a particle at rest is given by

$$\frac{\mathrm{d}\sigma}{\mathrm{d}\Omega} = \frac{1}{64\pi^2 s}\frac{|p_i|}{|p_f|}\bar{\Sigma}|M_{if}|^2, \tag{2.11}$$

where s is the squared center-of-mass energy of the interacting particles [3], and $\bar{\Sigma}|M_{if}|^2$ is the sum of all possible final spin states, averaged for all possible initial spin states[8] [1].

In an experimental setup with incoming particles that have a flux $J = n_i v_i$, where n_i is the number of incoming particles and v_i is their speed, directed at a target of N stationary particles, the transition rate $\mathrm{d}N_f$ and the cross section are related as follows:

$$\mathrm{d}N_f = JN\frac{\mathrm{d}\sigma}{\mathrm{d}\Omega}\mathrm{d}\Omega. \tag{2.12}$$

The product of J and N is determined by the experimental setup and is called *instantaneous luminosity* $L = JN$. Integrating over the solid angle gives the total cross section of a reaction

$$\sigma = \frac{\mathrm{d}N_f}{L}. \tag{2.13}$$

The exact calculation of the the scattering amplitude M_{if} and thus transition rate $\mathrm{d}N_f$ is usually performed by sophisticated programs at up to next-to-next-to-leading order (NNLO) for scattering processes of two particles.

Depending on the center-of-mass energy $\sqrt{s}$ of an initial state, many final states are possible. If decaying particles are produced in the interaction, each decay mode of a heavy particle has a certain probability, called *branching fraction*, depending on the masses and quantum numbers of the decay products. For each subprocess, a cross section can be defined by multiplying its branching fraction with the total cross section of an initial state. Picking up the previous example of $\mathrm{e^+e^-}$-scattering, the s-channel diagram from Fig. 2.3 can be extended to include any two fermions of the same flavor in the final state as long as $\sqrt{s}$ exceeds the combined mass of the produced fermion pair. Pairs of W bosons may be produced as well, leading to a myriad of possible final states at high center-of-mass energies.

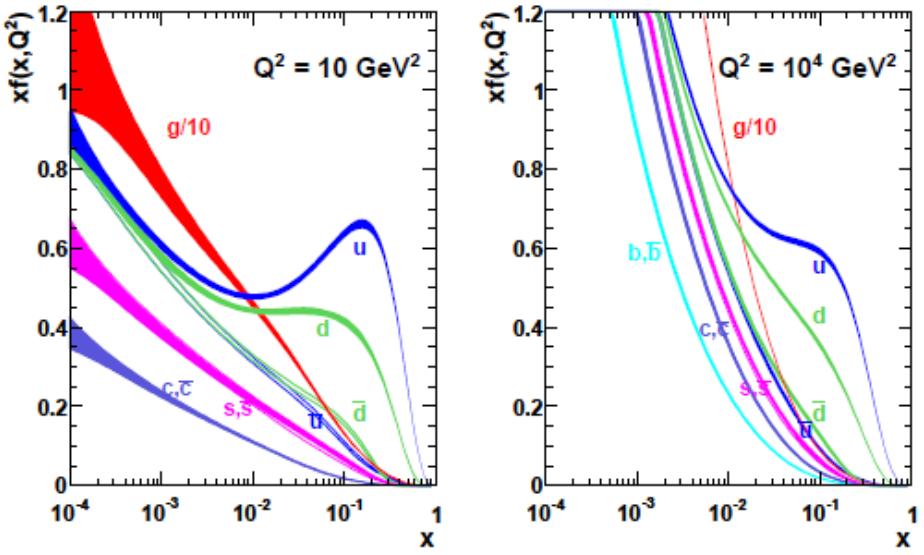

Figure 2.4: Parton distribution functions versus momentum fraction x at $Q^2 = 10$ GeV^2 (left) and 10^4 GeV^2 (right) with one-sigma uncertainties. Gluon PDFs are downscaled by a factor of 10 for visibility. From [6].

2.3 Proton-Proton Scattering at the LHC

Although the quantum numbers of the proton correspond to two u quarks and one d quark, these *valence* quarks are bound by gluons. As the kinetic energy of a proton increases, so does the energy of the valence quarks, making gluon radiation more likely. Furthermore, the radiated gluons become more energetic, making quark loops (called *sea* quarks) more likely, and thus the effect of creating additional particles inside the proton enhances. This means that at high energies, the proton consists of many more particles (called *partons*) than just the three valence quarks. When two protons collide, usually only one parton of each proton enters the hard interaction, whereas the remnants keep moving relatively unchanged. Each parton carries a fraction x of the total proton momentum before the interaction. On average, this fraction differs for valence quarks, sea quarks, and gluons inside the proton, as shown in Fig. 2.4. The curves shown in this plot for different types of partons are called *parton density functions* (PDFs), which give a likelihood of which particle enters the hard interaction as a function of the parton momentum fraction x, and

[8] Averaging over the initial spins is necessary if the initial state spins are unknown, as is the case at the LHC.

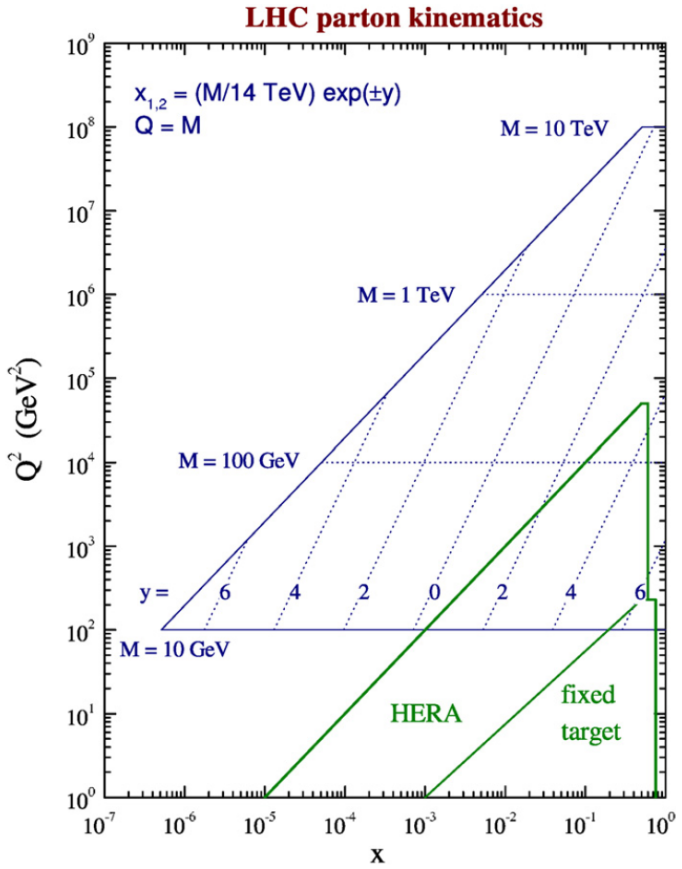

Figure 2.5: Relationship between momentum transfer Q^2 and momentum fraction x and corresponding mass M of particles produced at rapidity y. The range of the LHC at $\sqrt{s} = 14$ TeV is shown in blue and compared to HERA and fixed target kinematics. From [7].

the energy transfer of the hard interaction, $Q = p_1 - p_2$, for two incoming partons with four-momenta $p_{1,2}$. At high x, the valence quarks (u, d) are most likely to enter the interaction, while gluons and sea quarks are very unlikely to have such high momentum fractions. Below $x \approx 0.1$, gluons are the dominant partons. At high Q^2, the contribution of gluons and sea quarks becomes larger, and the steep curves of u and d represent predominantly sea quarks at values of x below circa 0.1.

At high proton energies such as those realized at the LHC, the probed values of x can be as low as 10^{-6}, as shown in Fig. 2.5. Consequently, the probability to have two gluons in the hard interaction is very large at the LHC. The momentum transfer Q^2 can be as high as 10^8 GeV^2 at the LHC design energy of 7 TeV per beam [7].

The cross sections for a selection of SM processes are given as a function of the center-

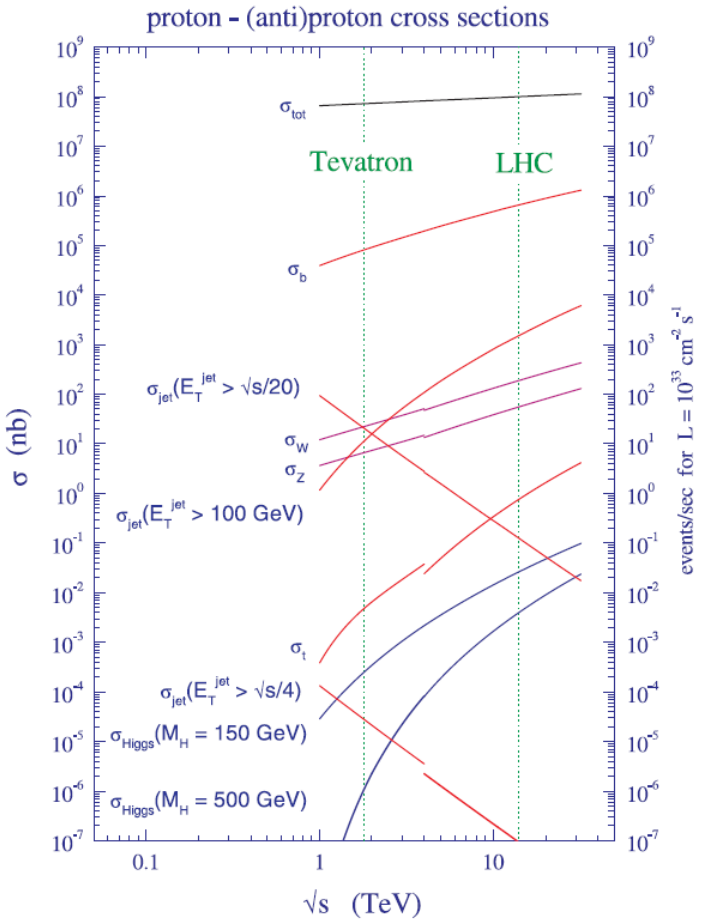

Figure 2.6: Standard Model cross sections and event rates in proton-(anti-)proton collisions as a function of the center-of-mass energy $\sqrt{s}$. The LHC intersect corresponds to $\sqrt{s} = 14$ TeV. From [7].

of-mass energy in Fig. 2.6. The dotted line for the LHC values corresponds to the design energy of $\sqrt{s} = 14$ TeV. The total proton-proton cross section σ_{tot} increases slightly with $\sqrt{s}$, whereas heavy particle production rates increase dramatically [7]. The y-axis on the right side of the plot shows the number of events per second for an instantaneous luminosity of $L = 10^{33}\text{cm}^{-2}\text{s}^{-1}$.

The main processes of quark-pair production at the LHC are shown in Fig. 2.7. The quark annihilation process can also proceed via electroweak boson exchange, although this is suppressed with respect to the QCD process shown. Electroweak processes such as direct lepton or W production can only occur with quarks in the initial state.

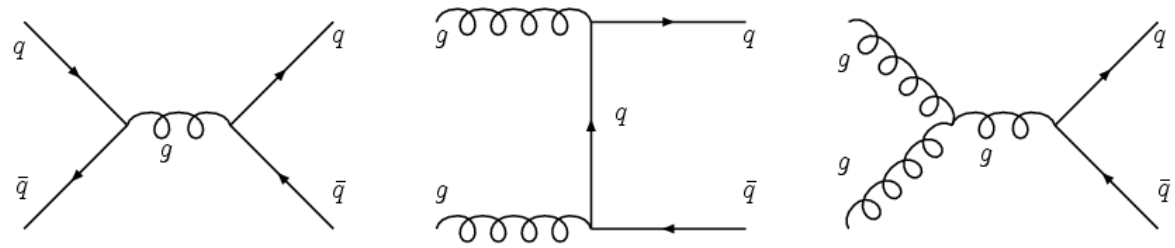

Figure 2.7: Feynman diagrams of quark-antiquark production at leading order at the LHC.

2.4 Supersymmetry

Supersymmetry (SUSY) introduces a new symmetry between fermions and bosons which effectively doubles the known particle spectrum: each Standard Model particle gets a superpartner with exactly the same characteristics except for the spin, which differs by one-half. Mathematically, this is achieved [8, 9, 10] by using an algebra with a generator Q, called *supercharge*, which commutes with the gauge transformations, the Hamiltonian, and the operator of the invariant mass. The irreducible representations of this SUSY algebra, called *supermultiplets*, contain a two-dimensional SM field and the corresponding superfields. A SM fermion has two helicity states (L, R) and gets one scalar (spin 0) superpartner for each state, forming a *chiral* supermultiplet, while a SM vector boson (spin 1) has two helicity states and one fermionic superpartner with again two helicity states, together forming a *gauge* supermultiplet. Each supermultiplet is a four-dimensional vector with two fermionic and two bosonic degrees of freedom. The interactions of the gauge supermultiplet are the SM gauge interactions, whereas the chiral multiplet has new Yukawa couplings [11] which are expressed in a *superpotential* W of the form

$$W = \frac{1}{2}M^{ij}\Phi_i\Phi_j + \frac{1}{6}y^{ijk}\Phi_i\Phi_j\Phi_k, \tag{2.14}$$

where M^{ij} is a symmetric fermion mass matrix, the Φ_i are chiral supermultiplets, and y^{ijk} is a Yukawa coupling of a scalar and two fermions.

The supersymmetric Higgs-sector has to be adjusted such that two Higgs-doublets along with their superpartners are present in chiral supermultiplets. Their scalar components, denoted H_u and H_d, give mass to up-type quarks, and to down-type quarks and charged leptons, respectively [11]. From the total of eight degrees of freedom of the Higgs doublets, three are necessary to give mass to the electroweak gauge bosons via electroweak symmetry

Chiral Supermultiplet Φ	Spinor ψ (spin 1/2)	Scalar ϕ (spin 0)
Q	$(u_L,\, d_L)$	$(\tilde{u}_L,\, \tilde{d}_L)$
$\bar{U}$	$u_R^\dagger$	$\tilde{u}_R^*$
$\bar{D}$	$d_R^\dagger$	$\tilde{d}_R^*$
L	$(\nu_L,\, e_L)$	$(\tilde{\nu}_L,\, \tilde{e}_L)$
$\bar{E}$	$e_R^\dagger$	$\tilde{e}_R^*$
H_u	$(\tilde{H}_u^+,\, \tilde{H}_u^0)$	$(H_u^+,\, H_u^0)$
H_d	$(\tilde{H}_d^0,\, \tilde{H}_d^-)$	$(H_d^0,\, H_d^-)$
Gauge Supermultiplet	Vector A^μ (spin 1)	Spinor λ (spin 1/2)
B, *bino*	B^0	$\tilde{B}^0$
W, *wino*	$\mathrm{W}^\pm$, W^0	$\tilde{W}^\pm$, $\tilde{W}^0$
gluon, *gluino*	g	$\tilde{g}$

Table 2.3: Supermultiplets of the MSSM.

breaking. This leaves five physical scalar Higgs particles in the MSSM: the CP-even h^0 and H^0, the CP-odd A^0, and the charged $H^\pm$.

The resulting particle spectrum of the minimal extension of SUSY sketched above, called Minimal Supersymmetric Standard Model (MSSM), is summarized in Tab. 2.3. Superpartners of SM particles are denoted by a tilde above the letter and are called sfermions (e.g. stau, selectron, etc.) or gauginos (e.g. bino, photino, etc.). The fermionic higgsinos mix with the gauginos after electroweak symmetry breaking to form physical states called neutralinos and charginos depending on their electric charge.

The *superpotential* of the MSSM is given by

$$W_{MSSM} = \bar{U}\boldsymbol{y_u}QH_u - \bar{D}\boldsymbol{y_d}QH_d - \bar{E}\boldsymbol{y_e}LH_d + \mu H_u H_d, \tag{2.15}$$

where the $\boldsymbol{y}$ are 3×3 matrices containing Yukawa couplings of scalars to fermions, and μ is the Higgs mass parameter [12]. Terms that violate baryon or lepton conservation are in principle possible in SUSY but were omitted in Eq. 2.15. The non-observation of such processes in the SM due to the stability of the proton led to the inception of *R-parity*, a new conserved quantity:

$$R_P = (-1)^{3B+L+2S}, \tag{2.16}$$

where B and L denote the baryon and lepton numbers, respectively, and S denotes the

spin quantum number [12]. The conservation of R-parity[9] means that sparticles will always be produced in pairs[10] and that the lightest sparticle (LSP) is stable.

The superfields have the invaluable trait of giving loop corrections to all processes that cancel exactly with the contributions from their SM counterparts [12]. This results in a stabilization of the Higgs mass at high energies, which is one of the main qualifying arguments for SUSY as a feasible theory. However, it also implies that the masses of superpartners are equal. Since no such additional particles have been detected by experiments [2], SUSY must be a broken symmetry.

With disregard to the origin or mechanism of SUSY breaking, it can be induced by adding mass terms to the superpotential. It is possible to keep the theory renormalizable by not letting the mass parameters exceed a few TeV [11]. This only results in logarithmic divergences (as opposed to the catastrophic quadratic divergences) and is referred to as *soft* SUSY breaking, since the theory remains stable at high energies [12]. Having soft SUSY breaking also serves as the main motivation to search for sparticles at the TeV scale. In this regime, the LSP will often have masses of below a few hundred GeV, making it an excellent candidate for cold dark matter. Furthermore, if SUSY is broken at the TeV scale, the running gauge couplings can unify with reasonable accuracy at the GUT scale ($\sim 10^{16}$ GeV). Clearly, SUSY is worth examining experimentally as it is capable of at least partly solving many of the SM's deficiencies.

However, with the addition of soft breaking terms, the MSSM contains 105 new parameters, including many CP-violating phases and sfermion mixing angles [11]. This is not a very predictive framework unless the number of parameters is reduced drastically. Constraints on CP-violation and generation-mixing (such as flavor-changing neutral currents and lepton flavor conservation) from experiments make it necessary to set to zero most of these parameters. Another reduction of parameters is achieved when requiring all scalar mass terms to have a common value m_0 at the GUT scale. Similarly, all gaugino mass terms get the value $m_{1/2}$. The couplings A_0 of the Higgs bosons to the sfermions are universal. The sign of the Higgs mass parameter $sign(\mu)$ and the ratio of the Higgs vacuum expectation values $\frac{v_1}{v_2} = \tan\beta$ complete the five parameters describing what is arguably the most popular SUSY breaking model, called *minimal supergravity* (mSUGRA). In this

[9] All SM particles have $R_P = 1$ and all sparticles have $R_P = -1$.

[10] This is assuming that the initial state contains only SM particles, which is of course the case at all colliders.

model, SUSY breaking is caused by an unspecified *hidden sector* of particles which interacts gravitationally with the known particles[11] (the *visible sector*) [11]. Many different models of SUSY breaking have been devised and studied. One of these, named *gauge-mediated supersymmetry breaking* (GMSB), is introduced in the next section.

In order to complete the phenomenological picture of SUSY, another supermultiplet is obtained when promoting SUSY from a global to a local symmetry: the gravity supermultiplet [11]. It contains the graviton and its superpartner, the gravitino (spin 3/2), which is massless unless SUSY is spontaneously broken. In analogy to electroweak symmetry breaking, the gravitino acquires mass in a super-Higgs mechanism [12]. The gravitino only interacts gravitationally which gives rise to interesting signatures in experimental searches if it is the lightest supersymmetric particle.

2.5 Quasi-stable Stau in GMSB

In contrast to mSUGRA (see Sec. 2.4), another way of communicating SUSY breaking from a hidden sector to the visible sector is to have *messenger* fields that underlie the known SM gauge interactions [13]. This *gauge-mediated supersymmetry breaking* (GMSB) approach introduces N_{mess} messenger fields that give mass to sparticles via loop diagrams containing the messengers. Thus, all soft breaking terms arise dynamically [13] and depend on the mass scale of the messenger particles M_{mess}. Additionally, the scale at which SUSY breaking occurs in the visible sector, Λ, is of importance for the determination of the masses of SUSY particles. These two scales are related by

$$\Lambda = F/M_{mess}, \tag{2.17}$$

where $\sqrt{F}$ is the scale of SUSY breaking in the hidden sector which can be as high as the GUT scale, and Λ is always smaller than M_{mess}. All sparticle mass terms obey the relation

$$\tilde{m}_i(M_{mess}) \sim N_{mess}\frac{\alpha_i(M_{mess})}{\pi}\Lambda, \tag{2.18}$$

where the α_i are the usual gauge couplings which are constrained to unify at the GUT scale. See e.g. Refs. [13, 14] for the explicit formulae. For masses of superparticles of the order of 1 TeV, one needs $\Lambda \simeq 100$ TeV. In principle, sparticle masses are proportional to

[11] Much like electroweak symmetry breaking is brought forth by the interaction with a Higgs field.

Λ, meaning that values of Λ lower than about 20 TeV are excluded via lower bounds on new particle masses.

The most outstanding feature of GMSB with respect to other SUSY breaking models is that flavor-changing neutral currents are suppressed naturally, since the soft breaking terms are brought about by the SM gauge interactions which disallow these interactions by construction. Thus, most of the new parameters of the MSSM (see Sec. 2.4) do not come into play in GMSB. The Higgs sector is still described by $\tan\beta$ and $sign(\mu)$, completing the parameters of GMSB:

$$N_{mess},\ \Lambda,\ M_{mess},\ \tan\beta,\ sign(\mu). \tag{2.19}$$

In GMSB, the gravitino is the LSP for any relevant value of F, and its mass is given by

$$m_{\tilde{G}} = \frac{F}{k\sqrt{3}M_{Pl}} = \frac{1}{k}\left(\frac{\sqrt{F}}{100\ \text{TeV}}\right)^2 \text{eV}, \tag{2.20}$$

where M_{Pl} is the Planck mass and k is a dimensionless parameter that is smaller than one [13]. Assuming R-parity conservation, all supersymmetric decays end with the stable gravitino. Since it only interacts gravitationally, the decay of the next-to-lightest SUSY particle (NLSP) into the gravitino may be strongly suppressed. Thus, the phenomenology of GMSB models at colliders like the LHC depends very much on the NLSP and its coupling to the gravitino.

For most of the GMSB parameter space, either the lightest neutralino $\tilde{\chi}_1^0$ or the stau ($\tilde{\tau}$) is the NLSP [13]. This is shown in Fig. 2.8, in the N_{mess}-M_{mess}-plane. The region of transition between the two NLSPs also varies with $\tan\beta$, as indicated by the three solid lines corresponding to different values of $\tan\beta$. Furthermore, the messenger index N_{mess} is restricted to values of 5 or lower[12] if $M_{mess} \simeq 100$ TeV.

If $N_{mess} = 1$, the $\tilde{\chi}_1^0$ is the NLSP except for high values of $\tan\beta$. At increasing values of N_{mess}, the stau is the NLSP beginning at low values of M_{mess} (e.g. $N_{mess} = 1.7$ and $M_{mess} = 100$ TeV), but as the number of messengers increases M_{mess} has to be increased as well to maintain this scenario. At low values of $\tan\beta$, small mass splittings lead to near-degeneracy between the three charged slepton masses. Such a slepton co-NLSP scenario significantly complicates signals at collider experiments. Finally, the stau and neutralino can be co-NLSPs, as shown in Fig. 2.9, where the relevant values of Λ and $\tan\beta$, at which each NLSP scenario is realized, are shown. The colored boxes refer to fixed values of N_{mess}.

[12]Note that N_{mess} is an effective index and is not restricted to integer values.

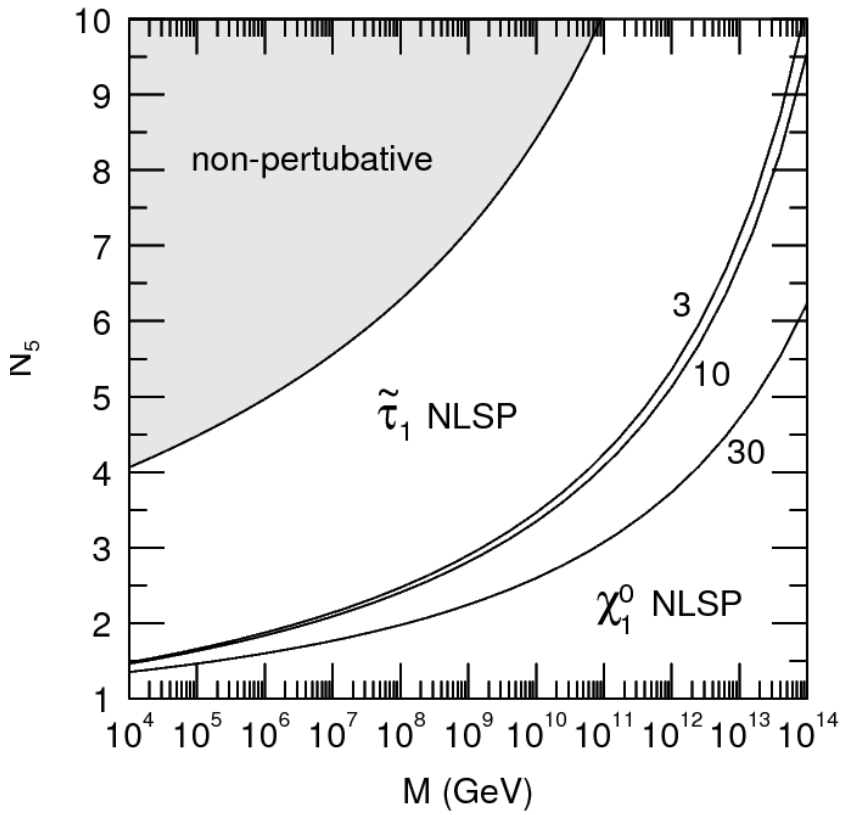

Figure 2.8: Next-to-lightest SUSY particle in GMSB as a function of $N_5 = N_{mess}$ and $M = M_{mess}$. The transition between the scenarios also depends on $\tan\beta$, as shown by the three solid lines corresponding to $\tan\beta = 3$, 10, 30. From [15].

Since we are interested in a heavy stable charged particle, a scenario with the stau as NLSP will be considered. The SPS 7 line [16] is one such GMSB scenario proposed for examination at colliders. In this work, the $\tan\beta$ parameter has been altered with respect to the SPS 7 line, such that the following parameters define one investigated model:

$$N_{mess} = 3, \quad \Lambda = 40 \text{ TeV}, \quad M_{mess} = 80 \text{ TeV}, \quad \tan\beta = 10, \quad \mu > 0, \tag{2.21}$$

where the ratio M_{mess}/Λ is fixed at 2 and Λ can be varied to change sparticle masses and decay ratios. The full mass spectrum of this GMSB model is given in Tab. 2.4. Note that in the third generation of squarks and sleptons, the left and right sfermion states mix to form physical states denoted 1 and 2. The stau NLSP is the $\tilde{\tau}_1$, but the subscript is omitted in the following.

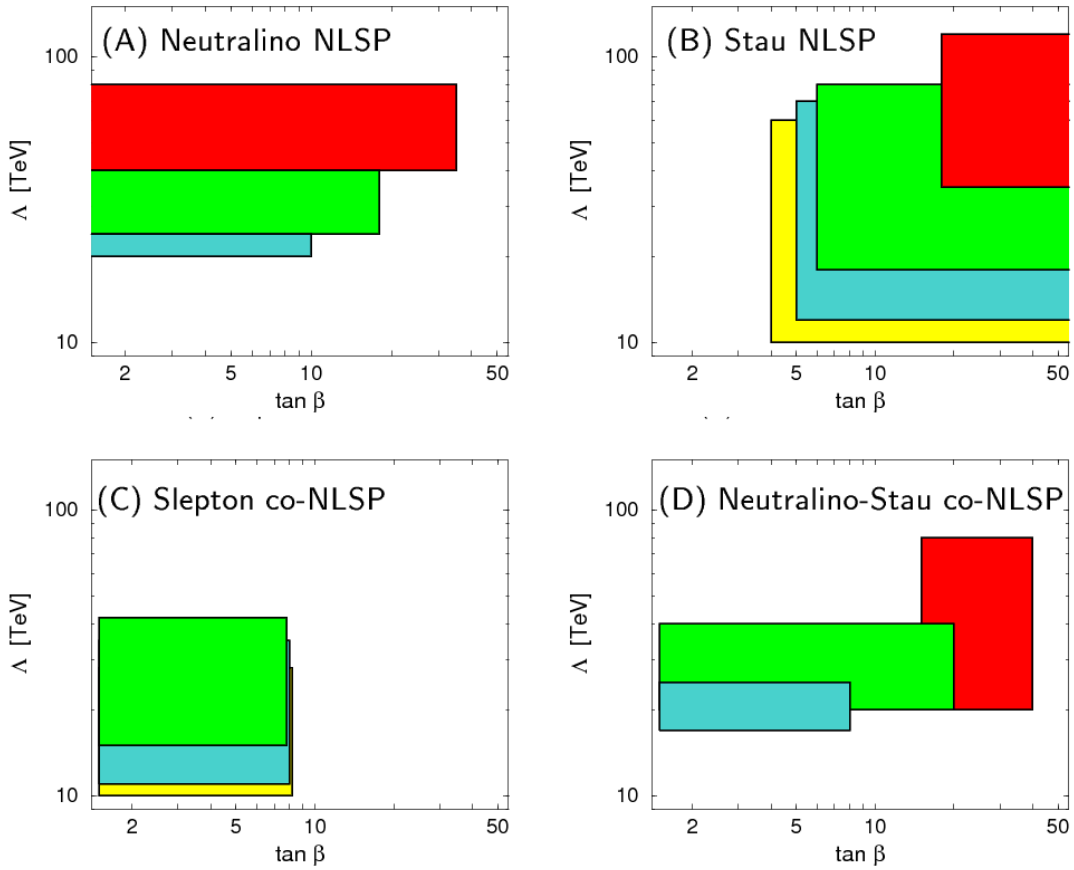

Figure 2.9: Next-to-lightest SUSY particles in GMSB: four possible scenarios and their ranges in the Λ-tan β plane are shown. Colored boxes correspond to fixed values of N_{mess}: red: $N_{mess} = 1$; green: $N_{mess} = 2$; blue: $N_{mess} = 3$; yellow: $N_{mess} = 4$. Scenarios A and D are not allowed for $N_{mess} = 4$, scenario C is not realized for $N_{mess} = 1$. From [15].

The decay width of the stau into its SM partner and the gravitino is given by

$$\Gamma(\tilde{\tau} \to \tau \tilde{G}) = \frac{k^2 m_{\tilde{\tau}}^5}{16\pi F^2} = 2k^2 \left(\frac{m_{\tilde{\tau}}}{100\ \text{GeV}}\right)^5 \left(\frac{100\ \text{TeV}}{\sqrt{F}}\right)^4 10^{-3}\ \text{eV}, \tag{2.22}$$

which accounts for basically 100 % of all stau decays [13]. This translates into a decay length of

$$L = \left[\left(\frac{100\ \text{GeV}}{m_{\tilde{\tau}}}\right)^5 \left(\frac{\sqrt{F/k}}{100\ \text{TeV}}\right)^4 \sqrt{\frac{E^2}{m_{\tilde{\tau}}^2} - 1}\right] 10^{-2}\ \text{cm} \tag{2.23}$$

for a stau with the energy E. The parameter k, which governs the mass of the gravitino and therefore the lifetime of the stau, as shown in Eq. 2.23, is chosen such that a long-lived

Sparticle	Mass [GeV]	Sparticle	Mass [GeV]
Sleptons		Higgs	
$\tilde{\tau}_1$	126	h^0	112
$\tilde{\tau}_2$	268	H^0	398
$\tilde{e}_R$, $\tilde{\mu}_R$	129	A^0	395
$\tilde{e}_L$, $\tilde{\mu}_L$	267	$H^\pm$	406
$\tilde{\nu}_{\tau,L}$, $\tilde{\nu}_{e,L}$, $\tilde{\nu}_{\mu,L}$	251	Gauginos	
Squarks		$\tilde{g}$	952
$\tilde{t}_1$	811	$\tilde{\chi}_1^0$	159
$\tilde{t}_2$	898	$\tilde{\chi}_2^0$	269
$\tilde{b}_1$	868	$\tilde{\chi}_3^0$	314
$\tilde{b}_2$	877	$\tilde{\chi}_4^0$	384
$\tilde{u}_R$, $\tilde{c}_R$	874	$\tilde{\chi}_1^\pm$	268
$\tilde{u}_L$, $\tilde{c}_L$	904	$\tilde{\chi}_2^\pm$	382
$\tilde{d}_R$, $\tilde{s}_R$	873	Gravitino	
$\tilde{d}_L$, $\tilde{s}_L$	908	$\tilde{G}$	$7.7 \cdot 10^{-6}$

Table 2.4: Masses of physical SUSY particles of the GMSB point with $N_{mess} = 3$, $\Lambda = 40$ TeV, $M_{mess} = 80$ TeV, $\tan\beta = 10$, $\mu > 0$.

stau emerges from the model:

$$k = 10^{-4}. \tag{2.24}$$

This leads to a gravitino mass of a few keV, which is near the maximum allowed for the gravitino to be a dark matter candidate in agreement with cosmological bounds [13].

2.6 Heavy Stable Charged Particles

In the context of collider physics, the term *heavy stable charged particles* (HSCPs) refers to massive particles with minimal mean decay lengths of a few centimeters, such that they can be detected by HEP experiments. This can be achieved by measuring their interaction with matter or, in the case of decay length below a few meters, identifying secondary vertices displaced from the central interaction region. Besides being long-lived, the main identifying characteristic of an HSCP is its mass, M_{HSCP}. If it is greater than the lower

momentum reconstruction threshold p_{min} of a tracking detector, a significant amount of HSCPs with momenta $p_{min} < p_{HSCP} < M_{HSCP}$ could be detected. It follows from the relativistic relation between momentum and mass[13],

$$p = \beta\,\gamma\,M, \tag{2.25}$$

that if $p_{HSCP} \lesssim M_{HSCP}$, then $\beta\gamma \lesssim 1$. Therefore, as implied by the Bethe-Bloch formula [2] for the energy loss of a free particle in a medium, these particles will have a higher mean energy loss (dE/dx) than those with $1 \lesssim \beta\gamma \lesssim 1000$. To exemplify the Bethe-Bloch formula, the stopping-power of copper to muons is shown in Fig. 2.10. At values of $0.1 < \beta\gamma < 1.0$, the energy loss decreases quadratically as $\beta\gamma$ increases, $dE/dx \sim (\beta\gamma)^{-2}$. Thus, with Eq. 2.25, the energy loss of a particle is related to its mass and momentum as follows:

$$dE/dx = K\frac{M^2}{p^2} + C, \tag{2.26}$$

where K and C are constants that are specific to the crossed material and have to be determined experimentally[14]. Such a direct handle on the mass of a new particle is a rarity, since most searches for SUSY have to rely on kinematic measurements for the determination of mass spectra.

For stable SM particles with momenta above a few GeV, the measured energy loss will usually be that of a mimimally ionizing particle (MIP), since these particles' masses are below a few GeV. Only at very low momenta can these particles produce high energy losses. This can be exploited to calibrate the energy loss measurement if the detector allows for efficient measurements of tracks at such low momenta. In CMS, the energy loss of particles is measured with the silicon strip tracker as outlined in Section 4.2.1. For most HEP experiments, low-momentum protons and kaons are suitable for the calibration of Eq. 2.26.

In the effort to extend the Standard Model to address its shortcomings, many theories have been devised that predict HSCPs with masses of hundreds of GeV and above [18]. If copious amounts of HSCPs with $p_{HSCP} \lesssim M_{HSCP}$ were produced, these "true" HSCPs

[13]Relativistic notation: $\beta = \frac{v}{c}$, $\gamma = (1-\beta^2)^{-1/2}$, where c is the speed of light in a vacuum which is set equal 1 throughout this work.

[14]For the CMS tracker's silicon strip modules, it has been shown [17] that Eq. 2.26 is accurate to about one percent for particles traversing the tracker at speeds $0.4 < \beta < 0.9$.

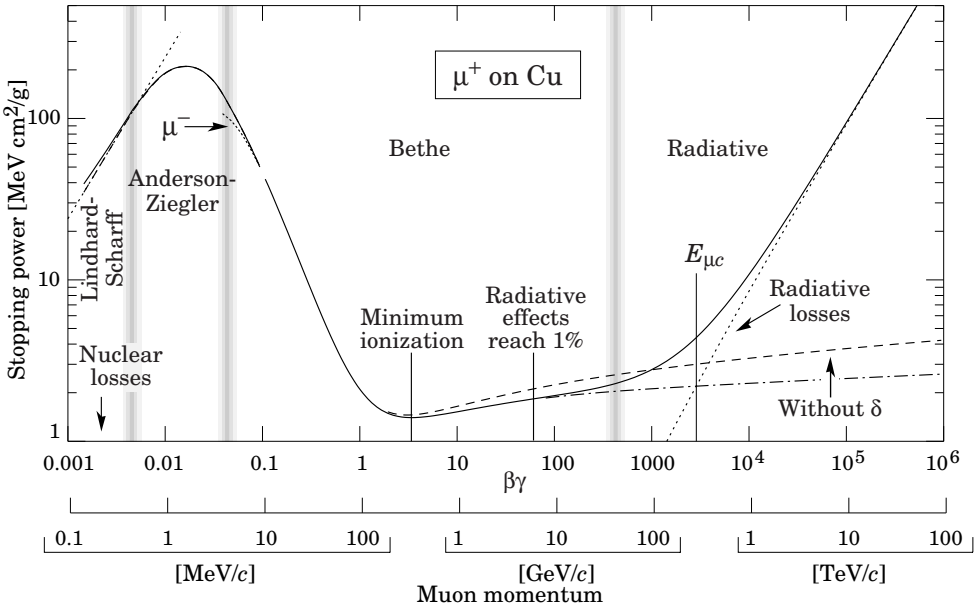

Figure 2.10: Muon stopping-power ($-dE/dx$) of copper as a function of $\beta\gamma = pM/c$ and momentum. Taken from [2].

would have an unmistakable signature of high momentum and high energy loss without sizeable SM backgrounds. Furthermore, HSCPs do not cause significant electromagnetic or hadronic showers due to their high masses, making them detectable with muon detectors as well. One possible HSCP, namely a quasi-stable scalar tau lepton arising in *gauge-mediated supersymmetry breaking*, outlined in the previous section, is studied in this thesis. Experiments at the LEP collider have excluded such particles with masses below 97.5 GeV [19].

Chapter 3

The CMS Experiment at the LHC

3.1 The Large Hadron Collider

The Large Hadron Collider (LHC) [20] is a circular particle collider operated by the European Organization for Nuclear Research (CERN) in Geneva, Switzerland. It is designed for proton-proton and lead-ion collisions at unprecedented energies and luminosities. LHC design parameters for proton-collisions are a center-of-mass energy $E_{cms} = 14$ TeV at $\mathcal{L} = 10^{34}\,\mathrm{cm}^{-2}\mathrm{s}^{-1}$. For two identical beams of n_b bunches with n_p protons per bunch, that have a revolution frequency f, and cross section A transverse to the beam-line, the instantaneous luminosity is given by $\mathcal{L} = f\frac{n_b n_p^2}{A}$.

Four major experiments, conceived to measure the wealth of particles coming from the collisions, are situated along the LHC ring. Two of these experiments, ATLAS and CMS, are multi-purpose detectors designed to measure all Standard Model processes as well as new, hypothetical particles of various kinds. The other two experiments serve more specific causes: The ALICE collaboration is focused on lead-ion collisions, especially the possible measurement of quark-gluon-plasma. Finally, LHCb is specialized on measuring various aspects of the b-quark, e.g. CP-violation. Additionally, several smaller experiments are situated within the experimental halls of the large detectors. An overview of the LHC, its pre-accelerators, and the experiments is shown in Fig. 3.1.

The LHC commenced operations in November 2009 with proton collisions at 900 GeV center-of-mass energy. A short run at 2.36 TeV was performed before shutting down the machine at the end of that year. On March 30th, 2010, proton bunches collided at 7 TeV center-of-mass energy for the first time. Whereas this beam energy was maintained

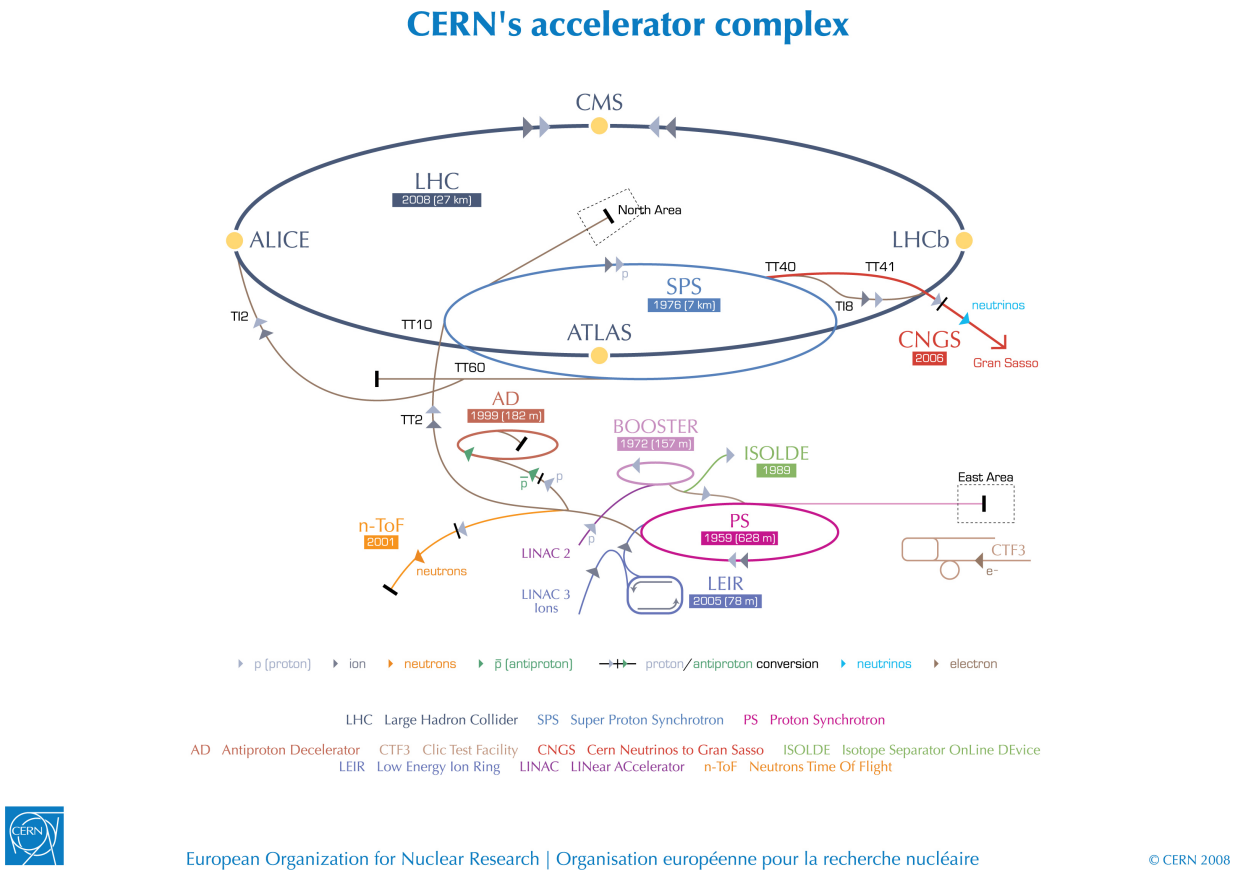

Figure 3.1: Schematic overview of the LHC and its pre-accelerators.

throughout the end of proton running in 2010[1], the instantaneous luminosity was increased gradually. Figure 3.2 shows the integrated luminosity recorded by CMS in the 7 TeV run in 2010 and the maximum instantaneous luminosity per day. In total, CMS accumulated 43.17 pb^{-1} of data and the maximum measured luminosity was $2.05 \times 10^{32}\,\text{cm}^{-2}\text{s}^{-1}$.

3.2 The Compact Muon Solenoid Experiment

The Compact Muon Solenoid (CMS) experiment [21, 22] at the LHC is designed to measure elementary particle interactions produced in collisions of protons or heavy ions. It is a cylindric high-energy physics detector with several layers of subdetectors and a solenoid magnet to divert charged particles. Surrounding the beam pipe is a silicon pixel detector followed by a large silicon strip detector. These two detectors comprise the CMS tracker

[1]This excludes operation with lead ions, which was carried out in November and December 2010.

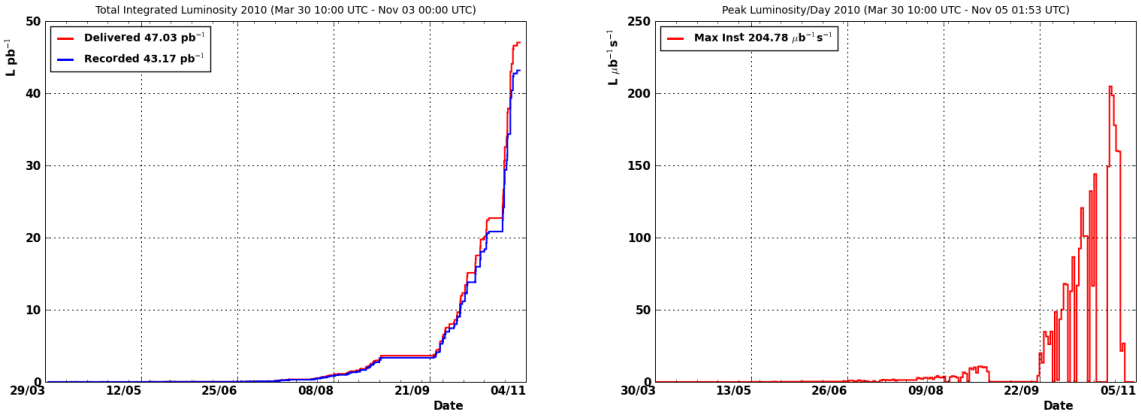

Figure 3.2: Day-by-day luminosity in 2010: delivered by LHC and recorded by CMS (left) and maximum instantaneous luminosity in CMS (right).

which is the largest of its kind. Particle tracks and vertices are reconstructed in its fiducial volume. Surrounding the tracker are the electromagnetic and hadronic calorimeters which measure showers of the corresponding particles. The large solenoid magnet provides a uniform field of 3.8 Tesla parallel to the beam-line to the aforementioned detectors, which are situated inside the coil. Outside the coil, the return field of the magnet permeates the iron yoke and muon chambers which are installed in alternating layers, completing the detector.

These substructures add up to a length of 21.6 m, a diamater of 14.6 m, and a weight of 12500 tons. A schematic picture of the detector is shown in Fig. 3.3.

CMS uses a right-handed coordinate system where the x-axis points toward the center of the LHC ring, the y-axis points toward the sky, and the z-axis points in the direction of the anti-clockwise beam. The polar angle Θ is defined in relative to the z-axis, whereas the azimuthal angle ϕ is measured from the x-axis in the x-y-plane.

3.2.1 Silicon Tracker

The identification of charged particles and reconstruction of vertices requires detectors very close to the interaction region which have high spatial granularity and fast read-out. Furthermore, the high particle flux close to the beam-pipe requires the active material to be quite resistant to radiation-damage accumulated during the long-term LHC operation. To facilitate these needs, CMS utilizes semi-conducting silicon as sensor material for the

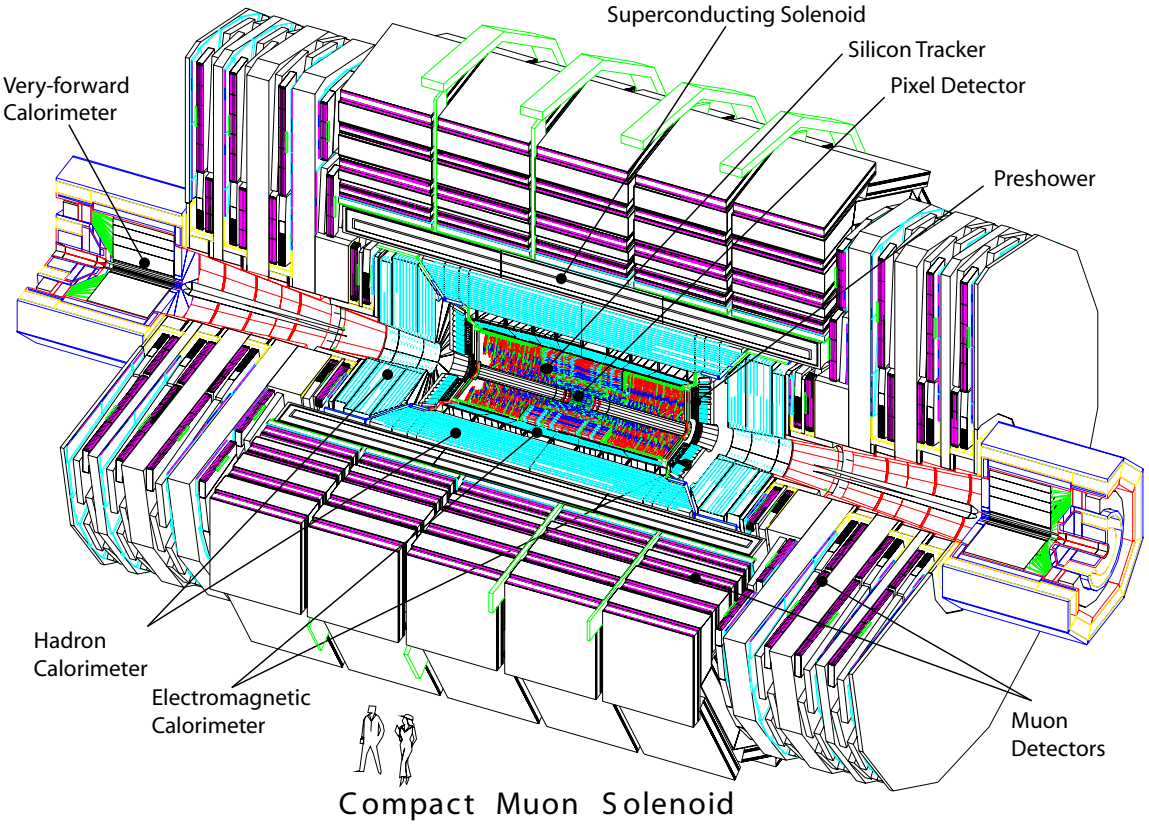

Figure 3.3: Schematic view of the CMS detector. [21]

tracker. At design luminosity and beam energy, about 1000 particle tracks will cross the detectors every 25 ns, necessitating a silicon pixel sensor design at low radii from the interaction point (IP) in order to keep the occupancy at or below one percent. This is necessary to enable pattern recognition and impact parameter resolution. Outside of about 20 cm from the beam pipe, silicon strip sensors suffice to maintain high position resolution while keeping the number of read-out channels at a manageable level.

The tracker covers a volume that is 5.8 m long with a radius of 1.2 m, covering a range of $|\eta| < 2.5$ in pseudorapidity[2]. The amount of material crossed by particles traversing the detector, measured in electromagnetic radiation lengths, X_0, depends on the polar angle[3]. It is minimal at $|\eta| = 0$ (0.4 X_0), maximal in the barrel-endcap transition region around

[2]The pseudorapidity η is a parametrization of the polar angle Θ: $\eta = -\ln(\tan\frac{\Theta}{2})$.

[3]One radiation length X_0 is the distance in a material after which a relativistic electron loses all but 1/e of its energy through bremsstrahlung [2].

$|\eta| \sim 1.4$ (1.8 X_0), and falls off to about 1 X_0 at $|\eta| = 2.5$.

The expected performance of the tracker in measuring the momentum of muons is shown below in Fig. 3.9. In general, tracks with transverse momenta of 100 GeV are reconstructed with a precision of $1-2$ %. At $p_T \simeq 20$ GeV, the resolution of the transverse impact parameter is about 20 μm which goes down to about 10 μm at high momenta (above 100 GeV).

Pixel Detector

The pixel detector consists of three layers of silicon pixel modules in the barrel, located at radii of 4.4, 7.3, and 11.2 cm, respectively, and two endcap disks on either side of the barrel at $z = \pm 34.5$ cm and $z = \pm 46.5$ cm. This layout contains 1440 modules with a total of 66 million pixels which have a size of 100×150 μm^2. An analogue read-out scheme with zero-suppression is used for the sensors, enabling the identification of large clusters from overlapping tracks. The sensors measure both the $r - \phi$ and z-coordinates of hits with a positional resolution of 9-20 μm. This resolution is achieved because of charge-sharing between pixels which, in the barrel, is invoked by the magnetic field and the resulting Lorentz-drift. In the forward sensors, this effect is invoked geometrically by tilting the modules about 20 ° with respect to the transverse plane.

The pixel barrel is subject to the highest particle fluences, and the innermost layer is expected to be functional for about two years at LHC design luminosity, whereas after about three years, the whole pixel detector will have to be replaced. Pixel upgrade research is fully underway in order to complete a replacement in time.

Strip Detector

The Silicon Strip Tracker (SST) consists of 15148 silicon strip modules arranged in four subdetector types. The Tracker Inner Barrel (TIB) has four cylindric layers of modules while the Inner Disks (TIDs), located at both ends of the TIB, have three disks with three rings of modules each. Both TIB and TID extend from 20 cm to 55 cm in radial direction. They are enclosed by the Outer Barrel (TOB), which is comprised of six layers, and two endcaps (TECs) with nine disks each. The outermost layer of the TOB is situated 116 cm from the beam-line whereas the outermost disks of the TECs are located at $z = \pm 282$ cm from the IP. The TEC disks have differing numbers of rings, as shown in Figure 3.4.

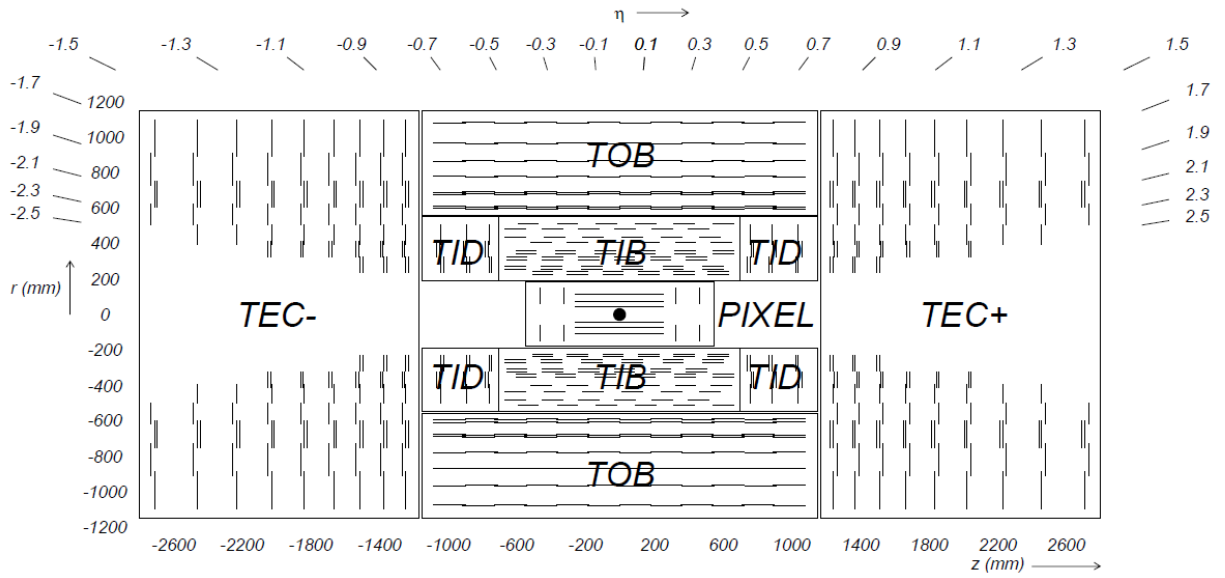

Figure 3.4: Schematic view of the silicon tracker in the r-z-plane. [21, 22] Each line represents a silicon module. Double lines represent double-sided strip modules.

The sensors of the SST use single-sided p-on-n type silicon micro-strip technology. Six-inch wafers of different thicknesses were chosen for the sensors. In TIB, TID, and the four innermost rings of the TECs, 320 μm thick wafers are used, while in TOB and rings five to seven of TEC the thickness is 500 μm. The latter modules have two sensors wire-bonded together, effectively forming strips that are twice as long and thus have more noise[4]. Increasing the wafer thickness leads to an increase in signal and was chosen to keep the signal-to-noise ratio above ten for all sensors. Strip pitches range from 80 μm in the two innermost layers of the TIB up to 183 μm in the TOB, which translates to single-point resolutions in $r - \phi$ of 23 and 53 μm, respectively. In the TID and TEC, wedge-shaped sensors are used, leading to non-constant strip pitches ranging from 100 to 184 μm.

On the backside of the sensors, an n^+ implantation covered by aluminium is connected to a positive voltage of up to 500 V, whereas the strips on the front are p^+ implantations on the n type bulk. Each implanted strip is in turn covered by an aluminum strip which is wire-bonded to a read-out chip on one side of the module. Strip lengths on a single sensor are typically 10 or 12 cm. The modules have either 512 or 768 strips which amounts to a total of 9.3 million strips covering about 198 m^2.

[4]The occupancy in the outer parts of the tracker is low enough to allow for larger modules.

In order to obtain two-dimensional hit information, two modules are mounted back-to-back (so-called *double-sided* modules) with a stereo angle of 100 mrad in the first two layers and rings of TIB, TOB, and TID, as well as rings 1, 2, and 5 in the TECs. This makes a measurement in the second coordinate (z in the barrel, r in the endcaps) of the sensor plane possible, albeit at one-tenth in resolution.

The read-out of the modules begins with four or six *Analogue Pipeline Voltage* (APV) chips (depending on the number of strips) which connect to 128 strips each. Two different read-out modes are provided by the APV. In *peak* mode, the signal, which takes 50 ns to build, is sampled at its maximum. In *deconvolution* mode, the signal is sampled at three positions of which a weighted mean is computed, reducing the rise time to 25 ns. The latter mode is used in collision data taking in order to assign measurements to the correct LHC bunch crossing. The signal of an APV is sampled at the LHC frequency of 40 MHz by a pipeline with 192 elements, giving a maximum buffer time of 4.8 μs. In order to transmit the signal to the processor farm, it is converted into an optical signal by an *Analogue-Opto-Hybrid* (AOH). The gain of the AOHs differs and has to be determined in-situ with collision tracks. At the end of the optical link, a *Front End Driver* (FED) unit receives the signal of 96 fibres, each carrying the signal of two APVs (corresponding to 256 silicon channels). The signals are digitzed by a 10-bit *Analogue-to-Digital Converter* (ADC). Finally, the signal is corrected by pedestal subtraction[5], common mode correction[6], and zero suppression[7] before being transferred to data acquisition at 8-bit resolution. This equates to a maximum signal height of 256 ADC counts per hit. Since the original signal has 10-bit resolution (1024 ADC counts), the 256th count is filled with clusters that were saturated in the original signal (having had more than 1023 ADC counts), whereas the 255th count is used for clusters with 255 to 1023 counts.

[5]The pedestal is the average noise of each strip which is determined by operating the tracker in non-collision mode.

[6]The common mode of an APV is the remaining average signal across all strips after pedestal subtraction which is determined event-by-event.

[7]A strip is only read out if its signal is five times larger than its average noise or if it is part of a group of neighboring strips that each have a signal of at least twice their respective average noise.

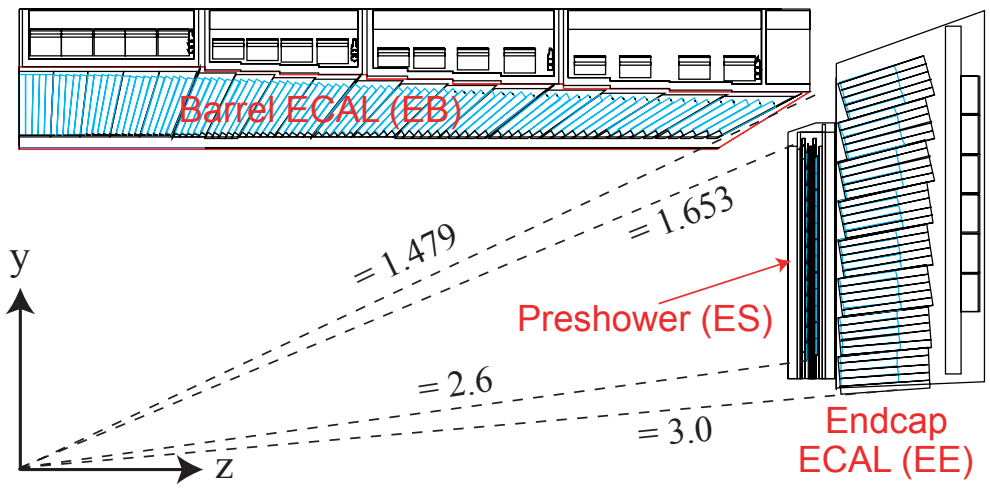

Figure 3.5: Schematic view of one-quarter of the electromagnetic calorimeter in the y-z-plane. [22]

3.2.2 Electromagnetic Calorimeter

The electromagnetic calorimeter (ECAL) is divided into a barrel part and two endcaps. Lead tungstate ($PbWO_4$) crystals with a density of 8.28 g/cm^3 and radiation length of 0.89 cm are used as active scintillators. Additionally, preshower detectors are installed in front of the endcaps in order to improve the detection of neutral pions and the identification of electrons against minimum-ionizing particles in the forward region. The design of the ECAL was heavily influenced by the ability to reconstruct a Higgs boson decaying into two photons.

The ECAL barrel section (EB), surrounding the silicon tracker, has an inner radius of 129 cm and covers a pseudorapidity range of $|\eta| < 1.479$. Its 61200 crystals have a front-face area of 22×22 mm^2, back-face area of 26×26 mm^2, and a length of 230 mm, corresponding to 25.8 radiation lengths. This setup results in a high granularity of 360 crystals in ϕ and 170 crystals in η. For the readout of the scintillation light, two avalanche photodiodes are glued to the back-face of each crystal.

The endcaps (EE), starting 315.4 cm from the nominal IP, contain 7324 crystals each, covering a range of $1.479 < |\eta| < 3.0$. The crystals in the endcaps have front-face areas of 28.6×28.6 mm^2, back-face areas of 30×30 mm^2, and are 220 mm long (24.7 X_0). One vacuum phototriode, designed to operate in high magnetic fields, is attached to the back-face of each endcap crystal.

The preshower detectors (ES) consist of lead radiators and 4288 silicon strip sensors

arranged in two layers, with a coverage of $1.653 < |\eta| < 2.6$ in pseudorapidity. The total thickness of each ES is 20 cm which is equivalent to 3 X_0, causing about 95 % of incident photons to start showering before reaching the second layer of silicon sensors.

Figure 3.5 displays the layout of the ECAL. Its overall energy resolution is parametrized as follows:

$$\left(\frac{\sigma}{E}\right)^2 = \left(\frac{S}{\sqrt{E}}\right)^2 + \left(\frac{N}{E}\right)^2 + C^2, \tag{3.1}$$

where the energy E is given in GeV. The stochastic term, S, is composed of fluctuations in the lateral shower size, a photostatistics contribution of 2.1 %, and energy measurement fluctuations in the preshower (where applicable). Noise contributions from electronics, digitization, and pileup are summed up in N. The constant term, C, includes intercalibration errors, leakage of energy from the rear of the calorimeter, and non-uniformities in longitudinal light collection. At energies above about 500 GeV, shower leakage into the HCAL becomes significant, therefore Eq. 3.1 loses validity at these high energies.

In test-beam measurements carried out in 2004 at CERN, electrons with energies of 20 to 250 GeV were used to calculate the energy resolution. Typical values obtained were: $S = 2.8\%$, $N = 12\%$, $C = 0.3\%$.

In the first few months of data taking in 2010, the fraction of operating channels of the EB and EE was 99.30 % and 98.94 %, respectively [23]. Additionally, 0.3 % of crystals in EB and 0.7 % in EE were deemed problematic and disregarded in the offline reconstruction of the data. For the ES, 99.79 % of silicon strips were functional.

3.2.3 Hadronic Calorimeter

The hadronic calorimeter (HCAL), besides detecting hadronic particles, was constructed for the important purpose of providing good hermeticity for the measurement of missing transverse energy. The barrel (HB) and endcap (HE) sections sit behind the ECAL inside the solenoid magnet. The hadron outer calorimeter (HO) is situated in the barrel outside the coil, whereas the hadron forward (HF) calorimeters lie close to the beam-pipe, albeit far from the IP, in order to provide coverage at high pseudorapidities.

The HCAL (not including the HF) is a sandwich sampling calorimeter using brass as absorber material ($\rho = 8.53$ g/cm^3) and plastic scintillators. These materials were chosen with the aim of maximizing the absorber material inside the solenoid while keeping the active material at a minimum. The scintillator tiles have a thickness of 3.7 mm and are

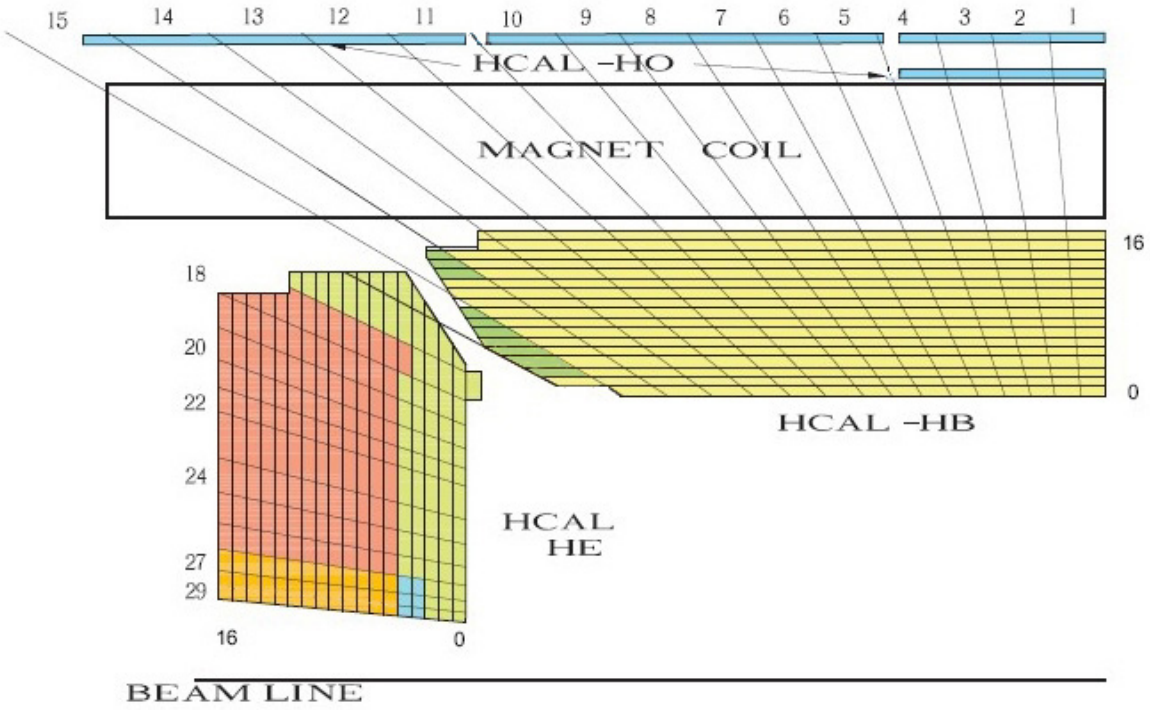

Figure 3.6: Schematic view of one-quarter of the hadronic calorimeter in the y-z-plane. The numbers denote tower and layer indices. [21]

read out with wavelength-shifting fibres connected to hybrid photodiodes (HPDs).

In the barrel, the front and rear scintillator layers have a thickness of 9 mm, inside of which lie steel plates installed for mechanical stability. This frame contains 32 calorimeter towers in pseudorapidity and 72 towers in azimuthal angle, amounting to 2304 towers covering $-1.4 < \eta < 1.4$. Each tower consists of 14 brass plates with a thickness of about 5 cm and 14 scintillator tiles which are read out longitudinally by one HPD. The material thickness of the HB corresponds to 5.8 hadronic interaction lengths (λ_l)[8]. For particles originating at the nominal IP, the effective thickness increases with the polar angle, e.g. to 10.6 λ_l at $|\eta| = 1.3$. The ECAL barrel adds about 1.1 λ_l to the material budget.

The HCAL endcaps cover $1.3 < |\eta| < 3.0$ and consist of towers with 12 to 17 layers of brass plates (7.9 cm thick) and scintillators, resulting in a total material thickness

[8]One interaction length λ_l is the distance in a material after which the energy of a relativistic charged particle is reduced by a factor of 1/e through nuclear interactions [2].

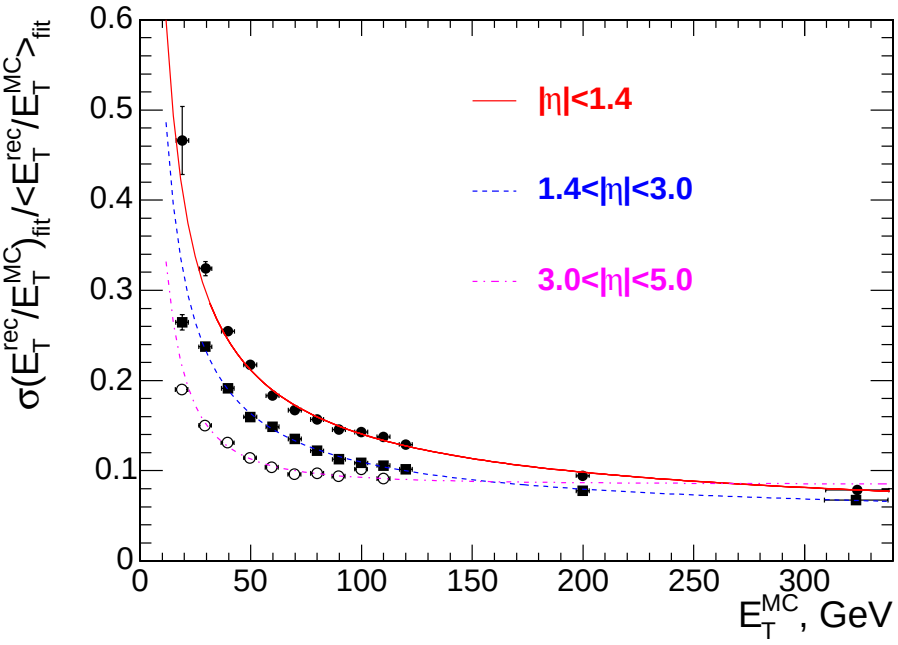

Figure 3.7: Jet transverse energy resolution as a function of transverse energy from simulated dijet events. Jets from three pseudorapidity regions are plotted. [22]

(including the ECAL endcaps) of more than 10 interaction lengths. The granularity of the five innermost ($|\eta| < 1.74$) towers is 5° in ϕ, while the towers with $|\eta| > 1.74$ have 10°-ϕ-segmentation. The schematic arrangement of the HCAL parts is shown in Fig. 3.6.

In the barrel region, the material thickness of the calorimeters does not suffice to contain all high-energy hadron showers. Therefore, additional 10 mm-thick scintillators referred to as Hadron Outer are installed in the pseudorapidity range $|\eta| < 1.3$ outside the solenoid, which acts as an absorber with $1.4/\sin\Theta$ radiation lengths. The HO is segmented into five rings in η, with the central ring having two scintillator layers while all others have one layer. The total depth of the barrel calorimetry is thus increased to a minimum of 11.8 λ_I.

Situated close to the beam-pipe with the front faces at 11.2 m from the IP, the hadron forward calorimeters cover the region $2.85 < |\eta| < 5.19$. The HF is subject to the highest particle fluences of any subdetector in CMS. Therefore, radiation-hard quartz-fibre was chosen as active material and steel as absorber. Each HF contains 432 towers which are connected to photomultipliers for signal read-out. The total absorber length is 165 cm which is equivalent to about 10 λ_I.

The jet energy resolution as a function of the true simulated jet transverse energy for

the barrel, endcap, and forward regions is shown in Figure 3.7. The resolution of missing transverse energy, E_T^{miss}, is given by $\sigma(E_T^{miss}) \approx 1.0\sqrt{\Sigma E_T}$.

3.2.4 Superconducting Magnet

The specifications of the CMS magnet were driven by the goal to efficiently reconstruct muons at very high momenta. A superconducting solenoid maintaining a uniform magnetic field of 3.8 T was chosen for this purpose. At 6.3 m in diameter and 12.5 m in length, the magnet completely surrounds the tracker and barrel calorimeters. The radial thickness of the coil is 31.2 cm, making the magnet a "thin coil" ($\Delta R/R \approx 0.1$), and the operating temperature is 4.6 K. At full current (ca. 19 kA), the solenoid stores about 2.6 kJ of energy, making it the strongest magnet ever used in high energy physics experiments. For the return-flux of the magnetic field, iron plates, collectively called "return-yoke", are installed in four layers in the barrel, and three discs in each endcap, which are sandwiched between the muon chambers. The barrel plates weigh a total of 6000 tonnes while the endcap disks add 4000 tonnes, thus the return yoke makes up about 80 % of the total weight of the CMS detector.

3.2.5 Muon System

The task of reconstructing muons at energies of a few GeV to a few TeV is a central aspect of the CMS detector design. To this end, the muon system utilizes three types of gaseous particle detectors situated outside the solenoid magnet. Figure 3.8 shows the layout of the muon stations.

In the barrel region, drift tube chambers (DTs) are arranged in four layers (so-called stations) which are interspersed with iron return-yoke holding most of the flux of the solenoid magnetic field. Each station has eight chambers to measure the coordinate in the $r-\phi$-plane, and the first three of the four stations have four additional chambers which measure the z-coordinate. The $r-\phi$-measuring chambers are grouped into two sets of four which are staggered by half a cell with respect to their neighbor in order to obtain an optimal angular resolution. In total, 250 DTs cover $|\eta| < 1.2$ in pseudorapidity. The drift distance of ionized particles in the chambers is capped at 21 mm, with an associated drift time of about 380 ns, which is small enough to ensure low occupancy even at design LHC luminosity. Single hits in the DTs can be resolved with an accuracy of about 200 μm,

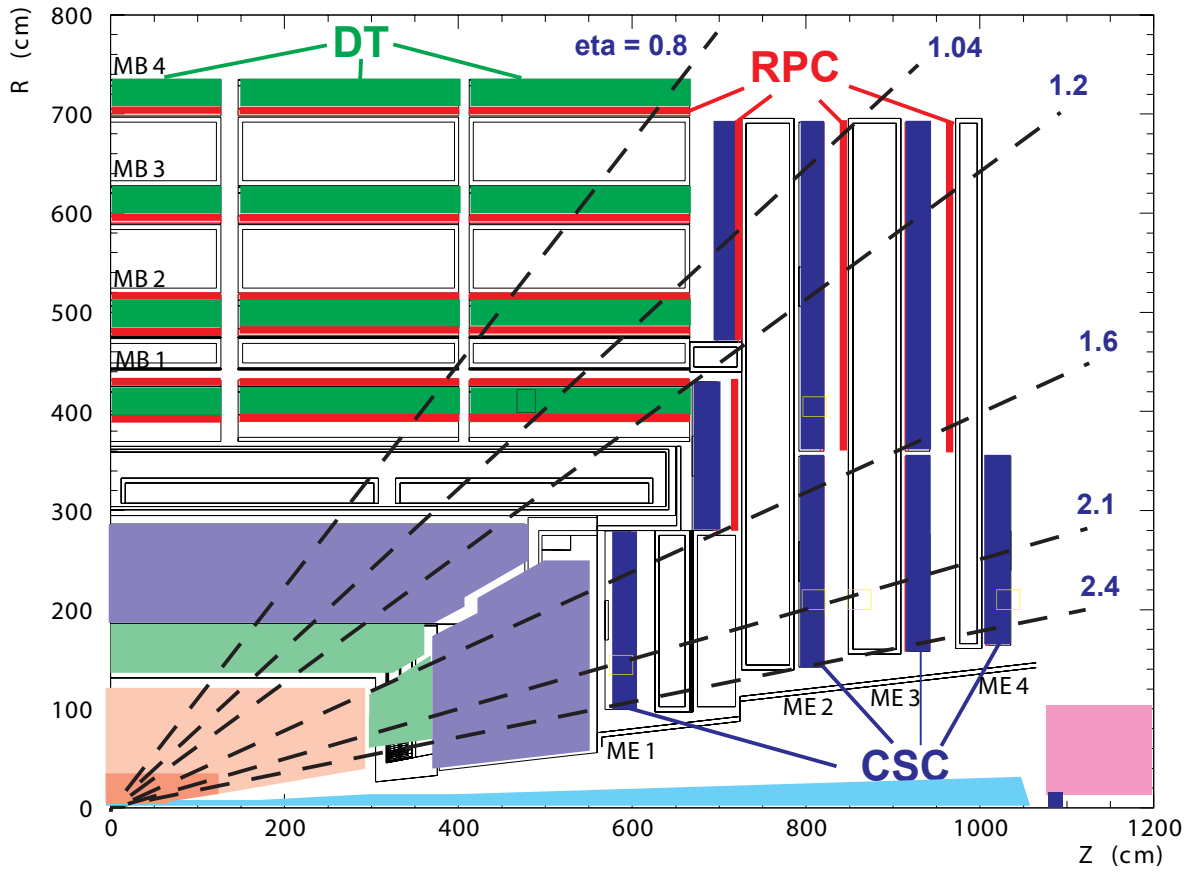

Figure 3.8: Schematic view of the muon system in the r-z-plane. Only the positive-z half is shown. [22]

making a global resolution of 100 μm in the $r-\phi$-plane possible.

The muon system endcaps are equipped with 468 cathode strip chambers (CSCs), which are arranged in four layers between the iron return yoke, providing measurements in the pseudorapidity region $0.9 < |\eta| < 2.4$. Faster response time is provided by the CSCs, which is necessary due to the higher muon rate in the forward region. Each CSC consists of seven layers of cathode strips running radially and six anode wire planes. In total, about 220000 cathode strips and 180000 anode wires are read out. The spatial resolution of a single chamber is about 80 μm in the $r-\phi$-direction.

Resistive plate chambers (RPCs) complement the DTs and CSCs with additional measurements in the region of $|\eta| < 1.6$, with an extension to $|\eta| < 2.1$ planned for later running periods. Additionally, the RPCs provide a faster triggering mechanism for muons than the DTs or CSCs. The RPCs are gaseous parallel plate detectors with two 2 mm

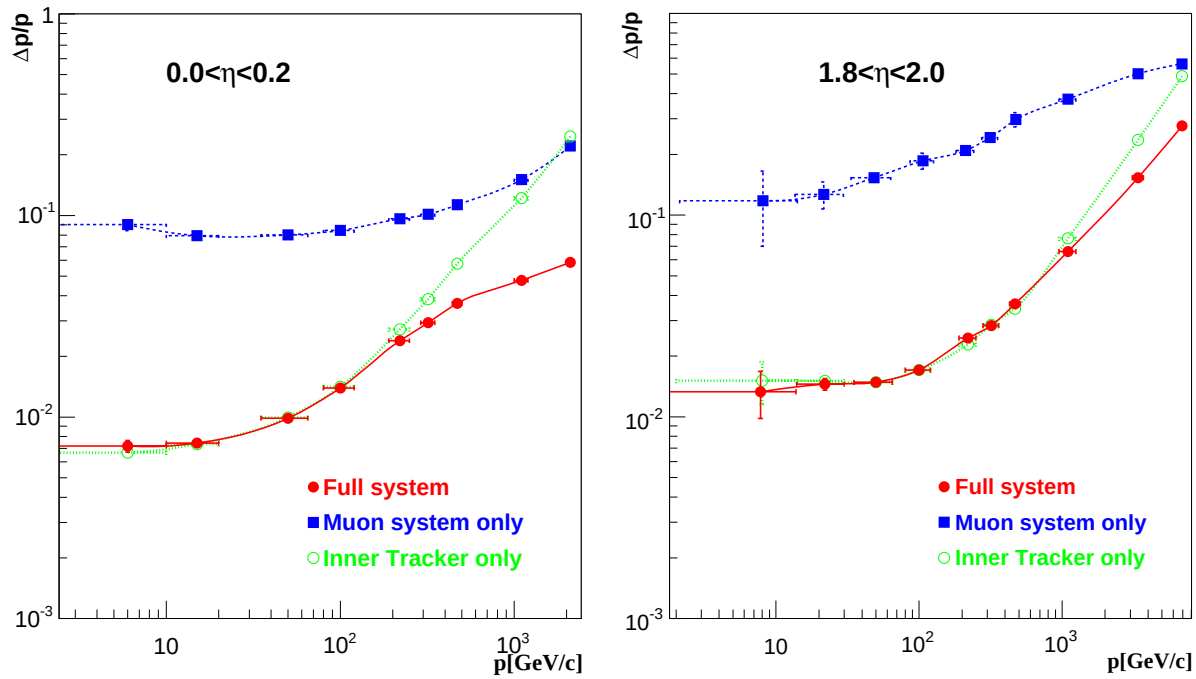

Figure 3.9: Momentum resolution as a function of momentum for muons in a central (left) and a forward (right) region of the CMS detector. Results are shown for tracks from the tracker (green), muon system (blue), and both detectors combined (red). [22]

gaps holding the gas, which measure particle crossing times faster than the nominal LHC bunch spacing of 25 ns. Their positional resolution is coarser than that of the DTs and CSCs. In the barrel, 480 RPCs are installed in six layers, while three layers are present in the endcaps.

The momentum resolution of muons is determined by the measurements of tracks in both the tracker and the muon system, as shown in Figure 3.9. At momenta of up to about 100 GeV, where multiple scattering in the material before the muon system is significant, the tracker resolution is about one order of magnitude better than that of the muon system. At higher momenta, combining tracker and muon tracks into one long "global" track yields the best results, since the long lever arm of the muon system improves the reconstruction as momentum increases and tracks become straighter. The aim of the "global muon" reconstruction in CMS is to obtain a momentum resolution of about 10 % at 1 TeV.

3.2.6 Trigger System

At the design luminosity of LHC of $10^{34}\text{cm}^{-2}\text{s}^{-1}$, the proton bunch-crossing rate will be 40 MHz, and about 20 inelastic collisions will take place at each bunch crossing. The resulting event rate will exceed the possible data processing rate by many orders of magnitude. Therefore, a two-level trigger system is used by CMS to reduce the rate of recorded events to about 200 Hz.

The Level-1 trigger (L1) [24] is a hardware-based system using data from the calorimeters and the muon system. Initially, local triggers are activated if energy thresholds in calorimeter towers are surpassed or simple track patterns arise in the muon chambers. Then, regional triggers combine local information to check whether electron or muon candidates are feasible in limited regions. Finally, the global muon and calorimeter triggers order the output of the regional triggers by quality and pass the information to the global trigger which decides whether an event will be passed to the next trigger stage. The total latency of the L1 trigger is 3.2 μs and the output rate is about 30 kHz.

The second stage of the trigger system is the High Level Trigger (HLT) [25]. It is a software trigger with many algorithms using almost the full event data accumulated in the CMS detector. Whereas the tracker is not part of the L1 trigger, the HLT uses full track information. HLT algorithms evolve as the instantaneous luminosity increases in order to keep the total rate of recorded events stable. There are about one hundred HLT paths which select different combinations of particles at various energy thresholds to suit the wide range of event topologies expected in CMS.

3.2.7 Luminosity Monitoring

Since most CMS physices analyses need to have an absolute normalization, the accurate determination of the integrated luminosity is indispensable. There are multiple techniques to calculate the luminosity online and offline.

In 2010, the hadron horward calorimeter was used for the real-time measurement of the luminosity in CMS [26]. The E_T distribution from four rings (at $3.5 < |\eta| < 4.2$) of the HF is analyzed in two independent ways: the number of empty towers is used to count the mean number of interactions and thus the luminosity; the total E_T deposited in the HF rises linearly with the number of interactions. The high pseudorapidity at which the measurement is made kinematically limits the total E_T to about 200 GeV, thus suppressing

large statistical fluctuations.

Two offline methods are used to check the online estimation of the luminosity. The first requires the coincidence of transverse energy measurements of at least 1 GeV in both HFs, this time using all towers. A timing cut of $|t_{HF}| < 8$ ns reduces non-collision backgrounds. The second method uses tracker information, requiring at least one vertex with two or more tracks at $z < 15$ cm from the nominal interaction point.

The absolute scale of the luminosity measurement is obtained by making Van der Meer scans [27] to extract the size and shape of the proton beams.

During the 7 TeV running period in 2010, the systematic uncertainty on the luminosity measurement was estimated to be 4 % [28]. The largest contribution to this number is the uncertainty on the beam current measurements, which was estimated to be 2.9 %.

Chapter 4

Event Simulation and Reconstruction

Any physics experiment needs to be compared to the known theory, which in this work is the Standard Model of particle physics. To this end, proton-proton collisions and the response of the CMS detector to the ensuing particles are simulated to a high degree of detail, as outlined in this chapter. The subsequent calculation of meaningful observables from detector signals (whether from real data or simulation), referred to as physics object reconstruction, is detailed for the relevant objects used in this study.

4.1 Event & Detector Simulation

Event generation in high-energy physics means the computation of final state particles from two incoming, initial state particles. For the LHC, the initial interaction is the scattering of two or more partons from the incoming protons. The final state particles are then subjected to a detailed simulation of a detector, and the corresponding signals in each subdetector are modelled. After full reconstruction of these simulated signals, the output should equal that of a real collision in the detector, meaning that a set of four-vectors of particles crossing the detector is produced.

By generating many kinds of known (SM) and hypothetical (e.g. Higgs, SUSY) processes, the real data collected by the detector are compared to simulation and interpreted afterwards. Of course, there are limitations as to which processes can be simulated precisely in a perturbative way. Therefore, many processes (e.g. low-energy QCD, fragmentation and hadronization) have to be modelled according to what is observed experimentally.

A myriad of programs exist for the generation of high-energy physics processes. One

of the most heavily used generators in the particle physics community, PYTHIA (version 6.4 [29]), was utilized in the generation of all simulated samples that are necessary for this work. PYTHIA is a leading-order event generator that has several modifications (so-called "tunes") that simulate the underlying event. Two of these, named "D6T" and "Z2" are used in this work. PYTHIA also simulates parton showering, meaning the radiation of gluons and photons from colored and electrically charged objects, as well as the subsequent fragmentation and hadronization of all colored objects in the event.

Another generator used in this study is MadGraph [30], which calculates leading-order processes with the addition of multiple final-state hadronic jets. Up to four jets are added to a leading order process, and the resulting events are weighted according to the number of additional jets. MadGraph does not perform the actual hadronization of the partons itself, so it is interfaced to PYTHIA after the final state partons are matched correctly[1].

For the calculation of the GMSB spectrum, decays, and masses, the ISASUGRA program, which is part of ISAJET 7.69 [31], was utilized. ISASUGRA takes as input the GMSB parameters introduced in Sec. 2.5 and solves the corresponding renormalization group equations. The output is a full spectrum of SUSY particles and branching ratios which can be interfaced with another event generator.

The CMS detector is modelled with the simulation program Geant4 [32]. With it, all detector parts are described in size, position, and the materials they are composed of. Electromagnetic and hadronic interactions of particles crossing the detectors are simulated. The response (signal-building) of active detector materials to traversing particles is calculated in the so-called *digitization* of the signals. Ideally, the digitized signals should emulate the real detector response to penetrating particles of all relevant types and energies. During detector operation with collisions, as the understanding of its response to real particles grows and changes, the simulation is often adjusted accordingly.

4.2 Physics Object Reconstruction

This section is dedicated to the reconstruction of physics objects, from the calculation of momentum four-vectors and other observables to the assignment of particle types from the various measurements obtained from the subdetectors of CMS. Objects and quantities relevant to this work are described in the following.

[1] For all samples signified as "MadGraph", the actual output comes from PYTHIA.

4.2.1 Hits, Tracks, and Energy Loss

Hit Reconstruction

Reconstruction of particle tracks begins with the local reconstruction of hits which consist of signals of neighboring strips or pixels, called clusters. Any strip with a signal-to-noise ratio $S/N > 3$, or any pixel with $S/N > 6$, serves as seed and neighboring strips with $S/N > 2$ (pixels with $S/N > 5$) are added to the cluster [21]. Pixel clusters are required to have $S/N > 10.1$ for their total charge. For the strip detector, the signal of a cluster has to be greater than five times the root-mean-squared value of the included strip noises. Furthermore, one dysfunctional strip may be included in a cluster. In the strip tracker, minimally ionizing particles have on average $S/N \sim 20$ per 300 μm of crossed silicon. The total cluster charge distribution has a long tail which is due to δ-electrons[2]. The most probable value (MPV) of the distribution is 300 ADC counts per mm of crossed silicon for MIPs. The gain of the APVs in the SST is calibrated to this value with particle tracks and varies by up to 20 % for each APV pair. The cluster position is determined from the weighted mean of the strip positions, with the weight depending on the signal strength of each strip. The final hit position, which is used for track reconstruction, is obtained by correcting the cluster position for the Lorentz-angle. The Lorentz-angle is the angle at which ionization electrons drift in the module with respect to the normal of the module surface. This effect is caused by the crossed electric (from the applied read-out voltage) and magnetic (from the CMS solenoid) fields inside the modules.

Track Reconstruction

Track reconstruction in CMS is performed with the Combinatorial Track Finder (CTF) algorithm which utilizes a Kalman filter [33]. The initial stage of the CTF algorithm is seed finding. Each track has five helix parameters fully describing it, therefore at least three points are needed to start the trajectory calculation. These can be three tracker hits or two hits and a beam spot or vertex position. Ideally, all seed hits are measured in the precise pixel detector but strip hits are used for seeding, as well. The seed trajectory is then propagated outward to search for compatible hits. With each hit that is added to the track, its parameters and therefore the propagation are updated until the last layer of the tracker is reached or no more hits are found. Overlapping tracks are removed if they

[2] δ-electrons are ionization electrons that are energetic enough to ionize neighboring atoms themselves.

share at least half of their hits with any other track. Then, the least-squares fit of all hits belonging to a track is repeated to obtain its final parameters. During this step, single hits with high χ^2 above a certain threshold (called *outliers*) are removed from the track. In order to improve track reconstruction efficiency and to reduce the fake rate, the previous steps are repeated in a six-step iterative procedure. The difference between the six steps is mainly the seed finding, but impact parameter and transverse momentum cuts are also varied.

Energy Loss Measurement

The energy loss per unit distance of charged particles, henceforth referred to as dE/dx, can only be measured by the silicon modules of the CMS tracker. It is the only observable that can discriminate charged hadrons like pions, kaons, and protons. While the pixel detector can and will be used to measure dE/dx, only the SST modules have been used thus far for this measurement. To calculate the energy loss per hit, $\Delta E/\Delta x$, the following approximation [34] is used[3]:

$$\Delta E/\Delta x = \frac{\Delta E \cdot \cos\Theta}{\Delta L}, \tag{4.1}$$

where ΔE is the energy deposited by a particle in the module, as measured by the cluster signal. For this, a normalization factor of $250 \cdot 3.61$ eV per ADC count is used to convert the cluster signal into an energy, where 250 is the number of electron-hole pairs per ADC count in the SST, and 3.61 eV is the energy needed to produce one such pair. ΔL is the thickness of the module, and Θ is the incident angle of the particle with respect to the module normal. The $\Delta E/\Delta x$ distribution, just like the cluster charge distribution on which it depends, has a long tail towards high values. Therefore, the mean dE/dx of a particle track cannot simply be taken as the arithmetic mean of the individual measurements. An unbinned Landau fit to the distribution of hit $\Delta E/\Delta x$ values is the natural approach to obtain an MPV of the particle dE/dx but, due to the high computing time of unbinned fits, a harmonic mean estimator is used by CMS. The general mean of grade k of a variable x is defined as:

$$M_k(x_1, ..., x_n) = \left(\frac{1}{n} \cdot \sum_{i=1}^{n} x_i^k \right)^{\frac{1}{k}}. \tag{4.2}$$

[3]To avoid confusion, the term $\Delta E/\Delta x$ will be used for individual hit measurements, while dE/dx will be used for the estimated track energy loss.

The parameter k was chosen to be -2, which gives a similar performance as a Landau fit [34], although at a reasonable computing time. The exponent of -2 applied to the hit $\Delta E/\Delta x$ measurements x_i implies that large values are downweighted significantly, thus pushing the result towards lower values. The resulting mean is used as an estimate of particle dE/dx and has an MPV of about 3 MeV/cm for MIPs.

Tracks with momenta as low as a few hundred MeV can be reconstructed with the CMS tracker. Close to this threshold, kaons, protons, and deuterons can be identified with energy loss measurements, whereas pions, muons, and electrons are always reconstructed as MIPs.

4.2.2 Muons

In CMS, muons are reconstructed in both the muon system and the tracker [21, 35]. Starting with an L1 trigger object in the muon system, local track segments are reconstructed in the DT and CSC stations. In the DTs, a straight line is fitted to the $r-\phi$ and (if available) $r-z$ measurements independently before being combined into the final segment with all track and hit parameters. The final position resolution in the $r-\phi$ direction is about 70 μm with a directional resolution of about 2 mrad. In the CSCs, a track segment is accepted if at least four out of six layers have hits compatible with a straight-line fit which takes the two-dimensional hit information into account simultaneously. For the reconstruction of a track in the muon system (*stand-alone muon*), a Kalman filter technique is used to combine the measurements from the different stations. DT track segments are treated as individual measurements, whereas CSC hits are refitted for the final track. RPC hits are also added individually to any muon track. The fit is performed inside-out with a trajectory update after each added measurement, followed by an outside-in fit which is extrapolated to the nominal IP for the final track parameters.

All tracks are by default muon candidates, but after extrapolating the trajectory to the muon system (taking into account energy loss in the calorimeters and positional uncertainty due to multiple scattering), those tracks without a matching track segment are not considered muon candidates. Any track with at least one matching segment in the CSCs or DTs is called *tracker-only muon*.

If the outside-in fit of a stand-alone muon track finds a matching tracker track, a global refit of both tracks into one *global muon* track is performed. This is usually the preferred

object for unambiguous muon identification.

4.2.3 Jets

Jets, being collimated streams of hadrons, are reconstructed mainly in the calorimeters, although the tracker plays an increasing role in improving and validating the conventional measurements.

Calorimeter tower energies are clustered by the Anti-k_T jet algorithm [36] with a cone size of up to $\Delta R = \sqrt{\Delta\phi^2 + \Delta\eta^2} = 0.5$ to form so-called *calorimeter jets*. Up to pseudorapidities of $|\eta| < 1.4$, one HCAL tower's base area corresponds to exactly 5×5 ECAL cells, thus forming one calorimeter tower. At $1.4 < |\eta| < 3.0$, the projection of ECAL cells onto HCAL towers is non-constant, while at $|\eta| > 3.0$, measurements from the hadron forward towers are used.

Another method of jet reconstruction is the combination of tracks and calorimeter towers in the so-called *jet-plus-tracks (JPT)* algorithm. However, the JPT method is superseded by the *Particle-Flow* algorithm [37], which incorporates information from all subdetectors to improve energy and spatial resolutions. Particle-Flow aims at reconstructing all particles in an event and adds them to a list to be clustered by the Anti-k_T algorithm, again with a cone size parameter of $\Delta R = 0.5$. Thus, charged hadrons are first identified by tracks from the silicon tracker, whereas photons and neutral hadrons are reconstructed in the calorimeters [38]. The resulting jets, called *Particle-Flow jets*, are used in this work.

Due to the non-uniform response of the CMS calorimeters to particles of differing momenta and pseudorapidities, the measured jet energies have to be corrected in the offline reconstruction. The "true" jet energies are of course unknown in data and therefore have to be evaluated from simulation, where the generated four-vectors of the particles constituting a jet are accessible. Reconstructing simulated jets with the same algorithms as outlined above results in correction factors for the measured jet energies, which depend on p_T and η. At CMS, this jet energy calibration is performed in a factorized approach [40]. Three correction factors, the $offset$, $relative$, and $absolute$ corrections are determined separately [38]. The offset correction takes into account additional calorimeter energy coming from electronics noise and pile-up proton-proton collisions. The jet energy dependence on the layout of the detector is addressed by the relative correction which therefore depends on η. The absolute correction removes the p_T-dependence of the jet response. For the

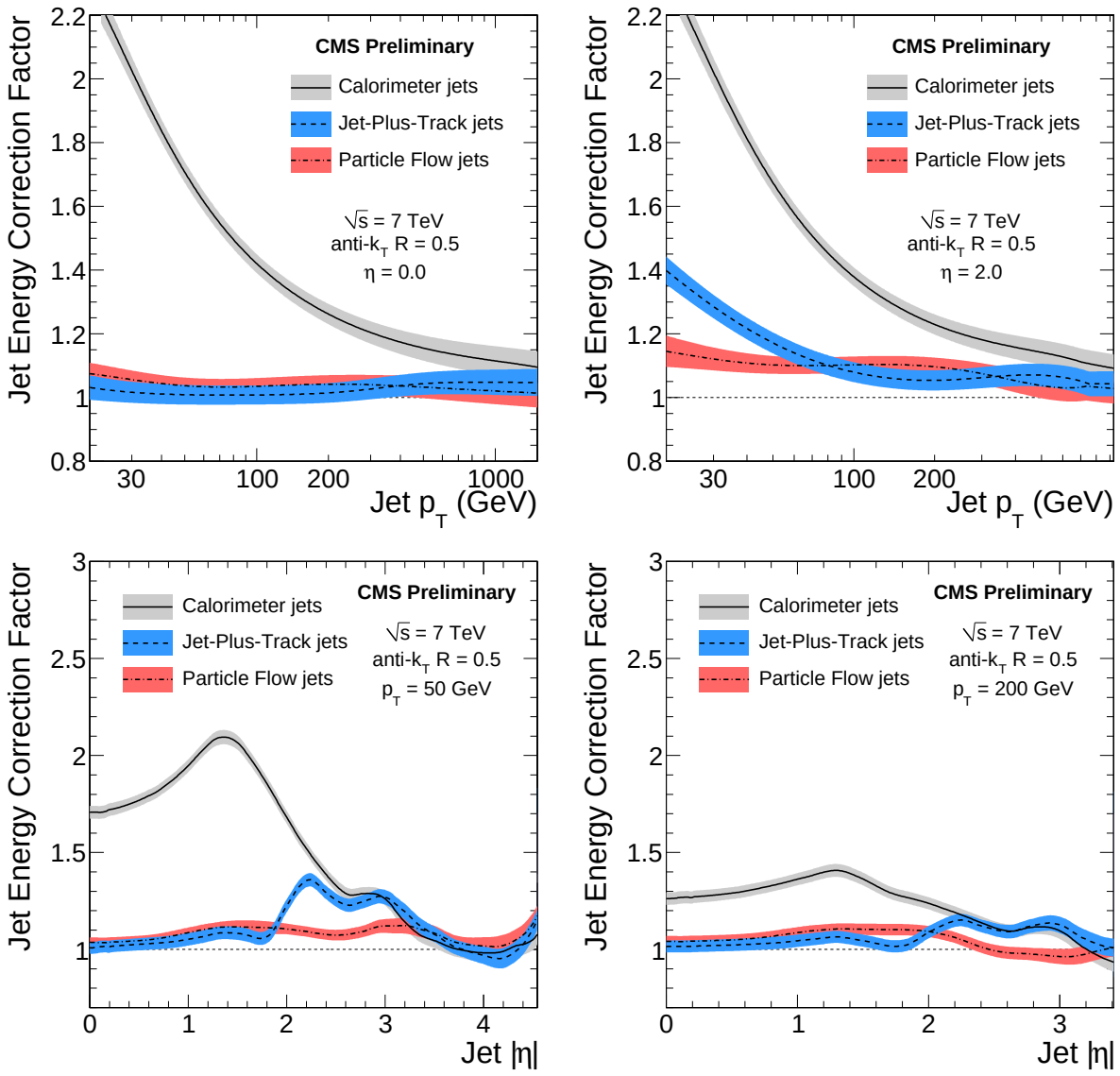

Figure 4.1: Total jet energy correction factors as a function of p_T for different values of η (top) and as a function of η for different values of p_T (bottom). Distributions for calorimeter, JPT, and Particle-Flow jets and their uncertainties are shown for jets reconstructed with the anti-k$_T$ algorithm. From [39].

determination of the corrections from simulation, the offset correction was actually not separated from the relative and absolute corrections, so that only two factors were used. For the validation of these two factors with collision data, the momentum balance of di-jet and photon-jet events were analyzed, leading to small corrections to the jet energy

corrections used in collision data [38].

The total jet energy correction factors determined [39] for all three jet reconstruction methods, calorimeter, JPT, and Particle-Flow, are shown in Fig. 4.1 as functions of p_T and $|\eta|$, respectively. The corrections are much smaller, especially at low transverse momenta, for JPT and Particle-Flow jets than for calorimeter jets. Furthermore, the variation with η is the smallest for Particle-Flow jets.

4.2.4 Missing Transverse Energy

Missing energy transverse to the beam line arises primarily when weakly interacting particles are produced in collisions[4]. The resulting imbalance of final-state energies is caused by the lacking energy measurement of these particles. The magnitude and direction of missing transverse energy are obtained by calculating the total negative vector sum of the transverse momenta of all measured particles in an event with the Particle-Flow algorithm [41]. Jets were corrected as described in Sec. 4.2.3 before being included in the calculation [37]. Due to the finite measurement precision of the CMS subdetectors, measurements of missing transverse energy (MET) are smeared, usually resulting in small values of MET even when none is expected from a process.

4.2.5 Software

The software framework of the CMS experiment is called CMSSW, which is used for online and offline processing of data. Version 3.8.7 of CMSSW was used for this work. The ROOT framework [42] was used to display data in histograms and graphs throughout this thesis. Both CMSSW and ROOT are based on the C++ programming language.

[4]A full missing energy measurement is precluded because longitudinal information is lost due to the non-detection of final-state proton remnants going down the beam-pipe. Further complicating matters would be the unknown initial state in proton-proton collisions.

Chapter 5

Stable Stau Search

The selection of events for collision and simulated data is elaborated in this chapter. First, the signature of simulated stable staus in the CMS detector and the corresponding Standard Model backgrounds are outlined. Then, the utilized data samples are described, followed by the sequence of selecting signal-like events. This includes triggers, selection of basic objects such as tracks, muons, and jets, and the enhancement of the signal-to-background ratio via cuts on discriminating observables.

5.1 Stable Stau Signal in CMS

In the GMSB scenario described in Sec. 2.5, staus are prevalently produced at the end of a chain of supersymmetric particles decaying into SM particles and lighter sparticles until the stau is reached. Usually, pairs of squarks or gluinos are produced at the start of this chain. Thus, several jets and leptons, including neutrinos, normally accompany each stau. The direct production of stau-pairs in an electroweak process is suppressed compared to the production of colored sparticles. Since the other sleptons are not much heavier than the stau (see Tab. 2.4), the production of slepton pairs which then decay into the stau also contributes to the cross section. Additional significant contributions come from the production of a neutralino and a chargino via a W boson, and chargino pair-production via a photon or Z boson. As the mass scale of the GMSB model increases, the electroweak processes give larger fractions to the total cross section because the slepton and neutralino/chargino masses increase slower than the colored sparticles' masses due to the renormalization group equations. At the highest mass scales studied in this work,

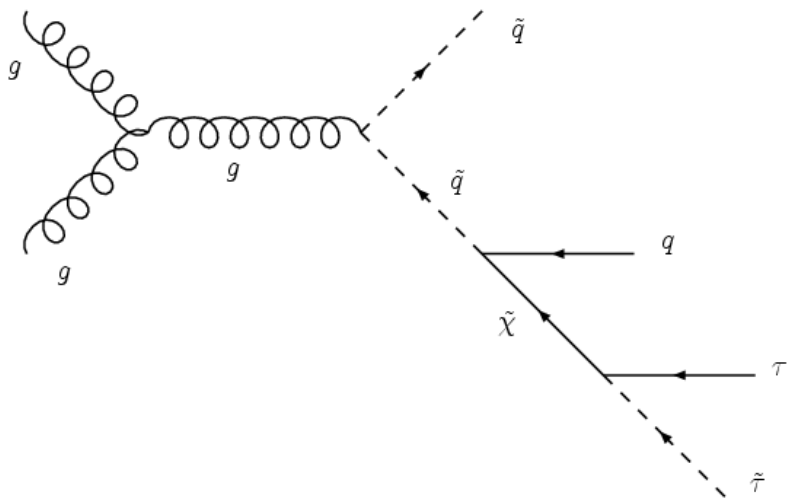

Figure 5.1: Feynman graph of a stau production process in GMSB via gluon fusion. Only one cascade branch is shown.

slepton and gaugino production outweighs that of colored sparticle production. Full mass spectra of all GMSB models studied in this thesis are given in App. B.

A diagram of SUSY-QCD production of squarks with a cascade decay ending in a stable stau is shown in Fig. 5.1. The cascade shown is the shortest one possible for squark production and many more intermediate decays are very probable. The electroweak production processes always have quarks in the initial state.

The generated transverse momentum and speed β of stable staus from simulations with three different GMSB parameter points are shown in Fig. 5.2. While many staus have $\beta \simeq 1$, a large fraction has lower speeds, which leads to high ionization in the silicon tracker modules as explained in Sec. 2.6. As the parameter Λ increases, higher squark and gluino masses give more overall momentum to the cascade decay products. Hence, staus with higher masses have harder p_T spectra. However, the mass increase of the staus outweighs the average momentum increase, leading to lower average speeds β.

Even though stable stau production is signified by large event activity, the high ionization of slow staus is unique enough to identify such events with the CMS detector. Particle tracks with high transverse momentum *and* high energy loss are not expected in any SM process, so the task is to find these tracks and to ensure that the energy loss measurement is well understood.

The stable stau essentially behaves like a very heavy lepton to the subdetectors of CMS,

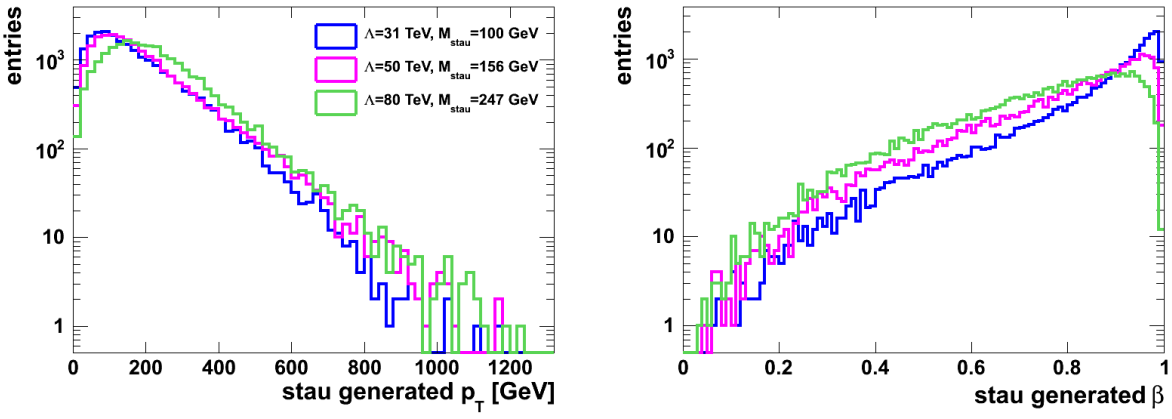

Figure 5.2: Generated stau transverse momentum (left) and speed (right) for three GMSB parameter points.

meaning it creates hits in the tracker and the muon system and traverses the calorimeters with small energy depositions. Thus, in the standard reconstruction algorithms of CMS, stable staus are usually tagged as muons. Very slow staus with $\beta \lesssim 0.5$ reach the muon stations during the next interval in the 25 ns read-out scheme of CMS[1], and will thus be reconstructed in the wrong event. Still, by far the most efficient triggers to select events with stable staus are muon triggers. In the signal simulation, a matching between trigger objects from the muon trigger with a threshold of $p_T = 9$ GeV to generator-matched stau muon candidates was performed. The resulting trigger efficiency is plotted as a function of the generated stau transverse momentum and displayed in Fig. 5.3. Efficiencies are shown for three samples with differing stau masses. The trigger turn-on moves to higher p_T for higher stau masses, because there are more slow staus at high masses, as shown in the β distributions in Fig. 5.2. At $p_{T,stau} \gtrsim M_{stau}$, the trigger efficiency surpasses 90 %. Thus, the trigger efficiency decreases slightly for higher stau masses. While this graph shows the probability of a stau-like object to trigger a muon trigger, the actual trigger efficiency for signal events is slightly larger since additional real, energetic muons can be produced in the SUSY decay chain. The total muon trigger efficiency for the sample with the stau mass of 100 GeV is 94.8 % while for the mass of 247 GeV it is 90.6 %.

Due to the high probability of stable staus being reconstructed as muons, the muon multiplicity expected from these events is high, especially since additional real muons can be produced in cascade decays. Thus, the muon multiplicity, along with the hard p_T

[1]The 25 ns interval corresponds to the bunch-crossing frequency at the LHC design luminosity.

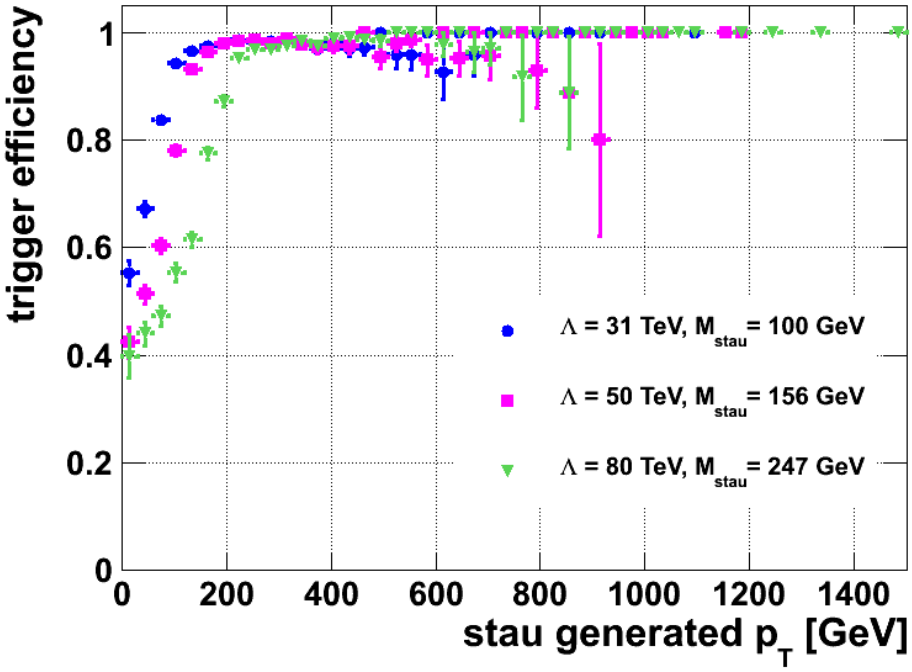

Figure 5.3: Fraction of signal events with at least one muon trigger object ($p_T \geq 9$ GeV) matched to a muon candidate that was matched to a generated stau four-vector, as a function of the generated stau transverse momentum. Three GMSB parameter points are shown.

spectrum of the staus, should differ significantly from Standard Model muon production processes.

5.2 Standard Model Backgrounds

The main signature of HSCPs, highly-ionizing tracks, only arise at very low momenta within the spectrum of the SM. Thus, at high momenta, the region of high energy loss is virtually devoid of SM background except for statistical fluctuations.

All possible sources of highly energetic muons from the SM are considered as backgrounds for the stable stau search. These include the production of top-antitop-pairs, where at least one W-boson decays leptonically into a muon and a neutrino. Likewise, single-top production, having a much lower cross section, contributes to the background, although only marginally with the amount of data analyzed in this work. The direct production of W-bosons with a subsequent decay into muon and neutrino is another important

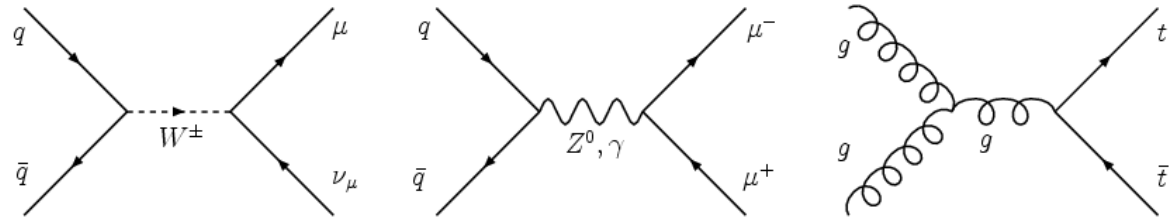

Figure 5.4: Leading-order Feynman diagrams of main SM background processes: single W production (left), Drell-Yan muon-pair production (center), top-pair production (right).

contribution, while W-pair production is similarly scarce as the single-top process. Furthermore, the production of opposite-sign muon pairs via quark annihilation into a Z-boson or an excited photon (referred to as Drell-Yan production) is another source of muons in the SM. Other di-boson production channels (WZ and ZZ) have lower cross sections than WW-production - which only marginally contributes to the SM background - and are neglected in this study. The aforementioned processes also have taus in the final state, a fraction of which decay into muons. Thus, the tau channel of these processes is considered, as well. Finally, QCD multi-jet events may produce muons in decays of charged pions and kaons, or B- and D-mesons. Leading-order Feynman diagrams of the main background processes are shown in Fig. 5.4. The diagrams represent the main contributions to these processes at the LHC.

5.3 Datasets

The CMS data from proton-proton collisions at 7 TeV center-of-mass energy recorded in 2010 are used in this search. Of the recorded total of 43.2 pb^{-1}, a "certified" amount of data corresponding to 35.8 pb^{-1}, where all detector subsystems were operational, is used. Only events that fired at least one single-muon trigger are considered for this analysis.

Simulated datasets used for comparison with the SM are: W-boson production with a subsequent leptonic decay; W-pair production with all possible final states; Drell-Yan production of two leptons, where the invariant mass of the two leptons is greater than 10 GeV; top quark pair-production ($\text{t}\bar{\text{t}}$); t-channel production of single top-quarks, which has a cross section of 21.5 pb and to which the s-channel (which is omitted) is suppressed by another order of magnitude; QCD multi-jet events with at least one muon (with $p_T > 15$ GeV) in the final state.

The QCD data sample was generated with PYTHIA and filtered for events containing muons. All other SM samples were generated with MadGraph, which is used to model the processes at tree-level. Furthermore, to account for the high number of hard jets observed in LHC proton-proton collisions, up to three (for the $t\bar{t}$ sample) or four (Drell-Yan and W samples) quarks or gluons are added to the final state[2]. The output of MadGraph was then processed with PYTHIA for the showering and hadronisation of colored objects.

The signal simulation was done with ISASUGRA whose output was processed with PYTHIA to create full events. Six signal samples with differing stau masses were created, as listed in Tab. 5.1. The varied parameter is the SUSY-breaking scale Λ which was introduced in Sec. 2.5. The resulting cross section falls rapidly with increasing Λ since all sparticle masses are proportional to Λ. For instance, the squark and gluino masses increase from about 700 GeV for $\Lambda = 31$ TeV to about 2 TeV for $\Lambda = 100$ TeV. The number of expected events for each sample corresponding to the analyzed luminosity of 35.8 pb^{-1}, assuming perfect detector acceptance, is given in the rightmost column of the table. For the three lower mass points, cross sections were calculated with Prospino2 [43, 44] at next-to-leading order (NLO), while for the higher-mass samples the leading-order (LO) cross sections from ISASUGRA were taken. The three high-mass points have too small numbers of expected events to be relevant for this search, so their cross sections were not determined to higher accuracy.

[2]This is done in lieu of a higher-order modelling of the original process, which would greatly increase the already high computing time demands of HEP event simulation.

Λ [TeV]	M_{stau} [GeV]	Cross section [pb]	Expected events	Calculation
31	100	1.63	58.4	NLO (Prospino2)
40	126	0.38	13.6	NLO (Prospino2)
50	156	0.10	3.6	NLO (Prospino2)
65	201	0.025	0.90	LO (ISASUGRA)
80	247	0.008	0.29	LO (ISASUGRA)
100	308	0.002	0.07	LO (ISASUGRA)

Table 5.1: Simulated signal samples by stau mass with the corresponding cross section, number of expected events for 35.8 pb^{-1}, and source of cross section calculation. Full mass spectra can be found in App. B.

Process	Cross section [pb]	Calculation
$W \rightarrow l\nu$	$31,314 \pm 1,558$	NNLO (FEWZ)
$WW \rightarrow X$	43.0 ± 1.5	NLO (MCFM)
$Z/\gamma \rightarrow ll$, $10 < M_{ll} < 50$ GeV	1,722	LO (MadGraph)
$Z/\gamma \rightarrow ll$, $M_{ll} > 50$ GeV	$3,048 \pm 132$	NNLO (FEWZ)
$t\bar{t}$	$157.5^{+23.2}_{-24.4}$	NLO (MCFM)
$t \rightarrow bl\nu$ (t-channel)	21.5 ± 1.1	NLO (MCFM)
QCD with muons	84,679	LO (PYTHIA)

Table 5.2: Simulated Standard Model processes with theoretical cross sections (and errors where available) and the source of their calculation.

Finally, the simulated processes were interfaced with the CMS detector simulation from Geant4. An overview of all simulated background samples and their theoretical cross sections, is given in Tab. 5.2. The cross section of top-pair production was obtained with MCFM [45], a program that performs next-to-leading order calculations of Feynman diagrams. The electroweak processes Drell-Yan and W-production were calculated at next-to-NLO [46]. However, for the Drell-Yan process with $M_{ll} < 50$ GeV and the QCD process, no calculation was available, therefore the leading-order cross section from the generator is given. Simulated events are normalized to data according to their cross sections and number of generated events.

5.4 Event Selection

This section is devoted to the selection of events containing highly energetic and highly ionizing muons, beginning with the triggers used for collision data and simulations. Since the energy loss measurement is performed using silicon strip hits of the muons, track quality criteria are detailed. Furthermore, the cascade of particle decays that usually precedes the production of a stau in GMSB produces many hadronic jets, therefore jets will also be used to identify possible stable stau event candidates. The cuts applied on physics objects to obtain a control (SM-dominated) selection are described in this section.

In the following, graphs showing different SM process simulations are arranged such that the expected events from all processes are stacked up to one full distribution which is

then compared to the observed data. Each type of SM process is given a distinct color in the graphs. The samples of top-pair production and single-top production are summed up and labelled "top". The fraction of single-top events in the top distributions is diminutive in all figures. The GMSB model process with a stau mass of 100 GeV ($\Lambda = 31$ TeV) is shown as a blue line for comparison and labeled "signal, $\Lambda = 31$ TeV". All simulated samples are normalized to the integrated luminosity of 35.8 pb^{-1} to determine the number of expected events.

An overview of all quality criteria used in the physics objects selection is given in Tab. 5.3. The cuts for each physics object (vertices, muons, and jets) are explained in the following sections. For the motivation of the cuts, some of the criteria from Tab. 5.3 may not be applied, which will be stated in the discussion of each physics object.

5.4.1 Triggers

As explained above, simulated muon triggers are sufficient to identify a large fraction of stable stau events. Therefore, muon triggers are used on collision data and simulations to select events of interest for this search. The corresponding high level triggers accept events containing at least one reconstructed muon candidate with transverse momentum thresholds of 9, 11, and 15 GeV, respectively. Trigger thresholds were increased to control the trigger rates as the instantaneous luminosity was increased during the 2010 LHC run, since a maximum of about 200 events per second can be stored by the CMS data acquisition system (see Sec. 3.2.6). The simulated data samples for the SM backgrounds and the stau signal only have the 9 GeV transverse momentum threshold as part of the trigger simulation. Since the muons selected for further investigation have at least $p_T > 50$ GeV (see below), which is well above the trigger turn-on at the thresholds, the efficiency of the triggers can safely be assumed to be above 90 % [47]. This is true for both real and simulated triggers, which is why simulated triggers are assumed to have the correct scale with a certain systematic uncertainty, as discussed in Sec. 6.1.

5.4.2 Primary Vertex

In proton-proton collisions at 7 TeV with instantaneous luminosities in excess of 10^{32} $\text{cm}^{-2}\text{s}^{-1}$, multiple interactions per bunch crossing are quite common. This leads to many primary vertices being reconstructed in the interaction region. The main cause of multiple primary

vertices is called *pile-up*, indicating that more than one proton-proton collision takes place during one bunch crossing.

Vertices are reconstructed using tracks that are extrapolated to the beam-line via transverse (d_{xy}) and longitudinal impact parameters (d_z). Groups of tracks that originate in a small region along the beam-line (separated no more than $z_{sep} = 1$ cm) are used in a fit to determine the position of the vertex [48]. For this, each track is given a weight w_i (between 0 and 1) according to their compatibility to the vertex [49]. The effective number of degrees of freedom of a vertex is defined as $n_{dof} = 2(\Sigma_{i=1}^{nTracks} w_i) - 3$. This quantity is used to select primary vertices coming from hard proton-proton interactions [48]. In practice, each event is required to have at least one primary vertex with $n_{dof} \geq 4$ that is loosely

Physics object	Selection criteria
trigger	1+ muon with $p_T > 9$, 11, or 15 GeV
	(see Sec. 5.4.1)
1+ **primary vertex**	$\lvert d_{xy}\rvert < 2$ cm
	$\lvert d_z\rvert < 24$ cm
	$n_{dof} \geq 4.0$
1+ **muon candidate**	$p_T > 50$ GeV
	$\lvert\eta\rvert < 2.4$
	$\lvert d_z\rvert < 0.1$ cm (w.r.t. primary vertex)
	global track $\chi^2/n_{dof} < 10.0$
	$n_{hits,\,tracker} > 9$
	$n_{hits,\,pixel} > 0$
	$n_{hits,\,muon} > 0$
	$I_{rel} < 0.05$
	$\Delta R_{jet} > 0.5$
	$M_{\mu\mu} > 12$ GeV & $\lvert M_{\mu\mu} - M_{Z^0}\rvert > 15$ GeV
2+ **jet candidates**	$p_T > 30$ GeV
	$\lvert\eta\rvert < 2.4$
	$\Delta R_{muon} > 0.1$
	noise & fake rejection (see Sec. 5.4.4)

Table 5.3: Complete list of control selection criteria for considered physics objects.

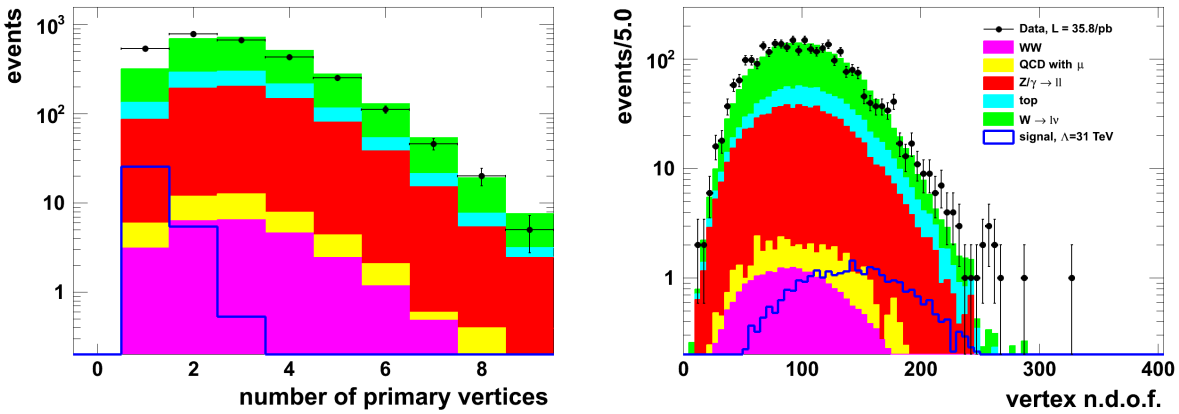

Figure 5.5: Control selection: number of reconstructed primary vertices (left) and number of degrees of freedom, n_{dof}, of the primary vertex with the best vertex fit (right). The signal simulation does not include pile-up.

compatible with the primary interaction region, $|d_{xy}| < 2$ cm and $|d_z| < 24$ cm. Figure 5.5 shows the n_{dof} of the primary vertex with the best fit quality (i.e. lowest χ^2/n_{dof}) after all control selection cuts were applied. The left plot of Fig. 5.5 shows the number of reconstructed primary vertices per event. The mean of this distribution is about 2.7 in collision data, showcasing the effect of pile-up. The SM simulations are corrected for the pile-up observed at the end of the 2010 run, when the average instantaneous luminosity was about 10^{32} cm^{-2}s^{-1}. Since the data sample encompasses a large range of event rates ($\sim 10^{26} - 10^{32}$ cm^{-2}s^{-1}), the average pile-up of the 2010 run is lower. Therefore, the SM simulations slightly overestimate the observed pile-up. This has a negligible effect on the selection of events with energetic muons and jets, however. No pile-up simulation was performed for the signal sample. The effect of this (which is already small for the SM background) on the signal selection is deemed negligible due to the high overall energies present in the signal processes.

5.4.3 Muons

Reconstructed muon candidates are required to have traversed the detector in the fully instrumented region of $|\eta| < 2.4$ and have a transverse momentum of at least 50 GeV. The latter cut already reduces much of the SM background, while not affecting the signal efficiency very much. As seen in Fig. 5.2, the transverse momentum requirement cuts into

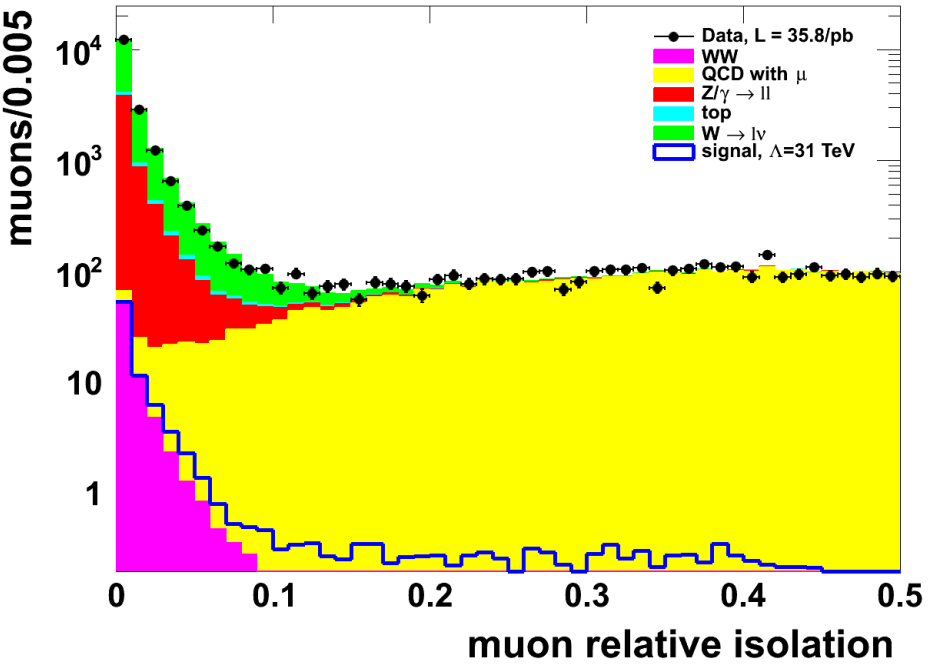

Figure 5.6: Relative isolation of muon candidates for the control selection without cuts on I_{rel} and jet multiplicity (see text for details).

the rising flank of the signal p_T distribution. Candidates are accepted if they have a global track with at least ten hits in the silicon tracker of which at least one has to be in the pixel detector, and at least one hit in the muon system. If the quality of the global track fit is too low, i.e. the χ^2/n_{dof} exceeds 10, candidates are rejected. The track quality is highly correlated with the minimum number of hits required, thus only very few muon tracks have $\chi^2/n_{dof} > 10$ as well as ten or more hits in the silicon tracker. Corresponding figures for the track quality of muons after the control selection are shown in Sec. 5.4.5.

Furthermore, muon candidates are required to be isolated from other activity in the event. This is important for a clean energy loss measurement since overlapping tracks can lead to higher-than-expected dE/dx values. The relative isolation of an object with respect to other tracks and calorimeter hits in its vicinity is measured with the I_{rel} variable:

$$I_{rel} = \frac{I_{tracker} + I_{ECAL} + I_{HCAL}}{p_T}, \tag{5.1}$$

where the I_x are the cumulated transverse momenta (for the tracker) or transverse energies (for the calorimeters) of all particles inside a cone of $\Delta R = \sqrt{\Delta\phi^2 + \Delta\eta^2} = 0.3$ (0.4

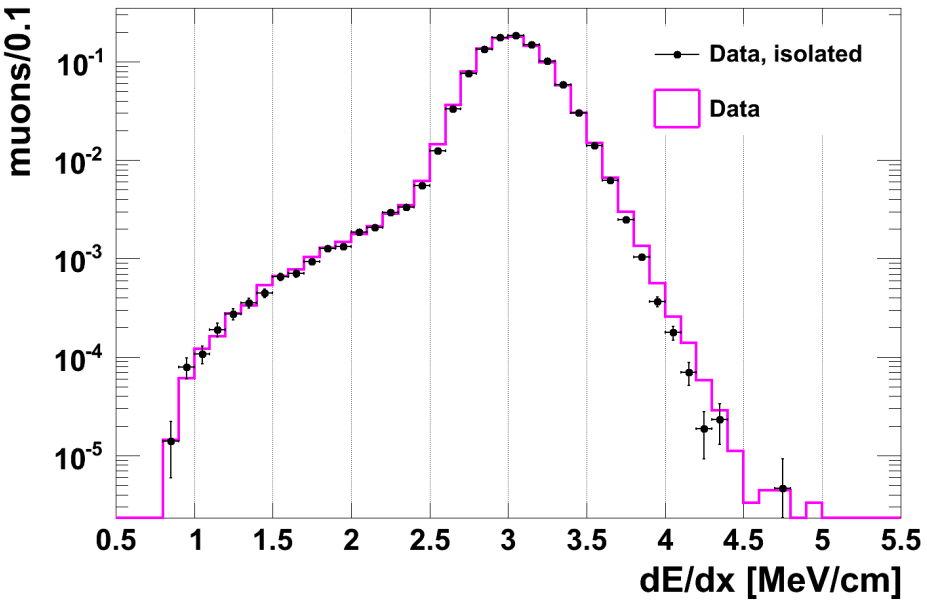

Figure 5.7: Energy loss measurements for isolated muons (black dots) compared with non-isolated muons (magenta line) from collision data. Distributions are normalized to unity for comparison. Note that much larger statistics are shown compared to the control selection (see text for details).

for the HCAL) around an examined physics object with transverse momentum p_T. The distribution of this variable for muon candidates, without applying the jet selection and the cut on I_{rel}, is shown in Fig. 5.6. The long tail of this distribution is dominated by QCD events, where muons are predominantly produced in heavy flavor meson decays. Thus, only muon candidates with $I_{rel} < 0.05$ are accepted for further investigation. The signal distribution of the relative muon isolation has a similar shape as the added SM backgrounds, peaking at zero. The cut on I_{rel} keeps more than 90 % of the signal but does not increase the signal-to-background ratio. Its purpose is to reduce the background from QCD multi-jet events and to select clean muons for untainted energy loss measurements. To showcase this, dE/dx distributions for muons selected as outlined here (although with $p_T > 20$ GeV to increase statistics) are compared in Fig. 5.7 with and without applying the isolation criteria detailed below. Also, no jet criteria are required for this distribution in order to increase statistics. This leads to a selection of about 800,000 muon candidates in the data, of which about 200,000 pass the isolation requirements. It is apparent that the distributions agree well around the most probable value of about 3 MeV/cm, but at values above 3.5 MeV/cm the non-isolated muons have a higher tail.

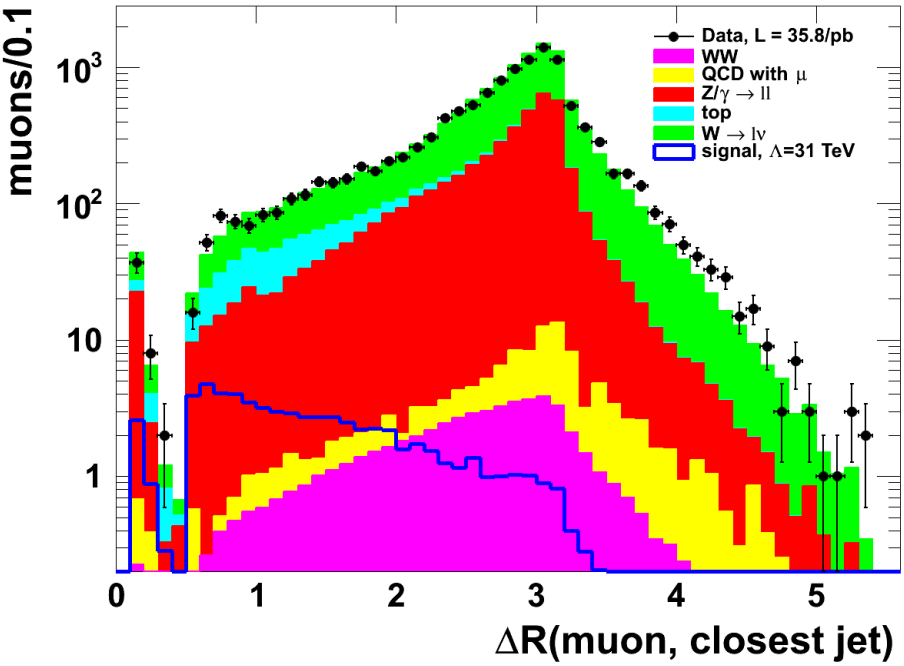

Figure 5.8: Distribution of minimal ΔR between selected muon candidates and selected jets for the control selection without cuts on ΔR and jet multiplicity (see text for details).

Despite the cut on I_{rel}, muons are sometimes reconstructed altogether as jets. To avoid these mismeasurements, a spatial separation of muons from jets is required. This is achieved by requiring a ΔR of greater than 0.1 between a selected jet (see next section) and a muon candidate. The distribution of ΔR between muons and the corresponding closest jets is shown in Fig. 5.8. For this figure, only one jet candidate was required. The first bin of 0 to 0.1 is empty due to the aforementioned ΔR cut, and the region between 0.1 and 0.5 has a steeply falling muon spectrum. This is due to the jet cone radius of up to $R = 0.5$, in which real muons may still exist or be produced from meson decays. These are removed by requiring that muons must be isolated from jets by $\Delta R > 0.5$. The spectrum above $\Delta R = 0.5$ rises toward a maximum at π, where most muons are back-to-back with a jet in the transverse plane. After that, the spectrum falls steeply as there are few events with large spatial gaps in detector activity.

Finally, for all events with at least two muon candidates of opposite charge, all possible combinations of opposite-sign di-muons are checked for compatibility with decay from a Z-boson ($M_Z = 91$ GeV) or a meson (the heaviest being the Υ, $M_\Upsilon = 9.5$ GeV) by calculating

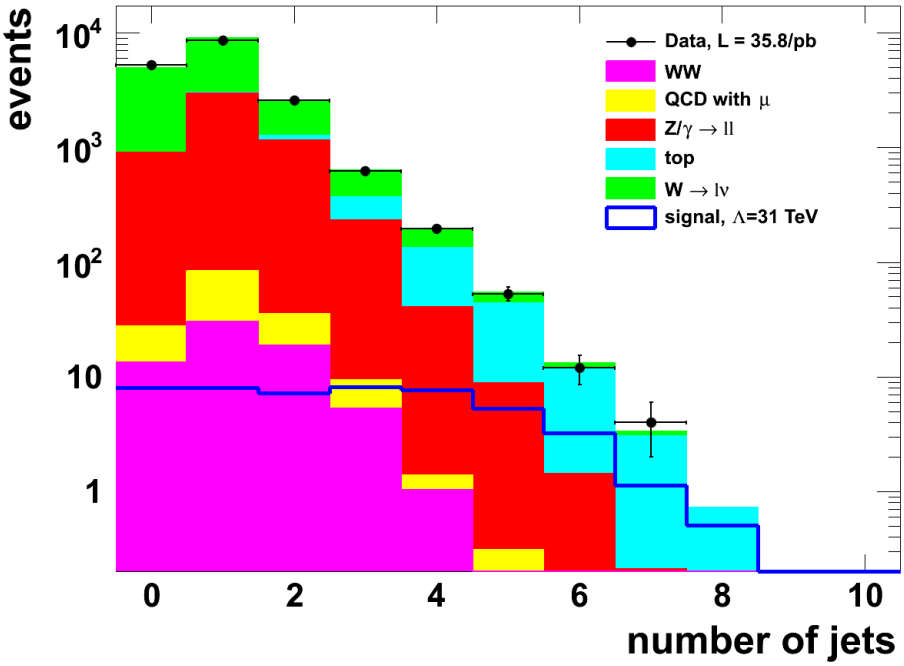

Figure 5.9: Number of selected jets for the control selection without the cut on jet multiplicity.

their invariant mass $M_{\mu\mu}$. Candidates which have an invariant mass of less than 12 GeV or between 76 and 106 GeV are discarded.

Muon candidates which satisfy all of the aforementioned criteria will henceforth be referred to as *selected muons*.

5.4.4 Jets

Hadronic jets are required to have transverse momenta of at least 30 GeV and be reconstructed within $|\eta| < 2.4$. The cut on $|\eta|$ is motivated by the boundaries of the silicon tracker, which is needed to take advantage of the Particle-Flow algorithm (see Sec. 4.2.3) which was used to reconstruct jets. In order to avoid noise and mismeasurements from the calorimeters, additional cleaning cuts are applied to the jets. The fraction of jet energy coming from neutral hadrons, photons, or electrons may each not exceed 99 %. These criteria also prevent photons or electrons from being identified as jets. Furthermore, the fraction of jet energy originating from charged hadrons must be greater than zero, as does the minimum number of charged particles inside the jet. Finally, all jets are required to

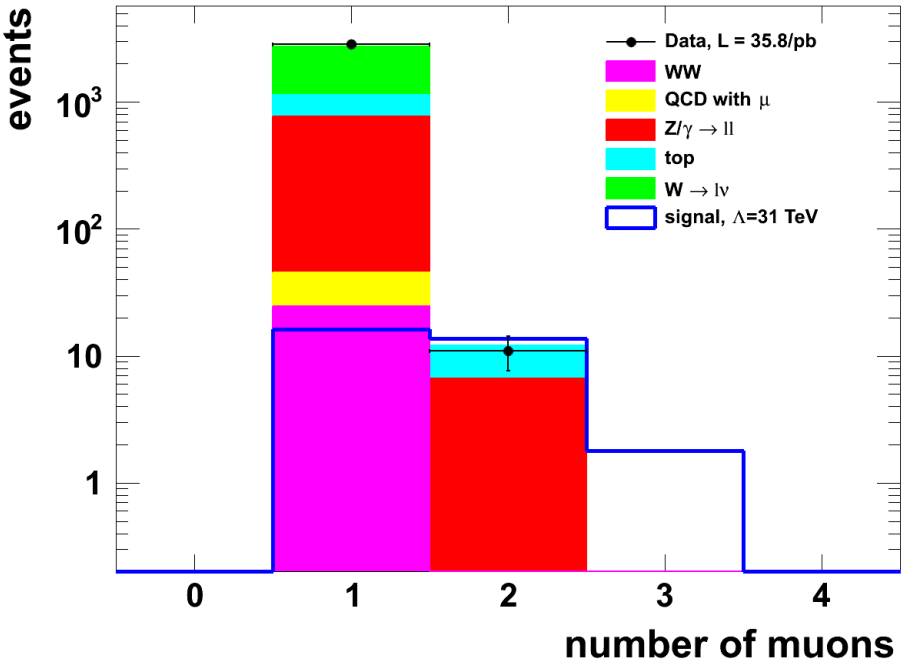

Figure 5.10: Control selection: number of selected muons per event.

consist of at least two particles (as defined by the Particle Flow algorithm) in order to qualify as a good Particle Flow jet. These cleaning cuts do not reject many jets in the final analysis, but they make sure that mismeasurements are rejected with high efficiency.

The number of jets meeting the above requirements, called *selected jets* from now on, is shown in Fig. 5.9 for events with at least one selected muon. There is a very good agreement between data and SM simulation, which show a peak at one with a steep decline for higher multiplicities. The shape of the signal distribution is discussed in the next section.

5.4.5 Control Selection

The control selection is made in order to validate the reconstructed kinematics of physics objects by comparing collision data and simulations. In selecting muons and jets at reasonably high momenta and multiplicities, the event yield is reduced significantly to 2860 events in data. In this study, where the signal cross sections are very low, the control selection should consist mostly of SM events which can be used to study the systematics without being signal contaminated.

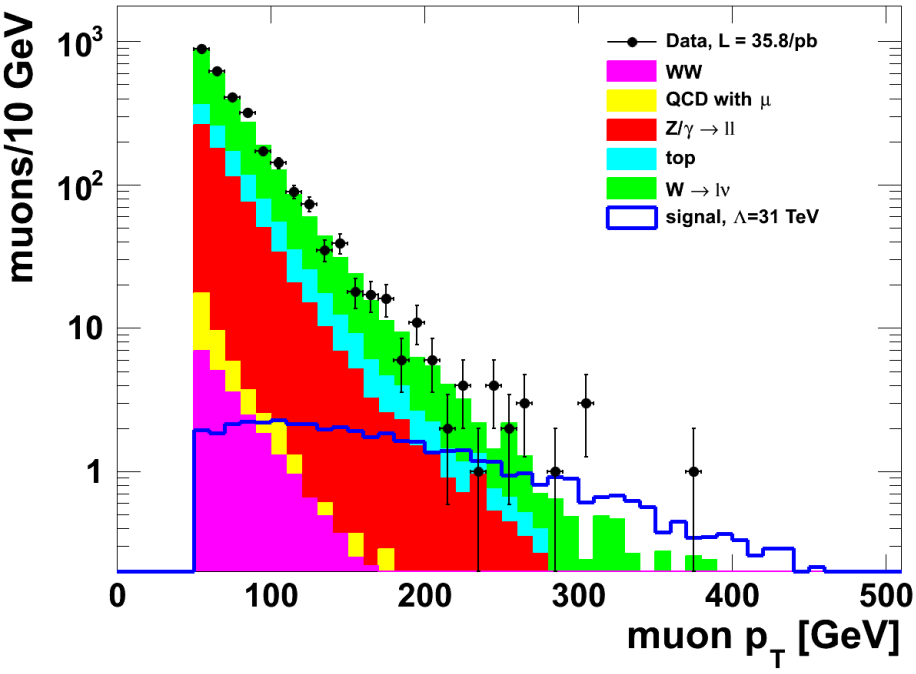

Figure 5.11: Control selection: transverse momentum distribution of selected muons.

In addition to requiring at least one selected muon, a cut on the selected jet multiplicity of at least two is imposed. This is done to enhance the signal-to-background ratio significantly, since the signal distribution for the number of jets is almost flat up to about five jets, whereas the SM distribution falls off steeply, as shown in Fig. 5.9. The complete control selection criteria, introduced in the preceeding sections, are summarized in Tab. 5.3.

The number of selected muons is shown in Fig. 5.10. The number of observed events in each bin agrees well with the expectation from the summed backgrounds. After the control selection, events with more than two selected muons are neither observed in data nor expected from Standard Model simulations. For the GMSB signal, a little more than one event is expected with three or more selected muons. While two or more muons are expected in the signal due to the mandatory pair-production of staus, many signal events with only one selected muon are expected. This is owed to the p_T cut of 50 GeV, and to the fact that staus just above this p_T-threshold have a reduced reconstruction efficiency in the muon chambers due to their possible (if $p_{\tilde{\tau}} < m_{\tilde{\tau}} = 100$ GeV) late arrival there.

The transverse momentum distribution of selected muons is shown in Fig. 5.11. A good agreement between data and SM simulation is observed, whereas the signal spectrum is

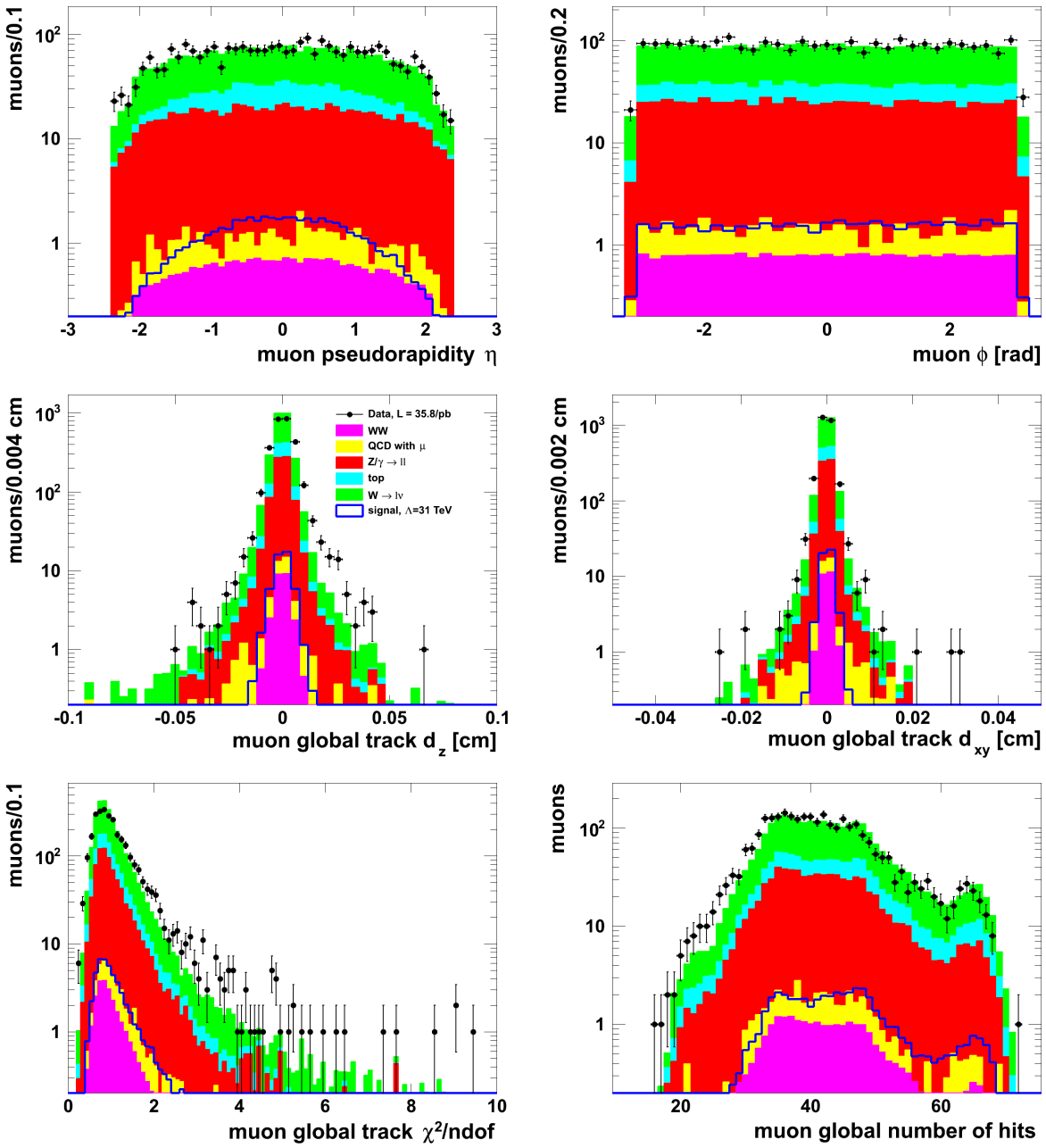

Figure 5.12: Control selection: global muon track distributions of pseudorapidity (top left), azimuthal angle (top right), longitudinal (center left) and transverse (center right) impact parameters, track fit quality χ^2/n_{dof} (bottom left), and total number of hits (bottom right).

much harder but too limited by statistics to have much discriminative power at this stage.

Distributions of pseudorapidity and azimuthal angle of selected muons are displayed in

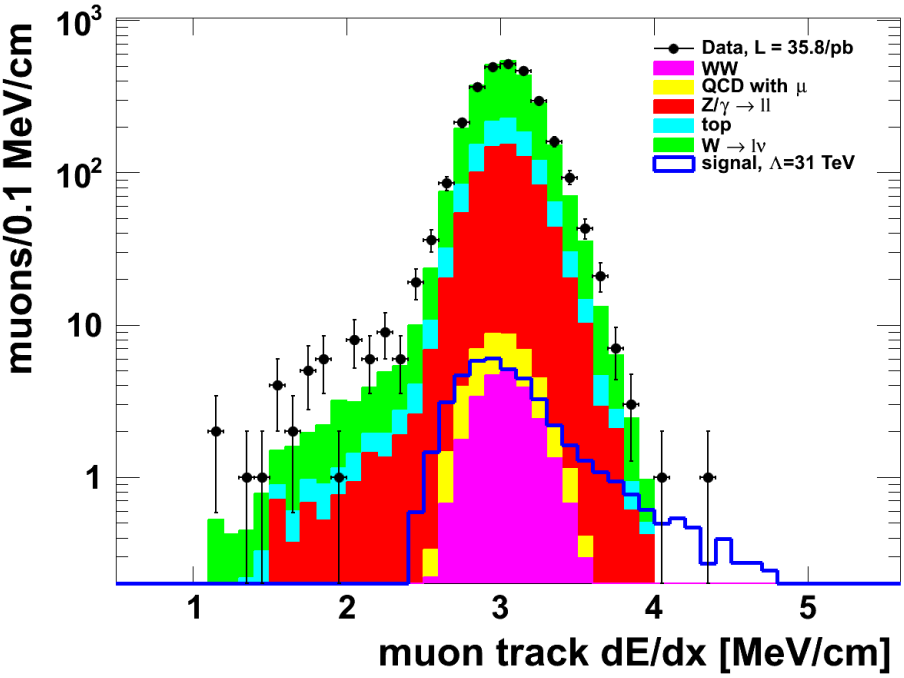

Figure 5.13: Control selection: distribution of track energy loss per unit length (dE/dx) of selected muons.

the top row of Fig. 5.12. In the signal, muons are produced more centrally than in the SM. The azimuthal angle distribution is flat, as expected, and agrees well between data and simulation.

The transverse and longitudinal impact parameters of the global muon track are shown in the middle row of Fig. 5.12. These values are measured with respect to the primary vertex with the highest fit quality in the event (see Sec. 5.4.2). These distributions are wider in data than in simulation, especially for the longitudinal impact parameter. The global muon track fit quality (χ^2/n_{dof}) and number of hits are shown in the bottom row of Fig. 5.12. These quantities also differ a bit between data and simulation, which is most likely due to the unknown misalignment of the tracker and muon chambers. Small shifts of the subdetectors result in significant changes of track-to-hit residuals and thus in χ^2/n_{dof}. For simulations, the positions and rotations of all subdetectors are shifted randomly to account for the real shifts observed with data. A precise knowledge of the relative alignment between tracker and muon system is especially important for the global track fit. The difference in the track fits between data and simulation may also be responsible for the discrepancies

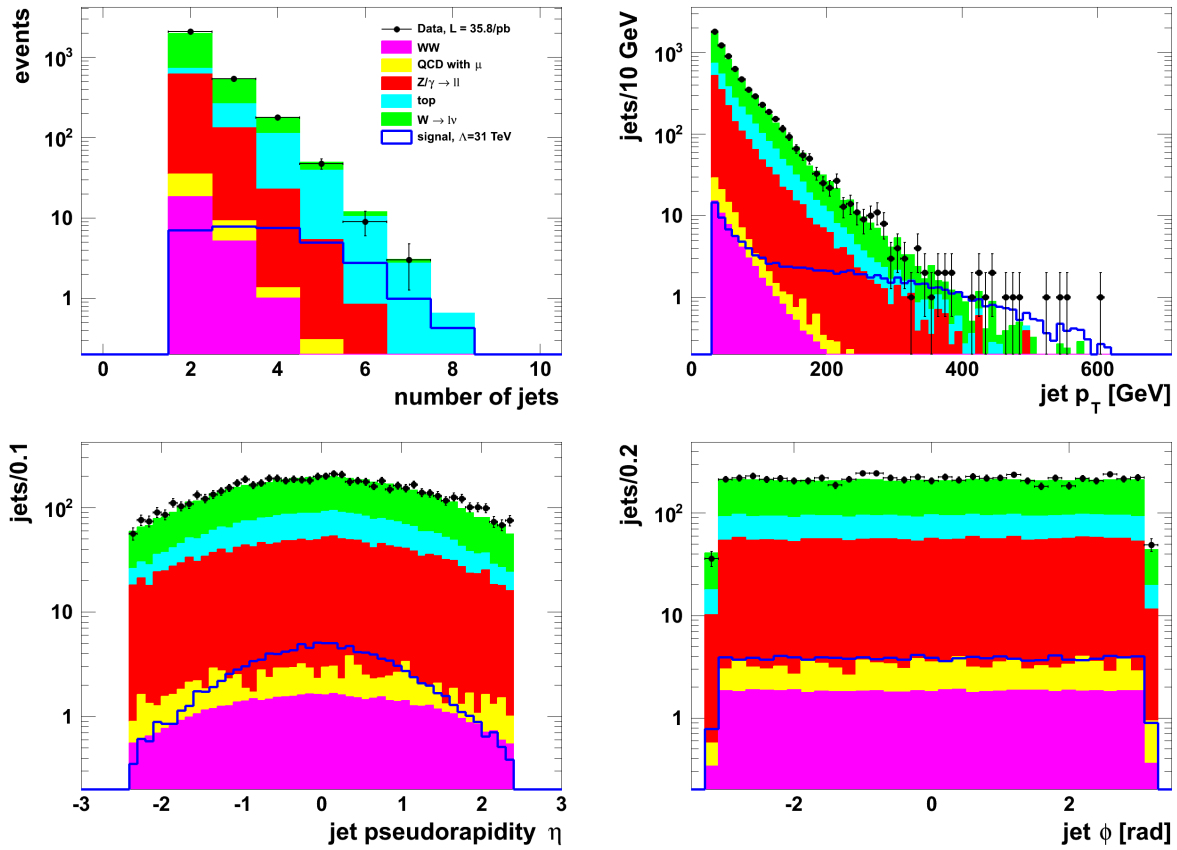

Figure 5.14: Control selection: distributions of selected jet multiplicity (top left), transverse momentum (top right), pseudorapidity (bottom left), and azimuthal angle (bottom right).

in the impact parameter distributions. For highly energetic muons, track bending is very small compared to the overall length of the track (about 7.5 m), therefore differences in the track fits lead to differences in the extrapolated starting points (i.e. impact parameters) of the tracks. The discrepancies seen in these distributions affect only a small percentage of all selected muons and are accepted as is, since the main kinematic distributions (p_T, η, and ϕ) are well described by simulations.

The estimated energy loss dE/dx of selected muons measured with the strip tracker modules is shown in Fig. 5.13. The long tail of the signal distribution contains staus with low speeds β. The data and SM simulation energy loss measurements agree well in the most probable value for minimally ionizing particles, $dE/dx \simeq 3$ MeV/cm. However, the tails in the data distribution are a bit wider than in the SM simulation. For this reason, the background at high dE/dx values, which will be required in the final selection (see

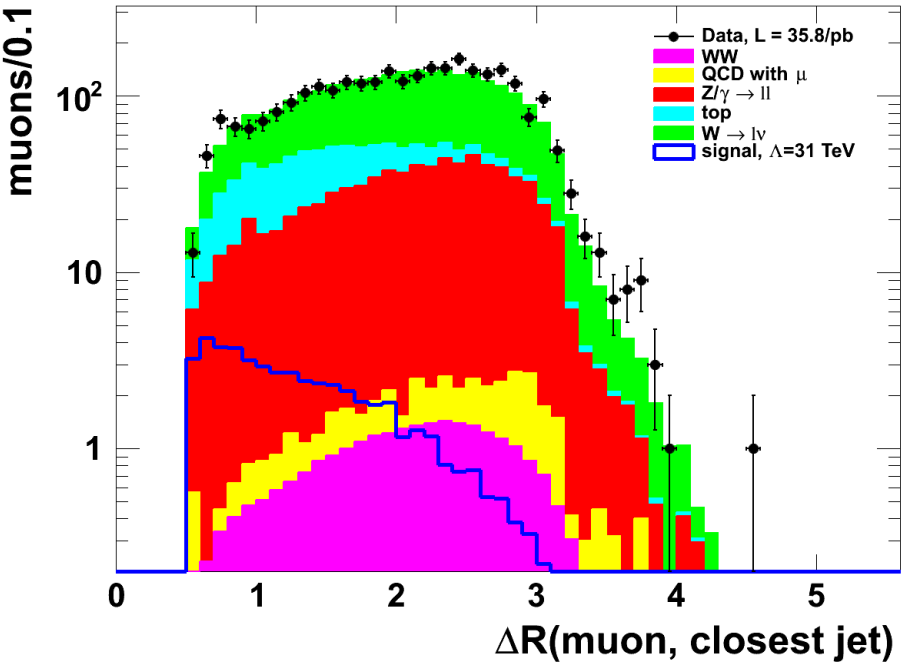

Figure 5.15: Control selection: distribution of ΔR between selected muon candidates and selected jets. A cut of $\Delta R > 0.5$ was applied.

Sec. 5.6), will be estimated with much better statistical precision from a larger dataset in the next section.

After requiring at least two jets and one selected muon, the number of selected jets and their transverse momenta are well described by simulation with respect to the data, as shown in Fig. 5.14. The high number of energetic particles expected in SUSY cascades becomes evident in the jet multiplicity distribution, which is nearly flat up to five jets with p_T greater than 30 GeV for the signal. In the Standard Model, events with five or more jets are mostly expected from top-pair production. The data distributions of η and ϕ of selected jets, shown in the bottom row of Fig. 5.14, agree with the SM simulation. As with muons, jets from signal events are more likely to be produced at lower absolute pseudorapidities than in the SM.

The angular distance between selected muons and the closest selected jet is shown in Fig. 5.15. The difference in shape between SM and signal can be explained by the high activity in signal events. For this reason, there are few signal events having large areas with little or no activity. This results in a steep decline in the ΔR distribution for the

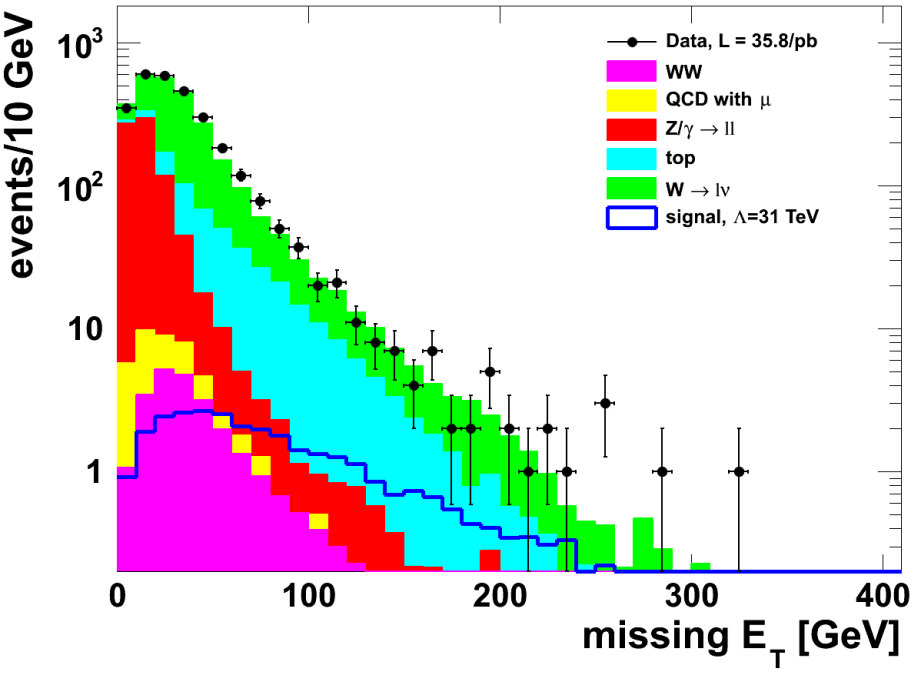

Figure 5.16: Control selection: distribution of missing transverse energy.

signal, whereas SM events have a flatter spread that falls off sharply after ΔR exceeds π.

The robustness of the selection is cross-checked with several other event variables that show the overall performance and understanding of the CMS detector. For instance, the distribution of missing transverse energy agrees well between data and SM simulation, as shown in Fig. 5.16. Similarly, the invariant mass of all opposite sign muon pairs is well described. The mass distributions are shown with and without the Z boson rejection described in Sec. 5.4.3. Only three SM backgrounds contribute to this distribution. The peak of the Z boson is nicely visible in the data and well described by the SM simulation, showing that the reconstruction of muons is well-understood. The long tail of the invariant mass distribution for the signal shows that the rejection of Z bosons does not significantly reduce the signal efficiency.

In the control selection, isolated muons produced in association with at least two hadronic jets have been extracted from proton-proton collisions measured by the CMS experiment. Selected muons are described well by the SM simulation for fundamental observables such as multiplicity and transverse momentum. Some of the detailed properties unveil small discrepancies in the reconstruction of muons, which is assumed to be caused

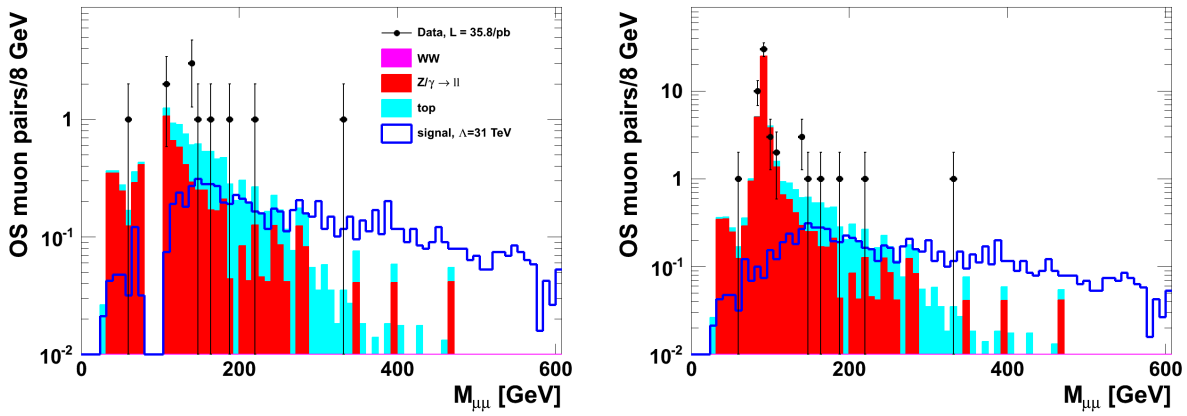

Figure 5.17: Control selection: distributions of invariant mass of opposite sign (OS) muon pairs with (left) and without (right) Z-boson rejection.

mostly by unknown misalignments in the muon chambers and their relative positions with respect to the silicon tracker. However, the further selection of events will be based on the well-described fundamental properties of muons. Furthermore, selected hadronic jets are excellently described by the simulations, both in shape and normalization. Hence, it is safe to assume that the remaining collision data sample is composed mainly of the simulated SM processes, mainly Drell-Yan production of leptons, single W production, and top-pair production. The number of events remaining in all simulated samples and the collision data after three selection steps are listed in Tab. 5.4. The first step is the trigger and vertex requirement, followed by requiring at least one selected muon, and the third step is the requirement of two or more selected jets. The trigger and vertex requirement shows a large discrepancy between expected SM events and collision data because the background samples are not exhaustive with respect to sources of muons. At low energies, a large number of muons originating from meson decays are expected to be present in the collision data. However, after selecting one high-p_T, isolated muon, the listed SM MC samples are in agreement with the data within statistical errors.

For the further suppression of the SM background, the transverse momentum and dE/dx distributions of selected muons will be investigated. The analysis will be split into events with one muon (exclusively) and events with two or more muons, respectively. This step is chosen due to the observation of vastly different signal-to-background ratios for the different muon multiplicities, as shown in Fig. 5.10. The final selections will be adjusted such that a good signal-to-background ratio is obtained for each search channel.

Data Sample	trigger & vertex	1+ sel. muon	2+ sel. jets
$W \rightarrow l\nu$	251,431	11,722	1,593.7
$WW \rightarrow X$	272	69.5	24.9
$Z/\gamma \rightarrow ll$, $10 < M_{ll} < 50$ GeV	9,509	384	78.4
$Z/\gamma \rightarrow ll$, $M_{ll} > 50$ GeV	34,199	4,806	652.6
$t\bar{t}$	1,774	372	343.5
$t \rightarrow bl\nu$	267	52.1	29.4
QCD with muons	2,641,209	107	21.0
Sum	2,938,661	17,513	2,743.7
Collision Data	7,320,998	17,644	2,860

Table 5.4: Control selection event yields for SM samples and 35.8 pb^{-1} of proton-proton collision data.

5.5 dE/dx Background Estimation from Data

As explained above, instead of using the simulated SM distribution of the energy loss measurement shown in Fig 5.13 for the final cuts, a prediction of muon tracks with high dE/dx will be calculated from collision data.

At track momenta above a few GeV, no highly ionizing tracks are expected in the Standard Model, for reasons explained in Sec. 2.6. For the investigated muon momenta, fluctuations to high dE/dx values depend solely on the number of measured tracks. Whereas the energy loss measurement is reasonably well modelled by simulations, as shown in Fig. 5.13 in the previous section, a prediction of the expected background from data, using real measurements from the silicon strip modules of the tracker, is much more trustworthy.

The strategy to predict the number of muon tracks above a certain dE/dx value is to use background-like collision tracks, apply a dE/dx cut at a desired value, and calculate the cut efficiency. The obtained dE/dx cut efficiency will be called *dE/dx fake rate*. For the final selection, the dE/dx fake rate will be used to reweight the number of expected background events obtained after the control selection. This substitutes a cut on the simulated background dE/dx distribution. In the case of the signal dE/dx distribution, a selection cut on the simulated value is applied. This is justified, because the mean and width of the dE/dx distribution is well simulated.

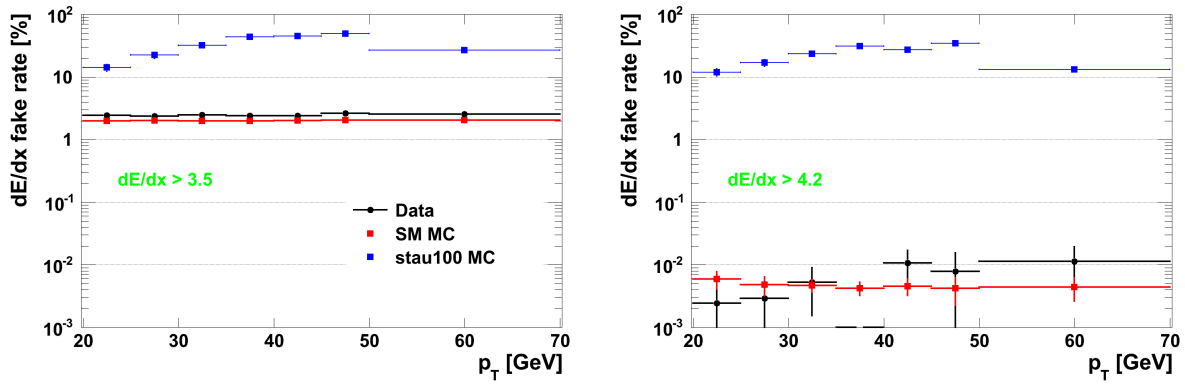

Figure 5.18: dE/dx cut efficiencies (fake rates) in bins of transverse momentum of muon tracks from data, SM, and signal simulations. The rightmost bin contains all muon tracks with $p_T >$ 50 GeV. Results for dE/dx cuts of 3.5 (left) and 4.2 MeV/cm (right) are shown. For comparison, the y-axis ranges are identical. The generated stau mass in the signal is 100 GeV.

The sample of background-like data tracks is similar to the control selection of muons detailed in Sec. 5.4.3. The selection criteria are identical except for the invariant mass requirements, which are omitted here, and the selected transverse momentum region: only muons with $20 < p_T < 50$ GeV are used for the determination of the dE/dx fake rate. No jet selection was done for this muon sample. The reason for choosing a low-momentum muon sample for the background prediction is two-fold: first, it must be ensured that the sample is not potentially contaminated by signal tracks, which have higher average dE/dx values and would therefore drive up the resulting fake rate. Secondly, in order to validate that the dE/dx fake rate for the background is indeed independent of p_T and can therefore be utilized for tracks with $p_T > 50$ GeV, a statistically independent sample must be used. Using a large sample of tracks reduces the influence of possible signal tracks in the data, but the effect of signal contamination must be investigated with simulations nonetheless.

In order to extrapolate the dE/dx fake rate from the background to the signal region, fake rates are calculated in intervals of 5 GeV of transverse momentum for the background region of 20 to 50 GeV, and, for comparison, for all tracks with $p_T > 50$ GeV (the signal region). This process is also done for simulated tracks from the main expected SM backgrounds, single W production, Drell-Yan production of lepton pairs, top-pair production, and QCD events with at least one muon, as well as for the signal with a stau mass of 100 GeV. The background samples are weighted according to their cross sections and the combined fake rate for all samples is computed.

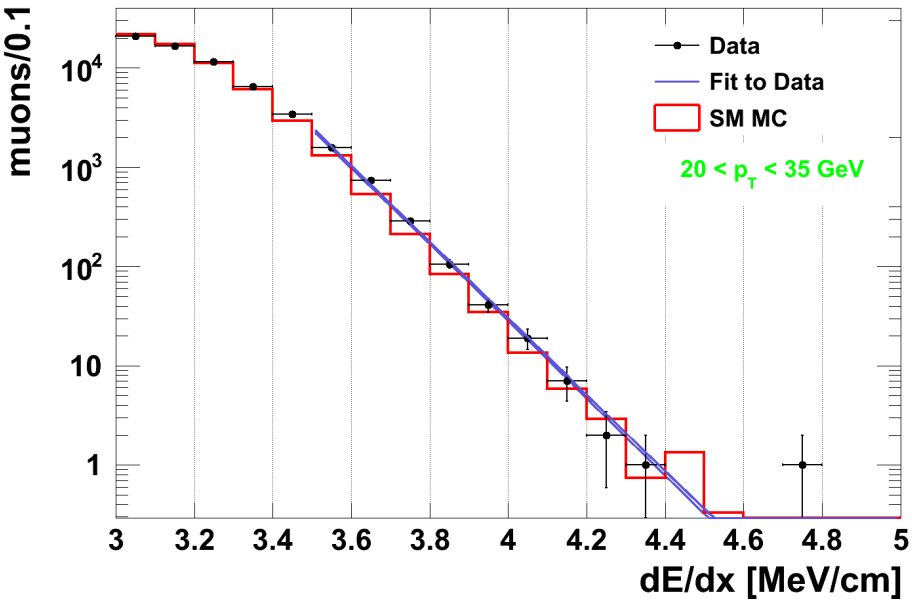

Figure 5.19: Distribution of energy loss per unit length (dE/dx) of muons with $20 < p_T < 35$ GeV for data and SM MC. An exponential function, $y = C \cdot e^{-S \cdot x}$, was fit to the data from 3.5 to 5.0 MeV/cm. (See text for more details.)

Fake rates are calculated for cuts on dE/dx ranging from 3.4 to 4.3 MeV/cm, in steps of 0.1 MeV/cm. Resulting values for data, SM background, and the signal simulation are shown in Fig. 5.18 for two of the dE/dx cut values. The plot for $dE/dx > 3.5$ MeV/cm shows that the fake rate does not depend on the p_T of the muon track for data and SM simulation as expected from the high momentum plateau of the Bethe-Bloch formula (see Sec. 2.6). For the cut of $dE/dx > 4.2$ MeV/cm, the data and SM MC distributions are less constrained due to the smaller statistics. For this cut, another method of calculating the fake rate, explained in the next paragraph, is used. In the signal simulation, the dE/dx cut efficiency increases with p_T, which reflects the turn-on of the trigger efficiency shown in Fig. 5.3, as well as the bare signal p_T distribution, which peaks around 100 GeV (see Fig. 5.2). In the signal region of $p_T > 50$ GeV, the signal efficiency decreases again since all high-momentum (i.e. low dE/dx) stau tracks enter this bin.

At high dE/dx cut values (4.1 to 4.3 MeV/cm), the number of muon tracks decreases rapidly, making statistical fluctuations very likely. For these cut values, the observed exponential decrease of the dE/dx distribution at high dE/dx is modelled with a function

of the form

$$y(x) = C \cdot e^{-S \cdot x}, \tag{5.2}$$

where C and S are free parameters, y is the number of tracks, and x is the muon track dE/dx. The function in Eq. 5.2 is fitted to a dE/dx distribution of tracks in a p_T-range corresponding to the values given in Tab. 5.5. The fit is applied in the range from 3.5 to 5.0 MeV/cm to stay in the regime of the exponential behavior. At lower values, the dE/dx distribution flattens until the maximum at about 3 MeV/cm is reached. Then, for dE/dx cut values of 4.1 and above, the curve is integrated from the cut value to infinity to approximate the number of tracks passing the cut:

$$\int_{dE/dx \text{ cut}}^{\infty} y(x)\, dx = \frac{C}{S} \cdot e^{-S \cdot dE/dx \text{ cut}}. \tag{5.3}$$

This method is used to calculate the fake rate for the three highest dE/dx cut values. For the cuts of 4.0 MeV/cm and below, the counting of tracks gives a nearly identical result to the exponential fit procedure. The resulting fit for muon tracks with $20 < p_T < 35$ GeV is shown in Fig. 5.19. This p_T-range is used for the dE/dx cut of 4.2 MeV/cm due to increasing signal contamination at higher momenta. The sum of SM backgrounds is shown for comparison. The free parameters of the exponential fit function, Eq. 5.2, are: $C = 7.6 \pm 2.3 \cdot 10^{16}$, $S = 8.87 \pm 0.09$ cm/MeV, $\chi^2/n_{dof} = 10.5/8$.

The statistical error of the fake rate is estimated from the fit errors on the free parameters, C and S, of the exponential fit. Varying these parameters by their errors and then recalculating the number of tracks with the integral Eq. 5.3 gives a higher and a lower fake rate. The deviations from the central values are given as (asymmetric) errors in Tab. 5.5.

Since the exact composition of the collision data sample is not known, the effect of possible signal contamination of the fake rate must be taken into account. Even at low transverse momenta, signal tracks may be present in the data, leading to an increase of the fake rate which in turn causes an over-estimation of the expected background after cutting on dE/dx. Comparing the SM MC fake rate with a fake rate where signal tracks are added - with the correct weight according to the luminosity of 35.8 pb^{-1} - to the SM simulation gives a measure of the signal influence. This is shown in Fig. 5.20 for the signal sample with a stau having a mass of 100 GeV. Of course, for higher stau masses the contamination decreases in proportion to the cross section. All intervals in the range of $20 < p_T < 50$ GeV for which the signal-contaminated fake rate lies within one standard deviation of the SM-only fake rate are considered for the determination of the data-driven fake rate. For the

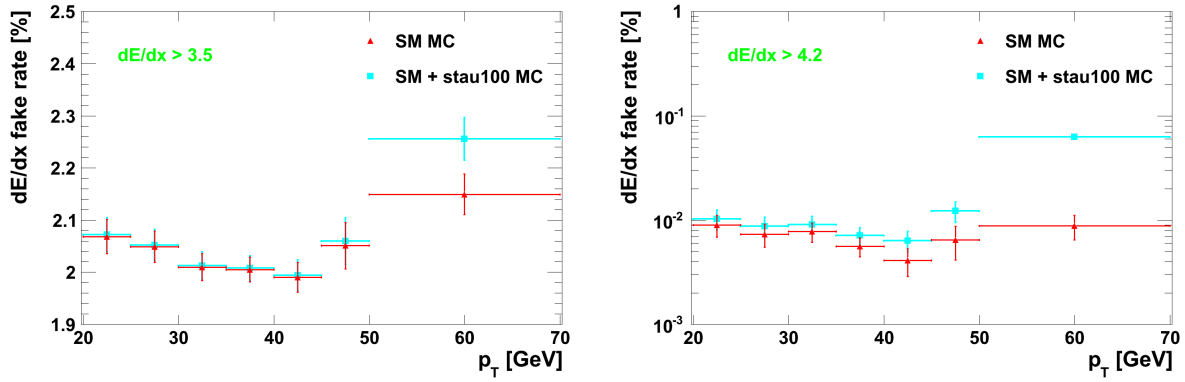

Figure 5.20: Simulated dE/dx fake rates are shown as a function of transverse momentum of simulated muon tracks. Background (SM) is compared to the sum of signal and background to visualize the effect of possible signal contamination. The rightmost bin contains all muon tracks with $p_T > 50$ GeV. Results for dE/dx cuts of 3.5 (left) and 4.2 MeV/cm (right) are shown. The generated stau mass in the signal is 100 GeV.

dE/dx cut of 3.5 MeV/cm, the effect of added signal is very small ($< 1\,\%$) except for tracks with $p_T > 50$ GeV. For this cut, the whole range of tracks with $p_T < 50$ GeV is used for the determination of the fake rate. In contrast, a strong signal contamination is evident for the dE/dx cut of 4.2 MeV/cm. In the p_T intervals from 35 to 50 GeV, the fake rates with added signal tracks deviate by more than one sigma from the background-only fake rates. Therefore, collision data tracks with $20 < p_T < 35$ GeV are used in the fake rate calculation (in this case with the exponential fit).

Calculated data-driven dE/dx fake rates and the corresponding transverse momentum ranges used for the calculation are listed in Tab. 5.5. Additionally, the signal MC efficiencies for the corresponding dE/dx cuts are given for muon tracks with $p_T > 50$ GeV. The signal efficiency ϵ_S is the value of the highest p_T bin in the signal distributions shown in Fig. 5.18. Also, the ratio of the signal efficiency and the background fake rate (ϵ_S/f_B) is given for each cut. As expected, the value of ϵ_S/f_B increases exponentially as the cut value increases, since the signal tail of the dE/dx distribution falls off much slower than the exponentially decreasing background. Systematic errors on this method and a correction for signal contamination are discussed below.

dE/dx cut [MeV/cm]	Background fake rate f_B [%]	Fit range in p_T [GeV]	Signal efficiency ϵ_S [%] ($p_T > 50$ GeV)	ϵ_S/f_B
3.4	5.485 ± 0.051	20 - 50	23.8	4.3
3.5	2.441 ± 0.035	20 - 50	20.0	8.1
3.6	1.054 ± 0.023	20 - 50	17.2	16
3.7	0.419 ± 0.014	20 - 50	15.2	36
3.8	0.167 ± 0.009	20 - 50	13.6	81
3.9	0.067 ± 0.006	20 - 50	12.1	181
4.0	0.031 ± 0.004	20 - 50	11.0	355
4.1	0.013 ± 0.001	20 - 45	10.0	786
4.2	$0.0050^{+0.0001}_{-0.0004}$	20 - 35	9.1	1820
4.3	$0.0022^{+0.0001}_{-0.0002}$	20 - 35	8.4	4200

Table 5.5: Data-driven dE/dx fake rates f_B for given dE/dx cut values. Muon tracks with transverse momenta in the ranges given in the third column were used for the fits. Also listed are the corresponding dE/dx cut efficiencies ϵ_S for the signal with the stau mass of 100 GeV, and the ratio ϵ_S/f_B.

Systematic Errors and Signal Contamination Correction

The data-driven dE/dx fake rate in the signal region of muons with $p_T > 50$ GeV is compared to the background fake rate in order to test the dependence of the dE/dx measurement on the transverse momentum of tracks. Additionally, the signal contamination is evaluated for the two chosen dE/dx cut values.

For the cut of 3.5 MeV/cm, the relative statistical error on the fake rate in data is less than 2 % ($f_{3.5} = 2.441 \pm 0.035\,\%$). The signal-region fake rate, being the value of the rightmost bin in the left plot of Fig. 5.18, is $f_{3.5}^{p_T>50} = 2.542 \pm 0.120$ %, which agrees with the background value $f_{3.5}$. As systematic uncertainty, the relative difference between the two fake rates is taken, 4.1 %. As shown in the left plot of Fig. 5.20, the signal contamination for the dE/dx cut of 3.5 MeV/cm is less than 1 % in the background region of $20 < p_T < 50$ GeV. Together, the systematic uncertainty on the dE/dx fake rate for the cut of 3.5 MeV/cm is estimated to be $\delta(f_{3.5}) = 5\,\%$.

For the cut of 4.2 MeV/cm, the exponential fit procedure on the background-like data sample (see Fig. 5.19) is repeated for the selection region of muons with $p_T > 50$ GeV.

dE/dx cut [MeV/cm]	Corrected background fake rate f_B^c [%]	Systematic error $\delta(f_B^c)$ [%]
3.5	2.441 ± 0.035	5
4.2	$0.0041^{+0.0001}_{-0.0003}$	24

Table 5.6: Data-driven dE/dx fake rates corrected for signal contamination (with statistical errors) and systematic uncertainties for dE/dx cut values chosen for the final selection.

The results of the integration of the exponential above 4.2 MeV/cm are then compared. The background fit resulted in a fake rate of $4.97 \cdot 10^{-3}$ %, see Tab. 5.5. Using muons with $p_T > 50$ GeV results in a fake rate of $5.23 \cdot 10^{-3}$ %. The relative difference of these two results is 5 %.

At this dE/dx cut value, the low number of surviving background tracks leads to signal contamination down to the lowest values of p_T, as shown in the right plot of Fig. 5.20. The average increase of the fake rate due to signal tracks in the range $20 < p_T < 35$ GeV (which was used to calculate the fake rate from data) is 18 %. Should the signal with $M_{stau} = 100$ GeV be present, then the background fake rate would be overestimated by 18 %[3]. In the case of an excess in the data, this overestimation would lead to a worsening of the signal significance because of the increased background prediction. If no excess were observed, reducing the background by 18 % while having the same number of observed data events would lead to degraded limits. However, this is a conservative approach and therefore the dE/dx background fake rate for the cut of 4.2 MeV/cm is reduced by 18 %, resulting in a final value of $f_{4.2}^c = 0.0050\,\% \cdot 0.82 = 0.0041\,\%$. Additionally, the correction factor of 18 % is taken as a systematic uncertainty since it is a priori unknown whether or not signal is present in the data.

The two uncertainties of 5 % and 18 % are added linearly to give a systematic error of 23 %. Finally, the larger of the asymmetric statistical errors from Tab. 5.5 (amounting to 8 %) is added in quadrature to the aforementioned 23 % systematic error to obtain the total systematic error for the dE/dx fake rate, $\delta(f_{4.2}^c) = 24\,\%$.

Corrected dE/dx background fake rates used in the final selection, which is described in the following section, and the corresponding systematic uncertainties are listed in Tab. 5.6.

[3]This depends on the GMSB mass scale: for higher masses, lower cross sections lead to smaller signal contaminations. To be conservative, the value for the lowest mass scale is taken.

5.6 Final Selection

As alluded to in Sec. 5.4.5, the final analysis will be split according to the muon multiplicity of events remaining after the control selection. For the determination of the final cuts to increase the signal-to-background ratio, just the signal and background MC distributions are compared to avoid a bias from the observed data distributions.

To begin, let us consider again the muon multiplicity distribution from the control selection, shown in Fig. 5.10: in the Standard Model, events with one muon are predicted to come mostly from single W production with a smaller contribution from Drell-Yan di-lepton processes, where one muon was either not energetic enough to survive the cut of $p_T > 50$ GeV, misreconstructed, or coming from a di-tau event where at least one tau decayed into a muon, with the latter two scenarios being much less likely than the former. Events with two selected muons are strongly suppressed with respect to single-muon events in the SM, reflecting the steep decline of the transverse momentum distribution, and are almost evenly divided between top-pair production and Drell-Yan production. No three-muon SM events pass the control selection. In contrast, the signal contains about as many multi-muon events as single-muon events. As a consequence, the signal-to-background ratio differs greatly between the single- and multi-muon channels, and the two channels will be investigated separately. The number of selected events for the two channels after the control selection are summarized in Tab. 5.7.

Muon	Remaining events			
multiplicity	Data	SM MC	Stau M=100	S/B
1 μ	2849	2731.7	16.1	0.006
2+ μ	11	12.0	15.6	1.3

Table 5.7: Number of observed and expected events and expected signal-to-background ratio for single-muon and multi-muon events after the control selection. Event numbers correspond to 35.8 pb^{-1} of CMS data.

5.6.1 Single-muon Channel

After the control selection, $B = 2731.7$ single-muon events are selected from the sum of all SM backgrounds, whereas $S = 16.1$ events are expected from the GMSB signal with a

stau mass of 100 GeV, corresponding to a signal-to-background ratio of $S/B = 0.006$. Figure 5.21 shows the energy loss of selected muons as a function of their transverse momentum after the control selection. The signal distribution clearly shows that highly ionizing tracks are expected at the lower end of the p_T spectrum. The background distribution is centered around the expected mean energy loss of 3 MeV/cm for MIPs. Clearly, a cut on the energy loss variable will result in a drastic improvement of the signal-to-background ratio.[4] For clarification, the one-dimensional muon p_T distribution is also displayed in Fig. 5.21. Although the p_T spectrum of the signal is harder than that of the background, the tail from SM muons almost completely covers the signal distribution. Therefore, it is not efficient to cut on transverse momentum in the single-muon channel to discriminate signal-like events from the background. The full selection criteria for this channel are listed in Tab. 5.8.

The cut on the dE/dx variable of selected muons is chosen such that a good S/B is obtained while keeping the signal efficiency high. As shown in the previous section, the cut of 4.2 MeV/cm improves S/B by about a factor of 1,820. This cut is applied on the signal and collision data dE/dx distributions, whereas the number of expected background events is calculated by multiplying the data-driven dE/dx fake rate with the number of single-muon events expected after the control selection. The signal efficiency for the range of dE/dx cuts from Tab. 5.5 is shown as a function of the resulting purity in Fig. 5.22. The signal purity is defined as $p = S/(S + B)$, which is the relative amount of signal (S) events with respect to all events selected.

For the dE/dx cut of 4.2 MeV/cm, the background fake rate is estimated from data to be $f^c_{4.2} = 0.0041\,\%$, see Tab. 5.6. The predicted number of remaining background

[4]Note that the background dE/dx values are just shown to gain an understanding of what to expect roughly from the SM. As explained in the previous section, the data-driven dE/dx fake rate will be used to reweight background events and to obtain the number of expected events from the SM.

Control selection	Additional criteria
1+ **good primary vertex**	none
1 **selected muon**	$dE/dx > 4.2$ MeV/cm
2+ **selected jets**	none

Table 5.8: Single-muon final selection criteria. The selection of physics objects is detailed in Tab. 5.3.

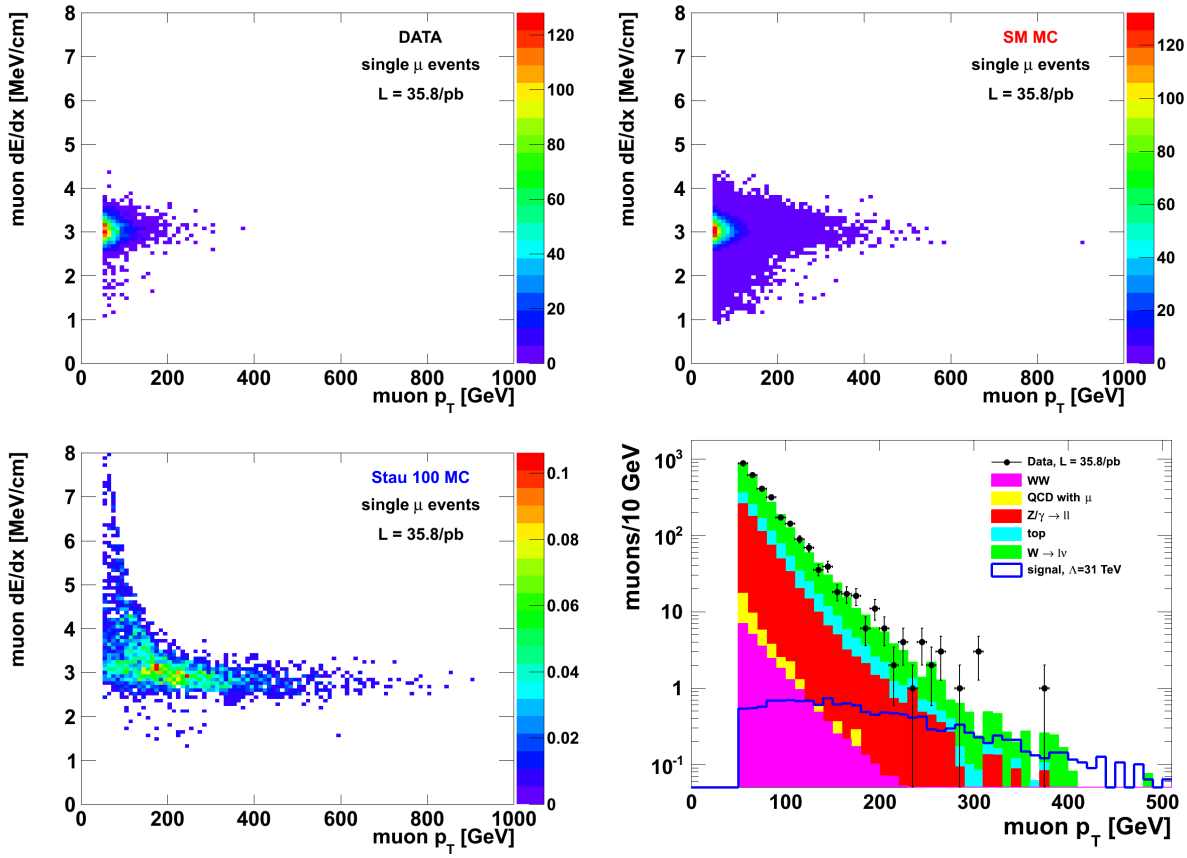

Figure 5.21: Control selection for single-muon events: muon dE/dx versus transverse momentum distribution for data (top left), combined SM background (top right), and signal (bottom left) are shown. (Note the different z-axis scales.) The muon p_T distribution for all samples is shown in the bottom right plot.

events after this cut is $B = 0.112$. After applying the dE/dx cut on signal and data, one event remains in the data sample, while $S = 1.47$ events are expected in the signal. The final signal-to-background ratio for this channel is $S/B = 13.1$. The corresponding dE/dx distributions are shown in Fig. 5.23, where the background prediction is shown as a histogram following the exponential fit curve from Fig. 5.19.

Distributions of muon p_T, number of jets, jet p_T, and missing transverse energy are shown in Fig. 5.24. Because of the high dE/dx cut, the muon p_T spectrum of the signal is cut off at about 150 GeV. The average number of jets is much larger in the signal than in the background, as are the average jet p_T and missing transverse energy. Due to the long tails of the signal distributions, a better separation of signal and background can be

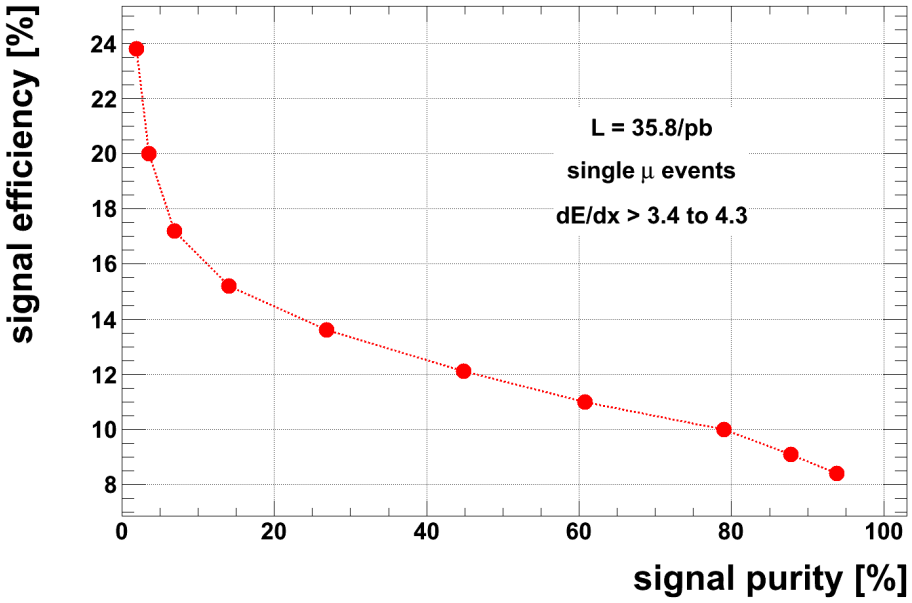

Figure 5.22: Signal efficiency versus purity for events with one selected muon for a range of muon track dE/dx cuts from 3.4 to 4.3 MeV/cm. Values are calculated with respect to the single-muon control selection. The generated stau mass is 100 GeV.

expected with larger data samples collected in 2011 and beyond.

The one selected data event, which is statistically compatible with the background expectation of 0.112 and the signal expectation of 1.47 events, is situated at the lower end of the distributions in Figs. 5.5 and 5.24. The momentum of the selected muon is $p = 69$ GeV and its energy loss is 4.4 MeV/cm. Using Eq. 2.26, the mass of this stau candidate is 70 GeV, which is below the limit from LEP of about 97.5 GeV for long-lived staus [19].

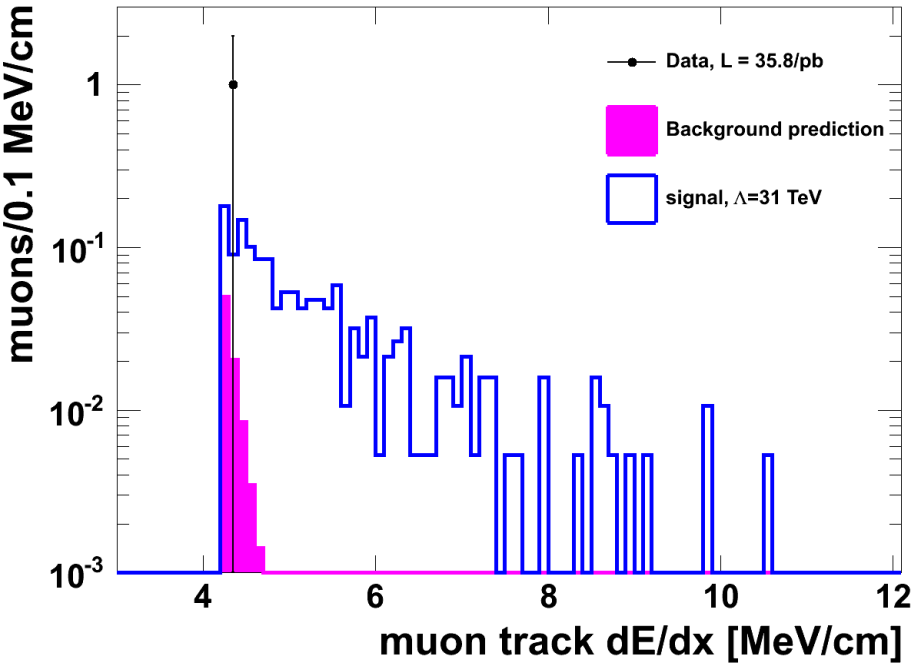

Figure 5.23: Single-muon final selection: distribution of inner track energy loss per unit length (dE/dx) of muons after a cut of $dE/dx > 4.2$ MeV/cm. The background prediction was estimated from data in Sec. 5.5.

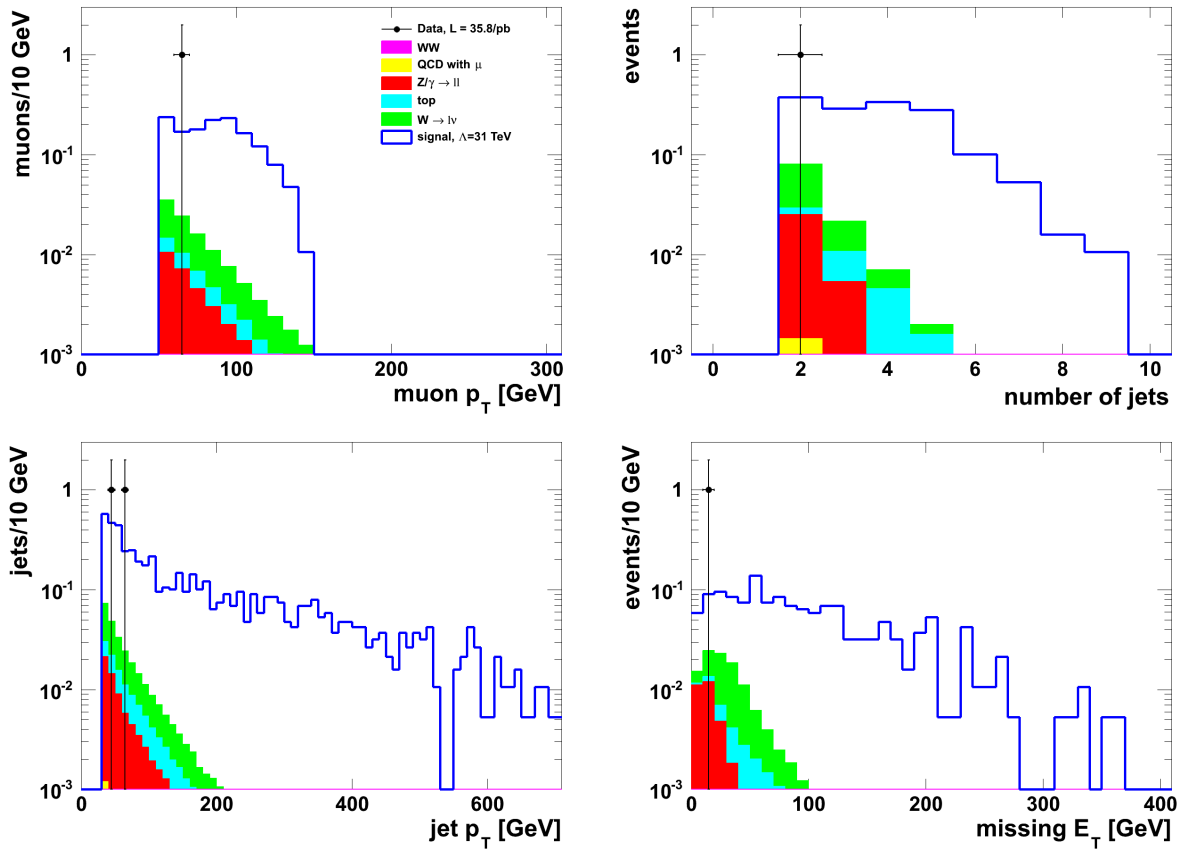

Figure 5.24: Single-muon final selection: distributions of muon p_T (top left), number of jets (top right), jet p_T (bottom left), and missing transverse energy (bottom right) are shown. The SM backgrounds have been reweighted for the dE/dx cut of 4.2 MeV/cm (see Sec. 5.5).

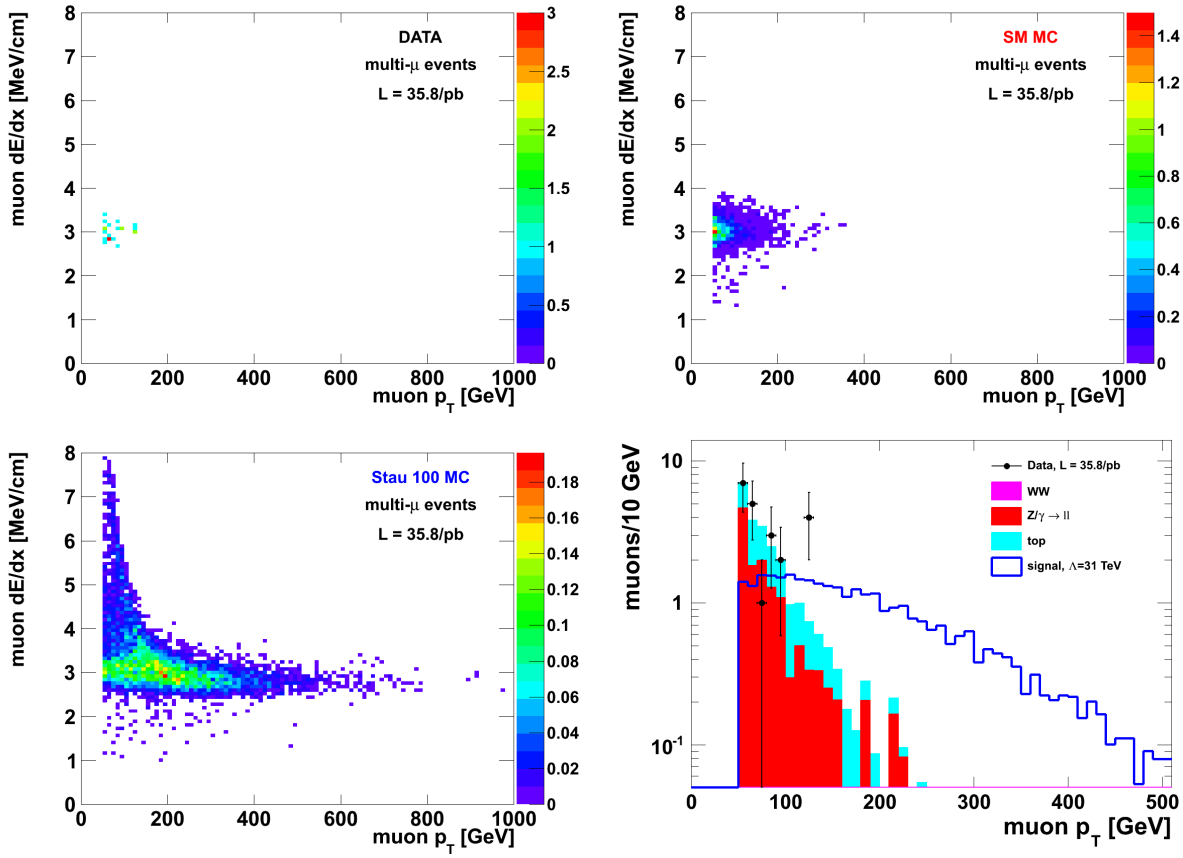

Figure 5.25: Control selection for events with two or more muons: muon dE/dx versus transverse momentum distributions are shown for data (top left), combined SM background (top right), and signal (bottom left). (Note the different z-axis scales.) The muon p_T distribution for all samples is shown in the bottom right plot.

5.6.2 Multi-muon Channel

Events with two or more selected muons are analysed in this section. Eleven such data events are measured, while $B = 12.0$ are predicted from Standard Model simulations, and $S = 15.6$ are expected from the signal, corresponding to $S/B = 1.3$. The correlation of energy loss and transverse momentum of muons for this channel after the control selection is shown in Fig. 5.25. The signal distribution resembles that of the single-muon channel (see Fig. 5.21), while the background is very diminished. The reduced background event yield strongly affects the tails of both the dE/dx and the p_T distributions. Thus, a looser cut on dE/dx than the one used for the single-muon channel is feasible, enhancing the

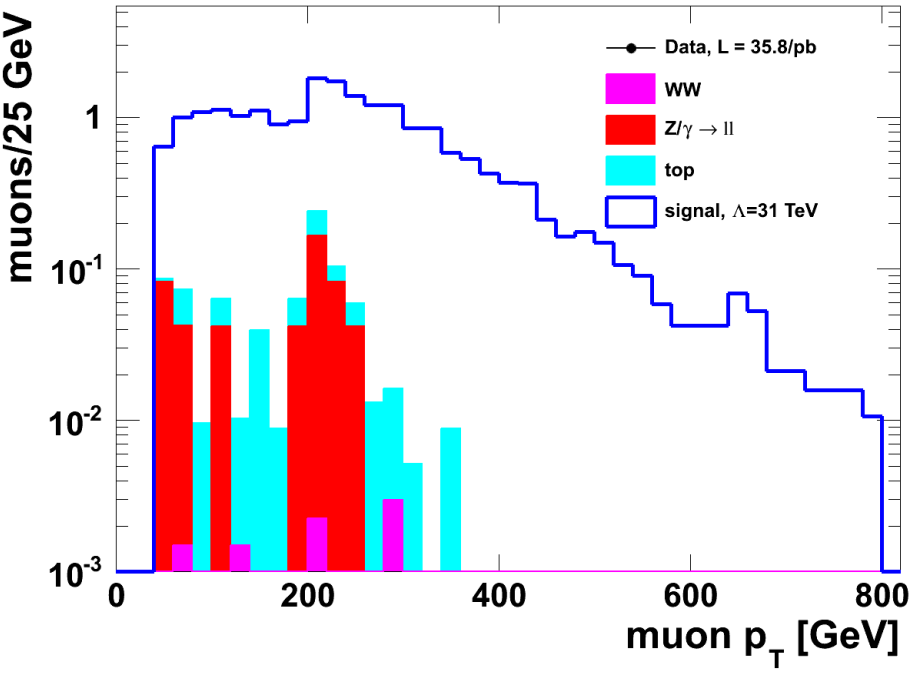

Figure 5.26: Multi-muon p_T final selection: selected muon transverse momentum distribution. The *leading muon* is required to have $p_T > 200$ GeV. Zero data events pass this selection.

signal efficiency. Furthermore, a cut on p_T will be made for the multi-muon channel, since the signal tail is much higher than the background, which can be seen in the bottom right plot of Fig. 5.25.

In the following, the selections on dE/dx and p_T will be made separately for the multi-muon channel.

Multi-muon p_T-Channel

For the determination of a cut on transverse momentum, the p_T spectrum of the multi-muon channel from Fig. 5.25 is regarded in more detail: in the SM, top-pair production and Drell-Yan production of lepton pairs are the processes expected to produce most pairs of energetic, isolated muons. The contribution from W-boson pair production is negligible for the amount of data collected. The data are described well by the SM simulation, except for two bins which fluctuate up and down by about two standard deviations, respectively. The signal p_T spectrum peaks around 100 GeV and has a long tail. The two stable staus in a signal event often have differing momenta (and therefore also differing energy losses)

Control selection	Additional criteria
1+ **good primary vertex**	none
2+ **selected muons**	1+ **muon with** $p_T > 200$ **GeV**
2+ **selected jets**	none

Table 5.9: Multi-muon p_T final selection criteria. The selection of physics objects is detailed in Tab. 5.3.

beacuse the decay chains of the two cascades are independent from each other. A cut of $p_T > 200$ GeV removes most of the background, but also a large portion of the signal. However, requiring $p_T > 200$ GeV only from the *leading* muon greatly increases the signal yield while still removing almost all background events. The selection criteria of this channel are listed in Tab. 5.9. The resulting distributions of muon p_T in Fig. 5.26 show a threshold at 200 GeV. The number of events passing this selection is $B = 0.40$ for the background and $S = 9.64$ for the signal simulation, giving $S/B = 24.1$, while zero data events remain.

Further distributions are displayed in Fig. 5.27: the number of selected muons is always two for the background, whereas the signal contains some higher multiplicities. Much larger multiplicities are also expected in the signal for the number of jets. The jet p_T and missing transverse energy distributions have long tails in the signal, as expected in supersymmetric processes.

Multi-muon dE/dx-Channel

The selection based on high energy loss is made by going back to the control selection, i.e. without applying the leading muon p_T cut from the previous selection. Starting from the multi-muon channel signal-to-background ratio of $S/B = 1.3$, the dE/dx cut of 3.5 MeV/cm from Tab. 5.5 is chosen to obtain the number of expected background events and applied to the signal simulation to get the signal efficiency. For the same reason given for the high p_T selection, the dE/dx criterion will be required for only one muon in the multi-muon channel. However, in order to prevent the same events to be selected by the dE/dx and the p_T selections, an upper cut on the transverse muon momentum of $p_T < 200$ GeV is imposed on *all* muons in this channel. This way, events containing both a high-dE/dx and a high-p_T muon are assigned to the p_T selection described above. Thus, two

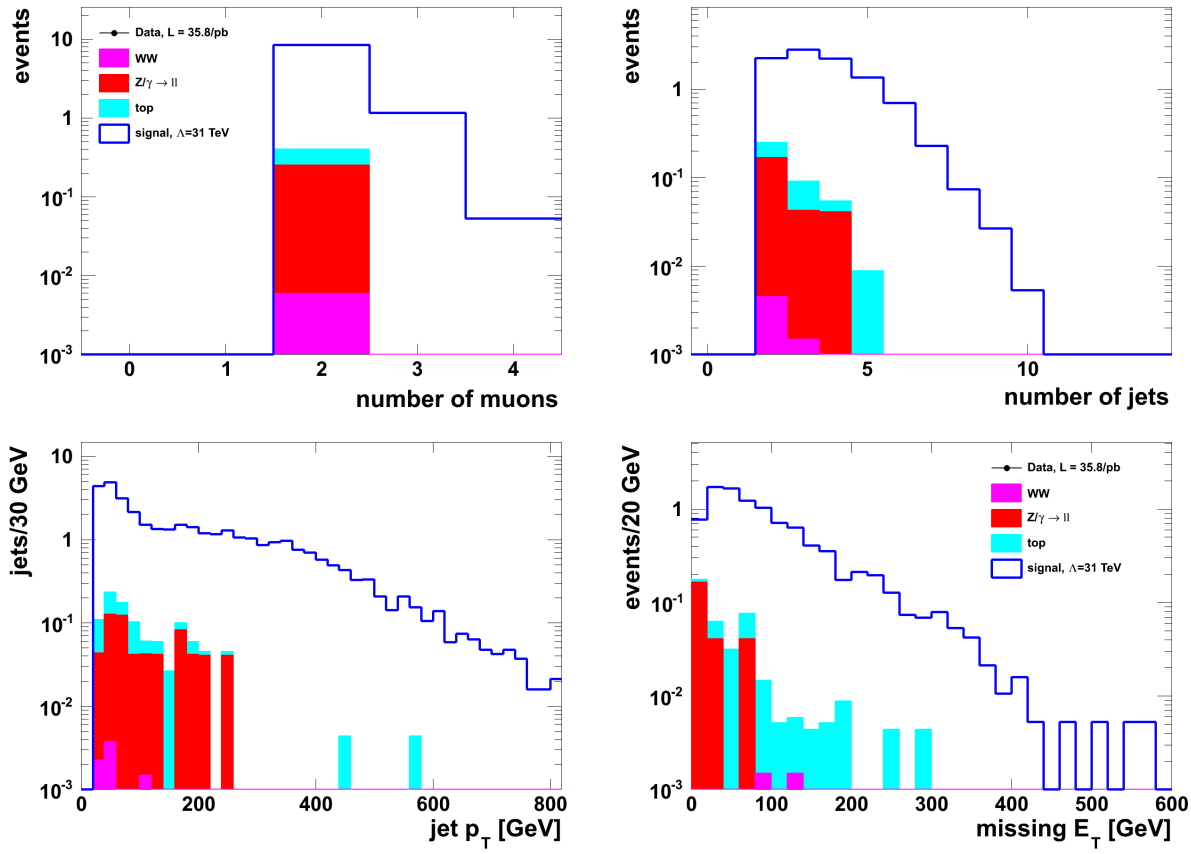

Figure 5.27: Multi-muon p_T final selection: distribtions of selected muons (top left), number of jets (top right), jet p_T (bottom left), and missing transverse energy (bottom right) are shown. The *leading muon* is required to have $p_T > 200$ GeV. Zero data events pass this selection.

disjoint multi-muon selections are performed, one exploiting the high momentum spectrum, the other using the energy loss measurement. The number of expected background events with two or more selected muons which have $p_T < 200$ GeV is $12.0 - 0.40 = 11.6$. The complete selection criteria are listed in Tab. 5.10.

In order to apply the background dE/dx fake rates, which were calculated *per muon*, the values given in Tab. 5.5 have to be recalculated for two-muon events. For a selection cut on a quantity that has a known efficiency ϵ *per particle*, a two-particle event can have three different configurations with respect to this selection cut: (1) both particles pass the cut with a probability $p_1 = \epsilon \cdot \epsilon$; (2) the first particle passes the cut but the second does not, with a probability $p_2 = \epsilon(1-\epsilon)$; (3) the reversal of (2), with probability $p_3 = (1-\epsilon)\epsilon = p_2$. Since we allow any event where only one particle (i.e. muon) passes the selection cut, all

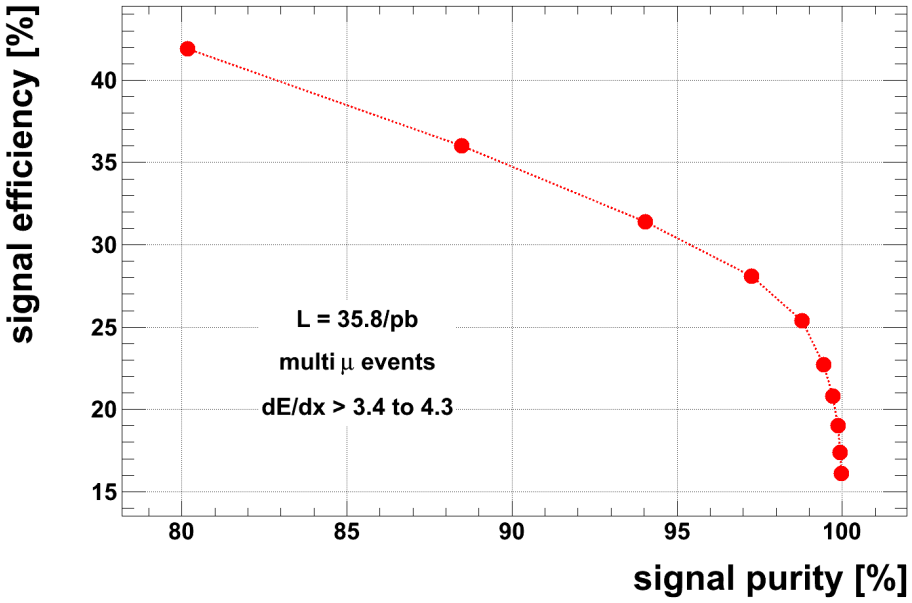

Figure 5.28: Signal efficiency versus purity for events with two or more selected muons with varying dE/dx cuts required for at least one muon. Values are calculated with respect to the multi-muon control selection. The generated stau mass is 100 GeV.

three configurations are allowed and the total probability of a two-particle event passing the selection cut is the sum of the three probabilities, $p_{total} = p_1 + p_2 + p_3 = 2\epsilon - \epsilon^2$, where ϵ is the background dE/dx fake rate *per muon* determined in the previous section. Note that, for the case at hand, it is not necessary to calculate a three-particle probability, because there are no events with three or more selected muons in the SM background simulation. Also, if ϵ is small (below 0.1=10 %), as is the case for the dE/dx fake rates, $p_{total} = 2\epsilon$ is a good approximation.

Control selection	Additional criteria
1+ **good primary vertex**	none
2+ **selected muons**	$p_T < 200$ **GeV**
	1+ **muon with** $dE/dx > 3.5$ **MeV/cm**
2+ **selected jets**	none

Table 5.10: Multi-muon dE/dx final selection criteria. The selection of physics objects is detailed in Tab. 5.3.

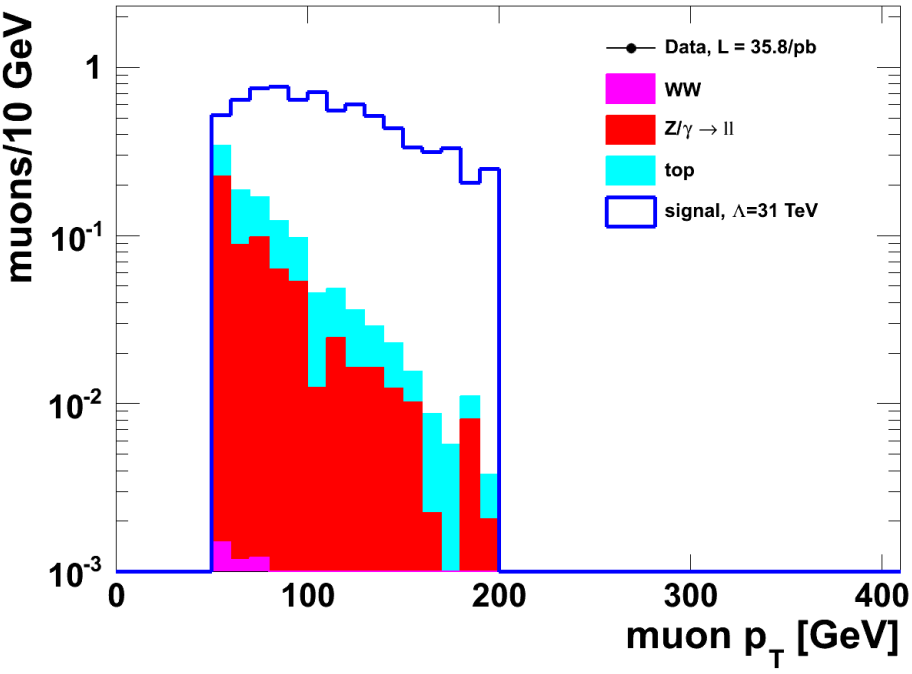

Figure 5.29: Multi-muon dE/dx final selection: selected muon transverse momentum distribution. At least *one muon* was required to have $dE/dx > 3.5$ MeV/cm. The SM backgrounds have been reweighted for this dE/dx cut (see Sec. 5.5). *All muons* were required to have $p_T < 200$ GeV.

Analogous to Fig. 5.22, the signal efficiency for the range of dE/dx cuts defined in Tab. 5.5 is displayed as a function of the purity for multi-muon events in Fig. 5.28. Since the initial signal-to-background ratio in the multi-muon channel is much larger than in the single-muon channel, a lower dE/dx cut is chosen to keep the signal efficiency as high as possible. For the cut of 3.5 MeV/cm, zero data events, $B = 0.57$ background events, and $S = 3.55$ signal events remain. This corresponds to a signal-to-background ratio of $S/B = 6.2$.

The distribution of muon p_T after the selection is shown in Fig. 5.29. The transverse momentum distributions are cut off at 200 GeV to avoid an overlap with the multi-muon p_T final selection. The same plots as shown for the other final selections are displayed in Fig. 5.30. They resemble the distributions from the multi-muon p_T final selection discussed previously (see Fig. 5.27). The SM distributions are the control distributions for multi-muon events that were reweighted for this dE/dx cut.

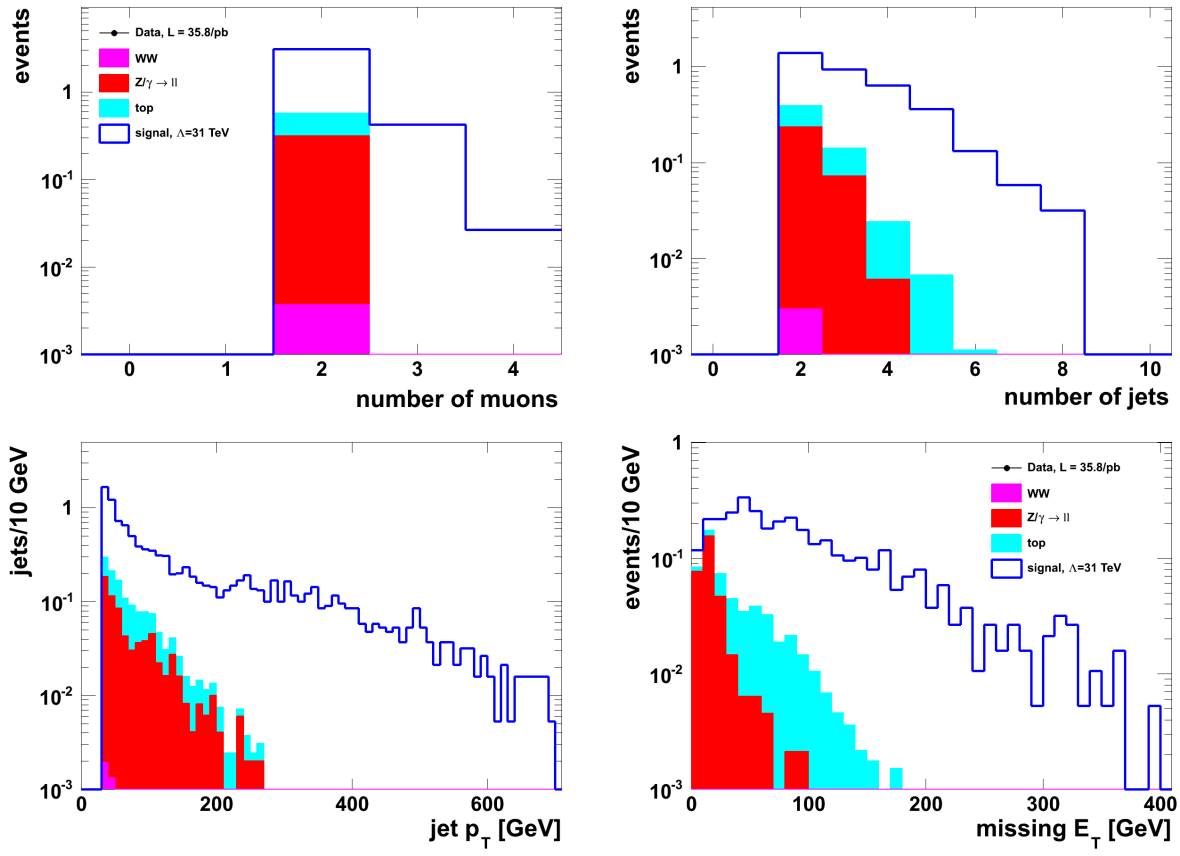

Figure 5.30: Multi-muon dE/dx final selection: distributions of selected muons (top left), number of jets (top right), jet p_T (bottom left), and missing transverse energy (bottom right) are shown. At least *one muon* was required to have $dE/dx > 3.5$ MeV/cm. The SM backgrounds have been reweighted for this dE/dx cut (see Sec. 5.5). *All muons* were required to have $p_T < 200$ GeV. Zero data events pass this selection.

			Stau M=100		Stau M=126		Stau M=156	
Final selection	Data	SM MC	events	S/B	events	S/B	events	S/B
1 μ, $dE/dx > 4.2$	1	0.11	1.47	13.1	0.60	5.4	0.21	1.9
2+ μ, $dE/dx > 3.5$	0	0.57	3.55	6.2	1.09	1.9	0.40	0.7
2+ μ, $p_T > 200$	0	0.40	9.64	24.1	2.34	5.9	0.61	1.5
Total combined	1	1.08	14.67	13.6	4.04	3.7	1.23	1.14

Table 5.11: Number of observed and expected events and expected signal-to-background ratio for the three final selections. The summation of the three selections gives the "Total combined" event numbers given in the lower row.

5.6.3 Discussion of Results

The results from the single-muon selection and the two multi-muon selections - one requiring high energy loss, the other high transverse momentum - are summarized in Tab. 5.11. In addition to the signal point with a stau mass of 100 GeV, for which the analysis was optimized, the next two higher masses given in Tab. 5.1 were analyzed and the resulting event yields are also listed in Tab. 5.11. Signal-to-background ratios are given for each selection and signal point.

No excess is seen in the data with respect to the expected Standard Model events. The multi-muon channels have larger numbers of expected signal events and no observed data events. Along with the small numbers of expected background events, exclusion limits can be set. The high signal-to-background ratios of the GMSB model with $M_{stau} = 100$ GeV point to an exclusion of this parameter point, which will be described in Cha. 7. Therefore, the candidate event from the single-muon selection is probably a fluctuation in the dE/dx measurement.

The sharp drop in cross section for higher sparticle masses, listed in Tab. 5.1, results in a signal-to-background ratio of just above one for the sample with $M_{stau} = 156$ GeV, meaning that this parameter point can not be excluded with the available data.

Finally, the signal efficiencies for the total combined selection are given in Tab 5.12 for four parameter points. The signal efficiency rises from 25 % to almost 38 % for the stau mass point of 200 GeV, due to a higher fraction of slow staus with increasing mass and a harder muon p_T spectrum. Since the number of expected events is only 0.34 for $M_{stau} = 200$ GeV, the three highest mass points are not studied any further in this work.

Λ [TeV]	M_{stau} [GeV]	Cross section [pb]	Exp. events comb. sel.	efficiency [%]
31	100	1.63	14.67	25.2
40	126	0.38	4.04	29.7
50	156	0.10	1.23	34.3
65	201	0.025	0.34	38.4

Table 5.12: Number of expected signal events and efficiencies after the combined final selection for different GMSB parameter points.

In the next chapter, the determination of systematic uncertainties is presented in order to obtain a meaningful measurement.

Chapter 6

Systematic Uncertainties

The experimental and theoretical uncertainties affecting the measurement of proton-proton collisions with highly ionizing and energetic muons are described in the following. First, general experimental uncertainties applied to both the signal and the background selection are introduced. Then, systematic effects on the signal selection are presented, followed by uncertainties on the SM background prediction. Uncertainties are estimated independently for each of the three final selections that were detailed in the previous chapter.

6.1 Experimental Uncertainties

These uncertainties are common to all selections and to both signal and background predictions.

Luminosity Measurement

As stated in Sec. 3.2.7, the uncertainty on the luminosity measurement in CMS for the 2010 LHC run was estimated to be 4 %.

Muon and Track Reconstruction

The uncertainty on the track reconstruction efficiency for isolated muons was found to be up to 2 % [50]. For the global muon reconstruction efficiency, the maximal difference between data and simulations was calculated to be 2.1 % [51]. The transverse momentum

resolution of muons is well described by simulations [51], therefore no additional systematic uncertainty on the muon momentum is assumed.

Muon Trigger

In a separate study [51], the muon trigger efficiency for single, isolated muons with $20 < p_T < 100$ GeV was found to differ by up to 5.1 ± 1.5 % between data and simulations. With a tag-and-probe method used on Drell-Yan di-muon events, the difference was up to 3.5 ± 0.4 %. The overall trigger efficiency found for these two event topologies was 90.8 and 92.4 %, respectively. Since the trigger efficiency for the signal, described in Sec. 5.1, is of similar value, the maximal discrepancy between data and simulation of 5 % is assumed for the trigger uncertainty for both signal and background.

6.2 Signal Prediction Uncertainties

Energy Loss Scale

The cuts on the track energy loss measurement have been varied up and down by 0.1 MeV/cm, equivalent to a relative change in scale of about 3 %. This results in quite a large difference in selection efficiency for the lowest stau mass but decreases for higher masses. This is attributed to the change in the dE/dx spectrum when keeping the p_T-cut unchanged since more staus are created with $p < M$, as explained in Sec. 5.1. The larger of the two selection differences from changed cuts on dE/dx (up or down by 0.1 MeV/cm) is chosen as systematic error for that sample and selection. All values from this study are given in Tab. 6.1. Note that due to the higher dE/dx cut value in the single-muon channel (4.2 MeV/cm), larger deviations are expected than for the multi-muon channel.

Jet Energy Scale

The uncertainty on the jet energy correction factors for Particle-Flow jets is at most 5 % at high values of pseudorapidity [39]. The influence of this uncertainty on the final selection has been tested by varying the cut on the jet transverse momentum. The regular cut of 30 GeV was increased and decreased by 1.5 GeV, and the resulting number of selected events for the low-mass signal sample is listed in Tab. 6.2. The largest deviation due to the changed cut value is about 3 % for the multi-muon dE/dx channel, whereas for the

		single μ, $dE/dx > 4.2$		2+ μ, $dE/dx > 3.5$	
M_{stau} [GeV]	dE/dx cuts	Expected	Sys. error	Expected	Sys. error
100	down 0.1	1.29	-13 %	3.20	-10 %
	regular	1.47	-	3.55	-
	up 0.1	1.71	+16 %	3.95	+11 %
126	down 0.1	0.54	-10 %	1.04	-5 %
	regular	0.60	-	1.09	-
	up 0.1	0.63	+6 %	1.15	+5 %
156	down 0.1	0.19	-9 %	0.39	-3 %
	regular	0.21	-	0.40	-
	up 0.1	0.22	+5 %	0.41	+3 %

Table 6.1: Numbers of expected signal events for the dE/dx final selections for different cuts on muon track energy loss. The "regular" cuts are $dE/dx > 4.2$ and $dE/dx > 3.5$ MeV/cm for the single- and multi-muon channels, respectively.

	single μ		2+ μ, dE/dx		2+ μ, p_T	
jet p_T [GeV]	Expected	Sys. error	Expected	Sys. error	Expected	Sys. error
> 28.5	1.48	+2 %	3.67	+3 %	9.69	+1 %
> 30.0	1.47	-	3.55	-	9.64	-
> 31.5	1.46	-1 %	3.46	-3 %	9.59	-1 %

Table 6.2: Numbers of expected signal events for the three final selections for different cuts on the jet transverse momentum. Relative deviations from the regular cut of 30 GeV are also given. The generated stau mass is 100 GeV.

other selections it is less than 2 %. The same is true for the higher-mass signal samples. This weak dependence on the jet momentum scale is due to the high average p_T of the two leading jets in the signal. To be conservative, a systematic error of 3 % due to the jet energy scale is assumed for all selections and signal samples.

Cross Section Uncertainties

Uncertainties on the signal cross section are determined by varying the renormalization scale μ and the parton density functions. The renormalization scale was adjusted by

M_{stau} [GeV]	Scale factor	Cross section [pb]	Sys. error
100	0.5	1.76	+8 %
	central	1.63	-
	2.0	1.47	-10 %
126	0.5	0.41	+8 %
	central	0.38	-
	2.0	0.35	-8 %
156	0.5	0.107	+7 %
	central	0.100	-
	2.0	0.094	-6 %

Table 6.3: Signal cross sections for lower ($\mu/2$), central, and higher (2μ) renormalization scales as calculated with Prospino2. Corresponding relative deviations are given.

factors of 1/2 and 2 in the calculation of NLO cross sections with Prospino2. Thus, three cross sections were obtained for each subprocess. The total cross section for each scale and the corresponding relative deviation from the central scale for the three signal samples are summarized in Tab. 6.3. The larger of the two variations is chosen as systematic error.

The variation of parton density functions (PDFs) was done by applying 22 different sets of PDFs from CTEQ6.6 [52] to the signal selections. For each PDF, two weights are determined for each event, one giving a higher weight than the central (default) PDF and the other giving a lower weight. For each final selection and set of PDFs, the half-difference between the lower and higher weights are summed up quadratically to obtain a total weight on an event-by-event basis [53]:

$$\Delta X = \frac{1}{2}\sqrt{\sum_{i=1}^{N}(X_i^+ - X_i^-)^2}, \tag{6.1}$$

where X is the event weight for the ith set of PDFs and N is the number of PDFs (in this case $N = 22$). Thus, for each selection a total weight ΔX is obtained that, when divided by the total central PDF weight, corresponds to a systematic uncertainty due to the variation of parton density functions. The resulting values for the three signal samples used in the final selection are summarized in Tab. 6.4.

	PDF uncertainties		
M_{stau} [GeV]	single μ	2+ μ, dE/dx	2+ μ, p_T
100	9 %	8 %	10 %
126	7 %	7 %	12 %
156	7 %	7 %	11 %

Table 6.4: Systematic uncertainties due to parton density functions for each final selection and signal sample.

6.3 Background Prediction Uncertainties

Energy Loss Prediction from Data

The uncertainties for the two dE/dx selections were determined in Sec. 5.5. For the single-muon channel the uncertainty is 24 %, whereas for the multi-muon channel it is 5 %.

Jet Energy Scale

The same procedure explained in Sec. 6.2 is applied to all background samples. Resulting deviations for the total background for each final selection are given in Tab. 6.5. For the high-momentum multi-muon channel, there is a very weak dependence on the jet energy scale because the jet p_T cut is very low in comparison to the muon p_T cut. The high total transverse energy in these events makes highly energetic jets much more likely than in the other two selections. For the single-muon channel, 8 % is taken as systematic uncertainty, and 5 % for the multi-muon dE/dx channel. These rather large values reflect the steep spectrum of transverse jet momenta shown in Fig. 5.14.

Cross Section Uncertainties

Theoretical cross sections for all background processes are given in Tab. 5.2. Uncertainties are given for all samples except for the QCD and low-mass Drell-Yan processes. In the final selections, the dominant remaining processes are $W \rightarrow l\nu$ with a relative theoretical uncertainty of 0.050, as well as the high-mass $Z/\gamma \rightarrow ll$ (0.043), and $t\bar{t}$ (0.155). Cross sections for these processes have been measured by CMS and were found to agree with the theoretical predictions [54, 55], justifying the use of the given theoretical uncertainties in

	single μ		2+ μ, dE/dx		2+ μ, p_T	
jet p_T [GeV]	Expected	Sys. error	Expected	Sys. error	Expected	Sys. error
> 28.5	0.121	+8 %	0.596	+5 %	0.406	+1 %
> 30.0	0.112	-	0.569	-	0.402	-
> 31.5	0.103	-8 %	0.539	-5 %	0.402	-0 %

Table 6.5: Numbers of expected background events for the three final selections for different cuts on the jet transverse momentum. Relative deviations from the regular cut of 30 GeV are also given.

Background	Cross section	Expected events		
process	uncertainty	single μ	2+ μ, dE/dx	2+ μ, p_T
$W \rightarrow l\nu$	0.050	0.07	0	0
$Z/\gamma \rightarrow ll$, $M_{ll} > 50$ GeV	0.043	0.02	0.25	0.28
$t\bar{t}$	0.155	0.02	0.15	0.25
N_{total}	-	0.11	0.40	0.53
$\delta(\sigma_{total})$	-	**0.07**	**0.10**	**0.11**

Table 6.6: Numbers of expected events of main background processes for the three final selections. Total cross section uncertainties $\delta(\sigma_{total})$ for each channel were calculated using Eq. 6.2.

this analysis. Other processes have negligible fractions of events in all selections and are not considered for the cross section uncertainties.

For each final selection, the uncertainties from the three main background processes are weighted according to the number of expected events in that selection to calculate the overall background uncertainty:

$$\delta\sigma_{total} = \sqrt{\frac{1}{N_{total}} \sum_i (\delta(\sigma_i))^2 \cdot N_i}, \tag{6.2}$$

where $\delta(\sigma_i)$ are the cross section uncertainties stated above and N_i are the numbers of expected events for the process i. N_{total} is the combined number of expected events from the three processes. Resulting uncertainties for the three final selections and corresponding event numbers are listed in Tab. 6.6. The calculated values are 7 % for the single-muon channel, and 10 and 11 % for the two multi-muon channels, respectively.

6.4 Total Systematic Errors

For each final selection, the uncertainties determined in the previous sections are added quadratically to obtain the total systematic errors for the background and the three signal samples. All values are given in Tab. 6.7. For the background, the error on the dE/dx fake rate from data dominates the total uncertainty on the single-muon selection. Beyond that, the cross section uncertainties are the main factors in the background systematics. For the signal, the variation of the dE/dx measurement is the dominant factor for the two dE/dx selections. For the high-momentum multi-muon selection, the PDF uncertainties give the largest contribution to the signal uncertainties.

Process	single μ	2+ μ, dE/dx	2+ μ, p_T
SM background	27 %	14 %	13 %
GMSB $M_{stau} = 100$ GeV	22 %	19 %	16 %
GMSB $M_{stau} = 126$ GeV	16 %	14 %	16 %
GMSB $M_{stau} = 156$ GeV	15 %	13 %	15 %

Table 6.7: Total systematic uncertainties for combined SM background and the analyzed GMSB signal points for the three final selections.

Chapter 7

Results

As described in Cha. 5, the selection of highly ionizing or energetic muons from 35.8 pb^{-1} of data yields no excess over the expected SM background. A GMSB model giving rise to quasi-stable stau leptons predicts signal-to-background ratios of $S/B \sim 10$ for a stau mass of 100 GeV and $S/B \sim 4$ for a stau mass of 126 GeV. Therefore, exclusion limits can be derived for these models. The three final selection channels, which are exclusive to each other (meaning that no two of these channels can select the same event), will be combined in the calculation of limits in order to obtain the best result.

For the determination of exclusion limits, a modified frequentist method [56] is used. It is detailed in App. A. Additionally, in order to treat systematic errors, a nuisance parameter is added to the Monte Carlo test statistics for the likelihood ratio $Q = L_{sb}/L_b$, where L_{sb} is the likelihood of a hypothesis that includes the signal and background, and L_b is the likelihood of a background-only hypothesis. Without systematic errors, the test statistics is a Poisson distribution centered around the number of measured events. The nuisance parameter has a value equal to the total systematic uncertainty which effectively modifies the Poissonian test statistics with a Gaussian whose width is just that systematic uncertainty multiplied with the number of expected events. The test statistics for signal and background are obtained by making a calculation of toy MC experiments (10,000 in this case) with the expected number of events as mean value and the corresponding systematic error as nuisance parameter.

The aforementioned steps are performed independently for all three selection channels, and the resulting likelihood ratios are multiplied in order to compute a combined ratio from which a confidence level limit can be obtained. The software implementation of this

	Data	SM MC		Stau M=100	
Final selection	Observed	Expected	Sys. error	Expected	Sys. error
1 μ, $dE/dx > 4.2$	1	0.11	27 %	1.47	22 %
2+ μ, $dE/dx > 3.5$	0	0.57	14 %	3.55	19 %
2+ μ, $p_T > 200$	0	0.40	13 %	9.64	16 %

Table 7.1: Numbers of observed and expected events and total systematic errors for simulations for the three final selections.

	Stau M=126		Stau M=156	
Final selection	Expected	Sys. error	Expected	Sys. error
1 μ, $dE/dx > 4.2$	0.60	16 %	0.21	15 %
2+ μ, $dE/dx > 3.5$	1.09	14 %	0.40	13 %
2+ μ, $p_T > 200$	2.34	16 %	0.61	15 %

Table 7.2: Numbers of expected events and total systematic errors for simulations for the three final selections.

whole procedure is included in the RooStats [57] extension of ROOT [42].

The nuisance parameters used for signal and background expectations are the systematic uncertainties determined in Cha. 6. Limits are calculated for the combination of the three final selections whose event yields and systematic errors are listed in Tab. 7.1 and 7.2.

For each signal sample, the cross section is multiplied with a factor in order to obtain the actual cross section for which the signal can be excluded at 95 % confidence level (CL). This factor is calculated iteratively during the limit computation. The resulting values for the combination of all three final selections are shown in Fig. 7.1. Thus, upper limits on the cross sections of the investigated GMSB models are given. These cross sections are compared to the signal cross sections from Tab. 5.1, which are also plotted in Fig. 7.1. The dashed lines in this figure are linear interpolations (on a logarithmic scale) between the data points. Those signal models for which the upper limit cross section lies below the theory prediction are excluded at 95 % CL.

With the data of the 2010 LHC proton-proton run, amounting to 35.8 pb^{-1}, the two GMSB models with $\Lambda = 31$ TeV and $\Lambda = 40$ TeV can be excluded. This corresponds to an exclusion of stable stau leptons with masses below 126 GeV.

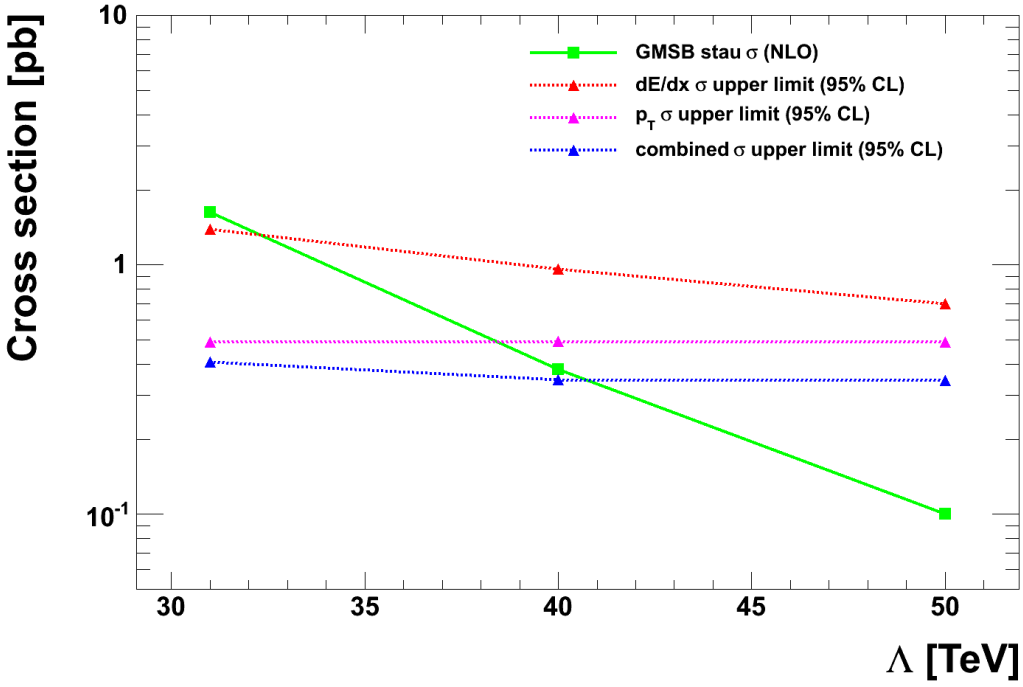

Figure 7.1: Signal cross section as a function of the GMSB parameter Λ. Calculated upper cross section limits at 95 % CL are compared to the theory prediction (green, solid). The combined limit is shown in dashed blue, the p_T-only limit in dashed magenta, and the dE/dx-only limit in dashed red.

The intersection of the cross section limit and the theory prediction for GMSB models with stable staus excludes values of Λ below 41 TeV, corresponding to stau masses roughly below 129 GeV. This estimate is to be taken with a grain of salt since the interpolation between the two signal points with $\Lambda = 40$ TeV and $\Lambda = 50$ TeV may not be accurate.

Additionally, to show the effect of combining a momentum-based analysis with an energy loss analysis, cross section limits were calculated only with the multi-muon p_T selection, and with a combination of the two dE/dx selections, respectively. The resulting limits are shown for comparison in Fig. 7.1. The p_T selection suffices to exclude the first signal point, as do the dE/dx selections, but for the point with $\Lambda = 40$ TeV, only the combination of all final selections results in an exclusion. Furthermore, the contribution of the dE/dx selections rises with higher SUSY mass scales, as evident by the larger slope of the dE/dx limit. This is due to the relative increase of slow staus with respect to energetic staus for the higher masses.

Chapter 8

Conclusion

A search for stable scalar tau leptons in gauge-mediated supersymmetry breaking (GMSB) was performed, analyzing the first proton-proton collisions produced at 7 TeV center-of-mass energy at the Large Hadron Collider. The data, corresponding to 35.8 pb^{-1}, were recorded with the CMS detector during the entire 2010 LHC run. Stable staus, resembling heavy muons, are expected to be found with high efficiency by muon triggers. Due to their high mass, stable staus may be slow-moving and deposit high ionization energy loss (dE/dx) in the silicon tracker, giving a unique signature for new particles. Furthermore, the mass of these particles could be directly calculated with the Bethe-Bloch formula (see Sec. 2.6).

In the analysis, events with at least one muon candidate were selected for high transverse momentum and high ionization energy loss in the silicon tracker, which are the main signatures expected from stable staus. Especially at low GMSB mass scales ($\Lambda = 31$ or 40 TeV), the production of squarks and gluinos is the dominant contribution to the signal cross section. Subsequent cascade decays of these heavy sparticles would lead to high jet and lepton multiplicities. Therefore, two or more hadronic jets were required. The background for the energy loss measurement was estimated by using a large sample of tracks from data, taking advantage of the fact that above momenta of a few GeV, no high energy loss is expected from any Standard Model particle. The search was divided into three disjoint final selections, depending on the muon multiplicity, and using either the transverse momentum or the energy loss measurement to improve the signal-to-background ratio. One data event passed the selection; it contains one selected muon with a momentum of $p = 69$ GeV and $dE/dx = 4.4$ MeV/cm, corresponding to a mass of 70 GeV. The

combination of the three search channels gave a SM background expectaction of 1.1 events. The analysis yielded no excess in the data over the expected Standard Model background. Signal expectations were 14.7 events for the GMSB model with a stau of 100 GeV, 4.0 events for the stau mass of 126 GeV, and 1.2 events for the stau mass of 156 GeV.

The final selection channels were combined in a calculation of upper limits on the GMSB cross sections. The final result is an exclusion of GMSB models in which stable staus with masses of 126 GeV or lower are expected. The full model parameters of the excluded point are:

$$N_{mess} = 3, \quad \Lambda = 40 \text{ TeV}, \quad M_{mess} = 80 \text{ TeV}, \quad \tan\beta = 10, \quad \mu > 0. \tag{8.1}$$

The squark and gluino masses are around 900 GeV in this model, as listed in Tab. B.2.

Previous experiments at the LEP collider have excluded stable staus with masses below 97.5 GeV [19].

The ATLAS collaboration has published a comparable result to the one presented here, using 37 pb^{-1} of data from the 2010 LHC run. They exclude stable staus with masses below 136 GeV [58], although in a slightly different GMSB model: $N_{mess} = 3$, $M_{mess} = 250$ TeV, $\tan\beta = 5$, $\mu > 0$. The Λ parameter was left unspecified.

In the meantime, the LHC has produced much more data in 2011, corresponding to more than 2.5 fb^{-1}. In an analysis of 1.09 fb^{-1}, the CMS collaboration has excluded stable staus with masses below 293 GeV, within the same model that was investigated in this study [59]. Thus, the GMSB model with $\Lambda = 85$ TeV, which was not accessible in the analysis presented here, has been excluded.

The two aforementioned analyses utilize the ionization energy loss measurement as well as the time-of-flight measured by muon detectors, thus increasing the sensitivity to slow-moving new particles. Using the time-of-flight measurement of muon candidates would be the next logical step for this analysis. Also, with a much larger amount of data, the precision of the dE/dx fake rate prediction could be greatly improved, especially at the high end of the dE/dx distribution (see Sec. 5.5). As shown in Sec. 5.6, other kinematic variables such as missing transverse energy and jet p_T could be used to further discriminate the signal from the background. Also, events with three muon candidates should be treated differently with more data, since this channel has a diminishing SM background even before requiring high dE/dx or p_T. The jet multiplicity cut should probably be relaxed, since for higher GMSB mass scales, the electroweak production channels (slepton pairs, and neutralino/chargino production) contribute more to the total cross section than the

QCD production channels. This leads to shorter cascades and smaller jet multiplicities in the signal. Pile-up is a much larger issue in the 2011 LHC collisions, since instantaneous luminosities in excess of $2 \cdot 10^{33}\text{cm}^{-2}\text{s}^{-1}$ have been reached. The signal simulation has to be adjusted accordingly. The isolation of tracks as well as the dE/dx measurement have to be re-evaluated for these data.

The main systematics to be improved in the signal selection is the dE/dx uncertainty. However, at higher stau masses, the dependence on the dE/dx measurement is already less pronounced, as described in Sec. 6.2. The uncertainties on the signal cross sections, being the renormalization scale and parton density functions, depend on external studies, meaning that the combined uncertainty of 10 to 15 % on the cross sections will probably be hard to reduce. For the background, the dE/dx prediction should be more precise with more data. Lowering the jet multiplicity requirement would reduce the dependence on the jet energy scale. Much like for the signal, the Standard Model cross section uncertainties would probably dominate the background systematics. Total systematic uncertainties of around 10 % seem feasible for both the signal and background expectations.

Finally, this analysis could be expanded to other GMSB models by varying the model parameters $\tan\beta$ and N_{mess}. The selection criteria could then be optimized for different signal topologies.

In conclusion, there are several possibilities for improving and expanding the search for stable staus. If the complications of high pile-up can be controlled during high-luminosity LHC running, which seems to be the case from the latest CMS results, this analysis should continue to provide a great search window for new physics.

Appendix A

CLs Method

The Modified Frequentist method [56] is commonly used in HEP experiments to compare likelihoods of different hypotheses[1].

In a counting experiment, the observed data (d) events, and the expected signal (s) and background (b) events are used to calculate a likelihood ratio $X(d)$ that discriminates signal-like outcomes from background-like outcomes:

$$X(d) = \frac{e^{-(s+b)}(s+b)^d}{d!}\left(\frac{e^{-b}b^d}{d!}\right)^{-1}. \tag{A.1}$$

In the case of n counting experiments (i.e. bins in a histogram or selection channels), the product of the individual ratios gives the total ratio,

$$X = \prod_{i=1}^{n} X_i. \tag{A.2}$$

This quantity is used to calculate the sum of Poisson probabilities of all possible numbers of observed events d_i' that have a likelihood ratio $X(d_i')$ that is equal to or smaller than the observed ratio $X(d_i)$, given by

$$\mathcal{P}_{s+b} = \sum_{X(d_i')\leq X(d_i)} \prod_{i=1}^{n} \frac{e^{-(s_i+b_i)}(s_i+b_i)^{d_i'}}{d_i'!}. \tag{A.3}$$

This probability is equal to the confidence level for excluding the simultaneous presence of signal and background,

$$CL_{s+b} = \mathcal{P}_{s+b}. \tag{A.4}$$

[1]The following passage is a revised excerpt from [60], Chapter 6.

The confidence level for the background-only hypothesis is calculated by only taking the background expectation into account in Equation (A.1), (A.2), and (A.3). The signal confidence level is then given by

$$CL_s = \frac{CL_{s+b}}{CL_b}, \tag{A.5}$$

so that the confidence level for excluding signal-like observations is

$$CL = 1 - \frac{\mathcal{P}_{s+b}}{\mathcal{P}_b}. \tag{A.6}$$

Appendix B

GMSB Mass Spectra

Sparticle	Mass [GeV]	Sparticle	Mass [GeV]
Sleptons		Higgs	
$\tilde{\tau}_1$	100	h^0	110
$\tilde{\tau}_2$	210	H^0	311
$\tilde{e}_R$, $\tilde{\mu}_R$	103	A^0	309
$\tilde{e}_L$, $\tilde{\mu}_L$	203	$H^\pm$	421
$\tilde{\nu}_{\tau,L}$, $\tilde{\nu}_{e,L}$, $\tilde{\nu}_{\mu,L}$	191	Gauginos	
Squarks		$\tilde{g}$	757
$\tilde{t}_1$	645	$\tilde{\chi}_1^0$	120
$\tilde{t}_2$	721	$\tilde{\chi}_2^0$	203
$\tilde{b}_1$	688	$\tilde{\chi}_3^0$	252
$\tilde{b}_2$	696	$\tilde{\chi}_4^0$	315
$\tilde{u}_R$, $\tilde{c}_R$	694	$\tilde{\chi}_1^\pm$	200
$\tilde{u}_L$, $\tilde{c}_L$	716	$\tilde{\chi}_2^\pm$	313
$\tilde{d}_R$, $\tilde{s}_R$	693	Gravitino	
$\tilde{d}_L$, $\tilde{s}_L$	721	$\tilde{G}$	$4.6 \cdot 10^{-6}$

Table B.1: Masses of physical SUSY particles of the GMSB point with $N_{mess} = 3$, $\Lambda = 31$ TeV, $M_{mess} = 62$ TeV, $\tan\beta = 10$, $\mu > 0$.

Sparticle	Mass [GeV]	Sparticle	Mass [GeV]
Sleptons		Higgs	
$\tilde{\tau}_1$	126	h^0	112
$\tilde{\tau}_2$	268	H^0	398
$\tilde{e}_R$, $\tilde{\mu}_R$	129	A^0	395
$\tilde{e}_L$, $\tilde{\mu}_L$	267	$H^\pm$	406
$\tilde{\nu}_{\tau,L}$, $\tilde{\nu}_{e,L}$, $\tilde{\nu}_{\mu,L}$	251	Gauginos	
Squarks		$\tilde{g}$	952
$\tilde{t}_1$	811	$\tilde{\chi}_1^0$	159
$\tilde{t}_2$	898	$\tilde{\chi}_2^0$	269
$\tilde{b}_1$	868	$\tilde{\chi}_3^0$	314
$\tilde{b}_2$	877	$\tilde{\chi}_4^0$	384
$\tilde{u}_R$, $\tilde{c}_R$	874	$\tilde{\chi}_1^\pm$	268
$\tilde{u}_L$, $\tilde{c}_L$	904	$\tilde{\chi}_2^\pm$	382
$\tilde{d}_R$, $\tilde{s}_R$	873	Gravitino	
$\tilde{d}_L$, $\tilde{s}_L$	908	$\tilde{G}$	$7.7 \cdot 10^{-6}$

Table B.2: Masses of physical SUSY particles of the GMSB point with $N_{mess} = 3$, $\Lambda = 40$ TeV, $M_{mess} = 80$ TeV, $\tan\beta = 10$, $\mu > 0$.

Sparticle	Mass [GeV]	Sparticle	Mass [GeV]
Sleptons		Higgs	
$\tilde{\tau}_1$	156	h^0	113
$\tilde{\tau}_2$	332	H^0	486
$\tilde{e}_R$, $\tilde{\mu}_R$	159	A^0	483
$\tilde{e}_L$, $\tilde{\mu}_L$	331	$H^\pm$	493
$\tilde{\nu}_{\tau,L}$, $\tilde{\nu}_{e,L}$, $\tilde{\nu}_{\mu,L}$	317	Gauginos	
Squarks		$\tilde{g}$	1,164
$\tilde{t}_1$	995	$\tilde{\chi}_1^0$	202
$\tilde{t}_2$	1,093	$\tilde{\chi}_2^0$	337
$\tilde{b}_1$	1,065	$\tilde{\chi}_3^0$	374
$\tilde{b}_2$	1,075	$\tilde{\chi}_4^0$	458
$\tilde{u}_R$, $\tilde{c}_R$	1,071	$\tilde{\chi}_1^\pm$	337
$\tilde{u}_L$, $\tilde{c}_L$	1,109	$\tilde{\chi}_2^\pm$	454
$\tilde{d}_R$, $\tilde{s}_R$	1,068	Gravitino	
$\tilde{d}_L$, $\tilde{s}_L$	1,112	$\tilde{G}$	$1.2 \cdot 10^{-5}$

Table B.3: Masses of physical SUSY particles of the GMSB point with $N_{mess} = 3$, $\Lambda = 50$ TeV, $M_{mess} = 100$ TeV, $\tan\beta = 10$, $\mu > 0$.

Sparticle	Mass [GeV]	Sparticle	Mass [GeV]
Sleptons		Higgs	
$\tilde{\tau}_1$	201	h^0	116
$\tilde{\tau}_2$	428	H^0	627
$\tilde{e}_R$, $\tilde{\mu}_R$	204	A^0	622
$\tilde{e}_L$, $\tilde{\mu}_L$	428	$H^\pm$	632
$\tilde{\nu}_{\tau,L}$, $\tilde{\nu}_{e,L}$, $\tilde{\nu}_{\mu,L}$	414	Gauginos	
Squarks		$\tilde{g}$	1,476
$\tilde{t}_1$	1,261	$\tilde{\chi}_1^0$	266
$\tilde{t}_2$	1,381	$\tilde{\chi}_2^0$	444
$\tilde{b}_1$	1,352	$\tilde{\chi}_3^0$	475
$\tilde{b}_2$	1,365	$\tilde{\chi}_4^0$	574
$\tilde{u}_R$, $\tilde{c}_R$	1,359	$\tilde{\chi}_1^\pm$	447
$\tilde{u}_L$, $\tilde{c}_L$	1,410	$\tilde{\chi}_2^\pm$	569
$\tilde{d}_R$, $\tilde{s}_R$	1,355	Gravitino	
$\tilde{d}_L$, $\tilde{s}_L$	1,412	$\tilde{G}$	$2.0 \cdot 10^{-5}$

Table B.4: Masses of physical SUSY particles of the GMSB point with $N_{mess} = 3$, $\Lambda = 65$ TeV, $M_{mess} = 130$ TeV, $\tan\beta = 10$, $\mu > 0$.

Sparticle	Mass [GeV]	Sparticle	Mass [GeV]
Sleptons		Higgs	
$\tilde{\tau}_1$	247	h^0	116
$\tilde{\tau}_2$	524	H^0	751
$\tilde{e}_R$, $\tilde{\mu}_R$	250	A^0	746
$\tilde{e}_L$, $\tilde{\mu}_L$	524	$H^\pm$	755
$\tilde{\nu}_{\tau,L}$, $\tilde{\nu}_{e,L}$, $\tilde{\nu}_{\mu,L}$	511	Gauginos	
Squarks		$\tilde{g}$	1,782
$\tilde{t}_1$	1,527	$\tilde{\chi}_1^0$	330
$\tilde{t}_2$	1,667	$\tilde{\chi}_2^0$	532
$\tilde{b}_1$	1,635	$\tilde{\chi}_3^0$	555
$\tilde{b}_2$	1,651	$\tilde{\chi}_4^0$	688
$\tilde{u}_R$, $\tilde{c}_R$	1,642	$\tilde{\chi}_1^\pm$	537
$\tilde{u}_L$, $\tilde{c}_L$	1,705	$\tilde{\chi}_2^\pm$	680
$\tilde{d}_R$, $\tilde{s}_R$	1,637	Gravitino	
$\tilde{d}_L$, $\tilde{s}_L$	1,707	$\tilde{G}$	$3.1 \cdot 10^{-5}$

Table B.5: Masses of physical SUSY particles of the GMSB point with $N_{mess} = 3$, $\Lambda = 80$ TeV, $M_{mess} = 160$ TeV, $\tan\beta = 10$, $\mu > 0$.

Sparticle	Mass [GeV]	Sparticle	Mass [GeV]
Sleptons		Higgs	
$\tilde{\tau}_1$	308	h^0	118
$\tilde{\tau}_2$	652	H^0	930
$\tilde{e}_R$, $\tilde{\mu}_R$	312	A^0	924
$\tilde{e}_L$, $\tilde{\mu}_L$	652	$H^\pm$	933
$\tilde{\nu}_{\tau,L}$, $\tilde{\nu}_{e,L}$, $\tilde{\nu}_{\mu,L}$	639	Gauginos	
Squarks		$\tilde{g}$	2,182
$\tilde{t}_1$	1,870	$\tilde{\chi}_1^0$	415
$\tilde{t}_2$	2,041	$\tilde{\chi}_2^0$	663
$\tilde{b}_1$	2,004	$\tilde{\chi}_3^0$	681
$\tilde{b}_2$	2,025	$\tilde{\chi}_4^0$	845
$\tilde{u}_R$, $\tilde{c}_R$	2,013	$\tilde{\chi}_1^\pm$	671
$\tilde{u}_L$, $\tilde{c}_L$	2,094	$\tilde{\chi}_2^\pm$	835
$\tilde{d}_R$, $\tilde{s}_R$	2,006	Gravitino	
$\tilde{d}_L$, $\tilde{s}_L$	2,095	$\tilde{G}$	$4.8 \cdot 10^{-5}$

Table B.6: Masses of physical SUSY particles of the GMSB point with $N_{mess} = 3$, $\Lambda = 100$ TeV, $M_{mess} = 200$ TeV, $\tan\beta = 10$, $\mu > 0$.

List of Figures

2.1 Feynman diagram of the muon decay at leading order. 7

2.2 Feynman diagrams of fermion and boson loop corrections. 12

2.3 Feynman diagrams of e^+e^- interactions: annihilation (left) and scattering (right) at lowest order. Time advances from left to right. 14

2.4 Parton distribution functions versus momentum fraction x at $Q^2 = 10$ GeV^2 (left) and 10^4 GeV^2 (right) with one-sigma uncertainties. Gluon PDFs are downscaled by a factor of 10 for visibility. From [6]. 16

2.5 Relationship between momentum transfer Q^2 and momentum fraction x and corresponding mass M of particles produced at rapidity y. The range of the LHC at $\sqrt{s} = 14$ TeV is shown in blue and compared to HERA and fixed target kinematics. From [7]. 17

2.6 Standard Model cross sections and event rates in proton-(anti-)proton collisions as a function of the center-of-mass energy $\sqrt{s}$. The LHC intersect corresponds to $\sqrt{s} = 14$ TeV. From [7]. 18

2.7 Feynman diagrams of quark-antiquark production at leading order at the LHC. 19

2.8 Next-to-lightest SUSY particle in GMSB as a function of $N_5 = N_{mess}$ and $M = M_{mess}$. The transition between the scenarios also depends on $\tan\beta$, as shown by the three solid lines corresponding to $\tan\beta = 3$, 10, 30. From [15]. 24

2.9 Next-to-lightest SUSY particles in GMSB: four possible scenarios and their ranges in the Λ-$\tan\beta$ plane are shown. Colored boxes correspond to fixed values of N_{mess}: red: $N_{mess} = 1$; green: $N_{mess} = 2$; blue: $N_{mess} = 3$; yellow: $N_{mess} = 4$. Scenarios A and D are not allowed for $N_{mess} = 4$, scenario C is not realized for $N_{mess} = 1$. From [15]. 25

2.10 Muon stopping-power ($-dE/dx$) of copper as a function of $\beta\gamma = pM/c$ and momentum. Taken from [2]. 28

3.1 Schematic overview of the LHC and its pre-accelerators. 30

3.2 Day-by-day luminosity in 2010: delivered by LHC and recorded by CMS (left) and maximum instantaneous luminosity in CMS (right). 31

3.3 Schematic view of the CMS detector. [21] 32

3.4 Schematic view of the silicon tracker in the r-z-plane. [21, 22] Each line represents a silicon module. Double lines represent double-sided strip modules. 34

3.5 Schematic view of one-quarter of the electromagnetic calorimeter in the y-z-plane. [22] 36

3.6 Schematic view of one-quarter of the hadronic calorimeter in the y-z-plane. The numbers denote tower and layer indices. [21] 38

3.7 Jet transverse energy resolution as a function of transverse energy from simulated dijet events. Jets from three pseudorapidity regions are plotted. [22] 39

3.8 Schematic view of the muon system in the r-z-plane. Only the positive-z half is shown. [22] 41

3.9 Momentum resolution as a function of momentum for muons in a central (left) and a forward (right) region of the CMS detector. Results are shown for tracks from the tracker (green), muon system (blue), and both detectors combined (red). [22] 42

4.1 Total jet energy correction factors as a function of p_T for different values of η (top) and as a function of η for different values of p_T (bottom). Distributions for calorimeter, JPT, and Particle-Flow jets and their uncertainties are shown for jets reconstructed with the anti-k$_T$ algorithm. From [39]. . . 51

5.1 Feynman graph of a stau production process in GMSB via gluon fusion. Only one cascade branch is shown. 54

5.2 Generated stau transverse momentum (left) and speed (right) for three GMSB parameter points. 55

5.3 Fraction of signal events with at least one muon trigger object ($p_T \geq 9$ GeV) matched to a muon candidate that was matched to a generated stau four-vector, as a function of the generated stau transverse momentum. Three GMSB parameter points are shown. 56

5.4 Leading-order Feynman diagrams of main SM background processes: single W production (left), Drell-Yan muon-pair production (center), top-pair production (right). 57

5.5 Control selection: number of reconstructed primary vertices (left) and number of degrees of freedom, n_{dof}, of the primary vertex with the best vertex fit (right). The signal simulation does not include pile-up. 62

5.6 Relative isolation of muon candidates for the control selection without cuts on I_{rel} and jet multiplicity (see text for details). 63

5.7 Energy loss measurements for isolated muons (black dots) compared with non-isolated muons (magenta line) from collision data. Distributions are normalized to unity for comparison. Note that much larger statistics are shown compared to the control selection (see text for details). 64

5.8 Distribution of minimal ΔR between selected muon candidates and selected jets for the control selection without cuts on ΔR and jet multiplicity (see text for details). 65

5.9 Number of selected jets for the control selection without the cut on jet multiplicity. 66

5.10 Control selection: number of selected muons per event. 67

5.11 Control selection: transverse momentum distribution of selected muons. . . 68

5.12 Control selection: global muon track distributions of pseudorapidity (top left), azimuthal angle (top right), longitudinal (center left) and transverse (center right) impact parameters, track fit quality χ^2/n_{dof} (bottom left), and total number of hits (bottom right). 69

5.13 Control selection: distribution of track energy loss per unit length (dE/dx) of selected muons. 70

5.14 Control selection: distributions of selected jet multiplicity (top left), transverse momentum (top right), pseudorapidity (bottom left), and azimuthal angle (bottom right). 71

5.15 Control selection: distribution of ΔR between selected muon candidates and selected jets. A cut of $\Delta R > 0.5$ was applied. 72

5.16 Control selection: distribution of missing transverse energy. 73

5.17 Control selection: distributions of invariant mass of opposite sign (OS) muon pairs with (left) and without (right) Z-boson rejection. 74

5.18 dE/dx cut efficiencies (fake rates) in bins of transverse momentum of muon tracks from data, SM, and signal simulations. The rightmost bin contains all muon tracks with $p_T > 50$ GeV. Results for dE/dx cuts of 3.5 (left) and 4.2 MeV/cm (right) are shown. For comparison, the y-axis ranges are identical. The generated stau mass in the signal is 100 GeV. 76

5.19 Distribution of energy loss per unit length (dE/dx) of muons with $20 < p_T < 35$ GeV for data and SM MC. An exponential function, $y = C \cdot e^{-S \cdot x}$, was fit to the data from 3.5 to 5.0 MeV/cm. (See text for more details.) . . 77

5.20 Simulated dE/dx fake rates are shown as a function of transverse momentum of simulated muon tracks. Background (SM) is compared to the sum of signal and background to visualize the effect of possible signal contamination. The rightmost bin contains all muon tracks with $p_T > 50$ GeV. Results for dE/dx cuts of 3.5 (left) and 4.2 MeV/cm (right) are shown. The generated stau mass in the signal is 100 GeV. 79

5.21 Control selection for single-muon events: muon dE/dx versus transverse momentum distribution for data (top left), combined SM background (top right), and signal (bottom left) are shown. (Note the different z-axis scales.) The muon p_T distribution for all samples is shown in the bottom right plot. 84

5.22 Signal efficiency versus purity for events with one selected muon for a range of muon track dE/dx cuts from 3.4 to 4.3 MeV/cm. Values are calculated with respect to the single-muon control selection. The generated stau mass is 100 GeV. 85

5.23 Single-muon final selection: distribution of inner track energy loss per unit length (dE/dx) of muons after a cut of $dE/dx > 4.2$ MeV/cm. The background prediction was estimated from data in Sec. 5.5. 86

5.24 Single-muon final selection: distributions of muon p_T (top left), number of jets (top right), jet p_T (bottom left), and missing transverse energy (bottom right) are shown. The SM backgrounds have been reweighted for the dE/dx cut of 4.2 MeV/cm (see Sec. 5.5). 87

5.25 Control selection for events with two or more muons: muon dE/dx versus transverse momentum distributions are shown for data (top left), combined SM background (top right), and signal (bottom left). (Note the different z-axis scales.) The muon p_T distribution for all samples is shown in the bottom right plot. 88

5.26 Multi-muon p_T final selection: selected muon transverse momentum distribution. The *leading muon* is required to have $p_T > 200$ GeV. Zero data events pass this selection. 89

5.27 Multi-muon p_T final selection: distribtions of selected muons (top left), number of jets (top right), jet p_T (bottom left), and missing transverse energy (bottom right) are shown. The *leading muon* is required to have $p_T > 200$ GeV. Zero data events pass this selection. 91

5.28 Signal efficiency versus purity for events with two or more selected muons with varying dE/dx cuts required for at least one muon. Values are calculated with respect to the multi-muon control selection. The generated stau mass is 100 GeV. 92

5.29 Multi-muon dE/dx final selection: selected muon transverse momentum distribution. At least *one muon* was required to have $dE/dx > 3.5$ MeV/cm. The SM backgrounds have been reweighted for this dE/dx cut (see Sec. 5.5). *All muons* were required to have $p_T < 200$ GeV. 93

5.30 Multi-muon dE/dx final selection: distributions of selected muons (top left), number of jets (top right), jet p_T (bottom left), and missing transverse energy (bottom right) are shown. At least *one muon* was required to have $dE/dx > 3.5$ MeV/cm. The SM backgrounds have been reweighted for this dE/dx cut (see Sec. 5.5). *All muons* were required to have $p_T < 200$ GeV. Zero data events pass this selection. 94

7.1 Signal cross section as a function of the GMSB parameter Λ. Calculated upper cross section limits at 95 % CL are compared to the theory prediction (green, solid). The combined limit is shown in dashed blue, the p_T-only limit in dashed magenta, and the dE/dx-only limit in dashed red. 107

List of Tables

2.1 Weak isospin I_3 of Standard Model fermions. Antiparticles have opposite values of isospin. 8

2.2 Particle content of the Standard Model. All numbers taken from [2]. 10

2.3 Supermultiplets of the MSSM. 20

2.4 Masses of physical SUSY particles of the GMSB point with $N_{mess} = 3$, $\Lambda = 40$ TeV, $M_{mess} = 80$ TeV, $\tan\beta = 10$, $\mu > 0$. 26

5.1 Simulated signal samples by stau mass with the corresponding cross section, number of expected events for 35.8 pb^{-1}, and source of cross section calculation. Full mass spectra can be found in App. B. 58

5.2 Simulated Standard Model processes with theoretical cross sections (and errors where available) and the source of their calculation. 59

5.3 Complete list of control selection criteria for considered physics objects. . . 61

5.4 Control selection event yields for SM samples and 35.8 pb^{-1} of proton-proton collision data. 75

5.5 Data-driven dE/dx fake rates f_B for given dE/dx cut values. Muon tracks with transverse momenta in the ranges given in the third column were used for the fits. Also listed are the corresponding dE/dx cut efficiencies ϵ_S for the signal with the stau mass of 100 GeV, and the ratio ϵ_S/f_B. 80

5.6 Data-driven dE/dx fake rates corrected for signal contamination (with statistical errors) and systematic uncertainties for dE/dx cut values chosen for the final selection. 81

5.7 Number of observed and expected events and expected signal-to-background ratio for single-muon and multi-muon events after the control selection. Event numbers correspond to 35.8 pb^{-1} of CMS data. 82

5.8 Single-muon final selection criteria. The selection of physics objects is detailed in Tab. 5.3. 83
5.9 Multi-muon p_T final selection criteria. The selection of physics objects is detailed in Tab. 5.3. 90
5.10 Multi-muon dE/dx final selection criteria. The selection of physics objects is detailed in Tab. 5.3. 92
5.11 Number of observed and expected events and expected signal-to-background ratio for the three final selections. The summation of the three selections gives the "Total combined" event numbers given in the lower row. 95
5.12 Number of expected signal events and efficiencies after the combined final selection for different GMSB parameter points. 96

6.1 Numbers of expected signal events for the dE/dx final selections for different cuts on muon track energy loss. The "regular" cuts are $dE/dx > 4.2$ and $dE/dx > 3.5$ MeV/cm for the single- and multi-muon channels, respectively. 99
6.2 Numbers of expected signal events for the three final selections for different cuts on the jet transverse momentum. Relative deviations from the regular cut of 30 GeV are also given. The generated stau mass is 100 GeV. 99
6.3 Signal cross sections for lower ($\mu/2$), central, and higher (2μ) renormalization scales as calculated with Prospino2. Corresponding relative deviations are given. 100
6.4 Systematic uncertainties due to parton density functions for each final selection and signal sample. 101
6.5 Numbers of expected background events for the three final selections for different cuts on the jet transverse momentum. Relative deviations from the regular cut of 30 GeV are also given. 102
6.6 Numbers of expected events of main background processes for the three final selections. Total cross section uncertainties $\delta(\sigma_{total})$ for each channel were calculated using Eq. 6.2. 102
6.7 Total systematic uncertainties for combined SM background and the analyzed GMSB signal points for the three final selections. 103

7.1 Numbers of observed and expected events and total systematic errors for simulations for the three final selections. 106

7.2 Numbers of expected events and total systematic errors for simulations for the three final selections. 106

B.1 Masses of physical SUSY particles of the GMSB point with $N_{mess} = 3$, $\Lambda = 31$ TeV, $M_{mess} = 62$ TeV, $\tan\beta = 10$, $\mu > 0$. 115
B.2 Masses of physical SUSY particles of the GMSB point with $N_{mess} = 3$, $\Lambda = 40$ TeV, $M_{mess} = 80$ TeV, $\tan\beta = 10$, $\mu > 0$. 116
B.3 Masses of physical SUSY particles of the GMSB point with $N_{mess} = 3$, $\Lambda = 50$ TeV, $M_{mess} = 100$ TeV, $\tan\beta = 10$, $\mu > 0$. 117
B.4 Masses of physical SUSY particles of the GMSB point with $N_{mess} = 3$, $\Lambda = 65$ TeV, $M_{mess} = 130$ TeV, $\tan\beta = 10$, $\mu > 0$. 118
B.5 Masses of physical SUSY particles of the GMSB point with $N_{mess} = 3$, $\Lambda = 80$ TeV, $M_{mess} = 160$ TeV, $\tan\beta = 10$, $\mu > 0$. 119
B.6 Masses of physical SUSY particles of the GMSB point with $N_{mess} = 3$, $\Lambda = 100$ TeV, $M_{mess} = 200$ TeV, $\tan\beta = 10$, $\mu > 0$. 120

Acknowledgements

This work would not have been possible without the support of many colleagues, friends, and family.

First, I would like to thank Prof. Dr. Peter Schleper for giving me the opportunity to be part of his wonderful group at University of Hamburg. He has been closely involved in my work since the beginning of my diploma thesis in 2007. His ideas and guidance have helped me keep track along the way. It was due to his excitement and passion for particle physics that I chose to work in this field, and I have never regretted that decision.

The supervisors of my work at University of Hamburg were Dr. Gero Flucke, Dr. Martin Weber, and Dr. Gordon Kaussen. I would like to thank them for the many discussions on physics and technical things that gave me an understanding of what it takes to be a particle physics scientist. A special thanks goes to Gordon who proof-read most of this manuscript and gave me valuable feedback for the analysis.

Furthermore, I am indebted to Dr. Christian Autermann and Dr. Christian Sander who cast a critical eye on my work and supported me with their expertise on searches for new physics.

To my partners in crime since the beginning, Dr. Jula Draeger and Jan Thomsen, you are friends first and then colleagues. An era comes to a close - I wish you all the best on your new endeavors.

To Dr. Sebastian Naumann-Emme, through our discussions across the table in our office, I've learned more about particle physics from you than anyone else in our group. All the best to you and your family.

To the whole group at University of Hamburg during the last four years, thanks for being part of lunch discussions, poker rounds, conference trips, and of course DPG rehearsals.

Finally, to my parents, Isa and Rainer, who have given me the best support imaginable, giving me the opportunity to comfortably focus on my work. I am gracious to you forever.

Bibliography

[1] B. R. Martin and G. Shaw, "Particle Physics". John Wiley & Sons, 1997.

[2] K. Nakamura et al (Particle Data Group), "Review of Particle Physics", *J. Phys. G: Nucl. Part. Phys.* **37** (2010) 075021.

[3] C. Berger, "Elementarteilchenphysik". Springer, 2002.

[4] **ALEPH, DELPHI, L3, and OPAL** Collaboration, The LEP Working Group for Higgs Boson Searches, "Search for the Standard Model Higgs Boson at LEP", *Phys. Lett.* **B565** (2003) 61–75, arXiv:hep-ex/0306033. doi:10.1016/S0370-2693(03)00614-2.

[5] **CDF and D0** Collaboration, T. Aaltonen et al., "Combined CDF and D0 Upper Limits on Standard Model Higgs Boson Production with up to 8.2 fb^{-1} of Data", arXiv:1103.3233.

[6] A. D. Martin, W. J. Stirling, R. S. Thorne et al., "Parton distributions for the LHC", *Eur. Phys. J.* **C63** (2009) 189–285, arXiv:0901.0002. doi:10.1140/epjc/s10052-009-1072-5.

[7] J. M. Campbell, J. W. Huston, and W. J. Stirling, "Hard Interactions of Quarks and Gluons: A Primer for LHC Physics", *Rept. Prog. Phys.* **70** (2007) 89, arXiv:hep-ph/0611148. doi:10.1088/0034-4885/70/1/R02.

[8] J. Wess and B. Zumino, "A Lagrangian Model Invariant Under Supergauge Transformations", *Phys. Lett.* **B49** (1974) 52. doi:10.1016/0370-2693(74)90578-4.

[9] J. Wess and B. Zumino, "Supergauge Transformations in Four-Dimensions", *Nucl. Phys.* **B70** (1974) 39–50. doi:10.1016/0550-3213(74)90355-1.

[10] S. Ferrara, J. Wess, and B. Zumino, "Supergauge Multiplets and Superfields", *Phys. Lett.* **B51** (1974) 239. doi:10.1016/0370-2693(74)90283-4.

[11] **MSSM Working Group** Collaboration, A. Djouadi et al., "The Minimal Supersymmetric Standard Model: Group Summary Report", arXiv:hep-ph/9901246.

[12] S. P. Martin, "A Supersymmetry Primer", arXiv:hep-ph/9709356.

[13] G. F. Giudice and R. Rattazzi, "Theories with Gauge-Mediated Supersymmetry Breaking", *Phys. Rept.* **322** (1999) 419–499, arXiv:hep-ph/9801271. doi:10.1016/S0370-1573(99)00042-3.

[14] J. A. Bagger, K. T. Matchev, D. M. Pierce et al., "Weak-Scale Phenomenology of Models with Gauge-Mediated Supersymmetry Breaking", *Phys. Rev.* **D55** (1997) 3188–3200, arXiv:hep-ph/9609444. doi:10.1103/PhysRevD.55.3188.

[15] S. Ambrosiano, "Gauge-Mediated Supersymmetry Breaking Models and the Linear Collider". Physics and Detectors for a Linear e^+e^- Collider: 2nd Workshop, Lund, Sweden, June 28-30, 1998.

[16] B. C. Allanach et al., "The Snowmass Points and Slopes: Benchmarks for SUSY Searches", *Eur. Phys. J.* **C25** (2002) 113–123, arXiv:hep-ph/0202233. doi:10.1007/s10052-002-0949-3.

[17] The CMS Collaboration, "Search for Heavy Stable Charged Particles in pp Collisions at $\sqrt{s} = 7$ TeV", *CMS-PAS-EXO-10-022* (2011).

[18] M. Fairbairn et al., "Stable Massive Particles at Colliders", *Phys. Rept.* **438** (2007) 1–63, arXiv:hep-ph/0611040. doi:10.1016/j.physrep.2006.10.002.

[19] LEPSUSYWG, "LEPSUSYWG/02-09.2". http://lepsusy.web.cern.ch/lepsusy/www/gmsb_summer02/lepgmsb.html.

[20] L. Evans (ed.) and P. Bryant (ed.), "LHC Machine", *JINST* **3:S08001** (2008). doi:10.1088/1748-0221/3/08/S08001.

[21] The CMS Collaboration, "The CMS Experiment at the CERN LHC", *J. Instrum.* **3:S08004** (2008).

[22] The CMS Collaboration, "CMS Physics Technical Design Report Volume I: Detector Performance and Software". CERN, Geneva.

[23] "Electromagnetic Calorimeter Commissioning and First Results with 7 TeV Data", Technical Report CERN-CMS-NOTE-2010-012, CERN, Geneva, July, 2010.

[24] The CMS Collaboration, "CMS TriDAS project: Technical Design Report. Volume 1, The Trigger Systems". Technical Design Report CMS.

[25] T. Virdee, A. Petrilli, and A. Ball, "CMS High Level Trigger", Technical Report LHCC-G-134. CERN-LHCC-2007-021, CERN, Geneva, June, 2007.

[26] The CMS Collaboration, "Measurement of CMS Luminosity", *CMS-PAS-EWK-10-004* (2010).

[27] S. van der Meer, "Calibration of the Effective Beam Height in the ISR", Technical Report CERN-ISR-PO-68-31, CERN, Geneva, 1968.

[28] The CMS Collaboration, "Absolute luminsosity normalization", *CMS-DPS-2011-002* (2011).

[29] T. Sjostrand, S. Mrenna, and P. Z. Skands, "PYTHIA 6.4 Physics and Manual", *JHEP* **05** (2006) 026, arXiv:hep-ph/0603175. doi:10.1088/1126-6708/2006/05/026.

[30] F. Maltoni and T. Stelzer, "MadEvent: Automatic Event Generation with MadGraph", *JHEP* **02** (2003) 027, arXiv:hep-ph/0208156.

[31] F. E. Paige, S. D. Protopopescu, H. Baer et al., "ISAJET 7.69: A Monte Carlo Event Generator for p p, anti-p p, and e+ e- Reactions", arXiv:hep-ph/0312045.

[32] **GEANT4** Collaboration, S. Agostinelli et al., "GEANT4: A simulation toolkit", *Nucl. Instrum. Meth.* **A506** (2003) 250–303. doi:10.1016/S0168-9002(03)01368-8.

[33] W. Adam, B. Mangano, T. Speer et al., "Track Reconstruction in the CMS Tracker", Technical Report CERN-CMS-NOTE-2006-041, CERN, Geneva, Dec, 2006.

[34] A. Giammanco, "Particle Identification with Energy Loss in the CMS Silicon Strip Tracker", Technical Report CMS-NOTE-2008-005. CERN-CMS-NOTE-2008-005, CERN, Geneva, June, 2007.

[35] The CMS Collaboration, "Performance of CMS Muon Reconstruction in Cosmic-Ray Events", *J. Instrum.* **5** (Nov, 2009) T03022. 47 p.

[36] M. Cacciari, G. P. Salam, and G. Soyez, "The anti-k_t jet clustering algorithm", *JHEP* **04** (2008) 063, arXiv:0802.1189. doi:10.1088/1126-6708/2008/04/063.

[37] The CMS Collaboration, "Commissioning of the Particle-Flow Reconstruction in Minimum-Bias and Jet Events from pp Collisions at 7 TeV", *CMS-PAS-PFT-10-002* (2010).

[38] The CMS Collaboration, "Jet Performance in pp Collisions at 7 TeV", *CMS-PAS-JME-10-003* (2010).

[39] The CMS Collaboration, "Determination of the Jet Energy Scale in CMS with pp Collisions at $\sqrt{s} = 7$ TeV", *CMS-PAS-JME-10-010* (2010).

[40] The CMS Collaboration, "Plans for Jet Energy Corrections at CMS", *CMS-PAS-JME-07-002* (2008).

[41] The CMS Collaboration, "Missing Transverse Energy Performance in Minimum-Bias and Jet Events from Proton-Proton Collisions at $\sqrt{s} = 7$ TeV", *CMS-PAS-JME-10-004* (2010).

[42] R. Brun and F. Rademakers, "ROOT: An object oriented data analysis framework", *Nucl. Instrum. Meth.* **A389** (1997) 81–86. doi:10.1016/S0168-9002(97)00048-X.

[43] W. Beenakker, R. Hopker, M. Spira et al., "Squark and Gluino Production at Hadron Colliders", *Nucl. Phys.* **B492** (1997) 51–103, arXiv:hep-ph/9610490. doi:10.1016/S0550-3213(97)00084-9.

[44] W. Beenakker et al., "The Production of Charginos/Neutralinos and Sleptons at Hadron Colliders", *Phys. Rev. Lett.* **83** (1999) 3780–3783, arXiv:hep-ph/9906298. doi:10.1103/PhysRevLett.83.3780.

[45] J. M. Campbell and R. K. Ellis, "MCFM for the Tevatron and the LHC", *Nucl. Phys. Proc. Suppl.* **205-206** (2010) 10–15, arXiv:1007.3492. doi:10.1016/j.nuclphysbps.2010.08.011.

[46] K. Melnikov and F. Petriello, "Electroweak gauge boson production at hadron colliders through $O(\alpha_s^2)$", *Phys. Rev.* **D74** (2006) 114017, arXiv:hep-ph/0609070. doi:10.1103/PhysRevD.74.114017.

[47] The CMS Collaboration, "Performance of Muon Identification in pp Collisions at $\sqrt{s} = 7$ TeV", *CMS-PAS-MUO-10-002* (2010).

[48] The CMS Collaboration, "Tracking and Primary Vertex Results in First 7 TeV Collisions", *CMS-PAS-TRK-10-005* (2010).

[49] T. Speer, K. Prokofiev, R. Fruehwirth et al., "Vertex Fitting in the CMS Tracker", Technical Report CMS-NOTE-2006-032, CERN, Geneva, Feb, 2006.

[50] The CMS Collaboration, "Measurement of Tracking Efficiency", *CMS-PAS-TRK-10-002* (2010).

[51] The CMS Collaboration, "Performance of Muon Reconstruction and Identification in pp Collisions at $\sqrt{s} = 7$ TeV", *CMS-PAS-MUO-10-004* (2010).

[52] P. M. Nadolsky et al., "Implications of CTEQ global analysis for collider observables", *Phys. Rev.* **D78** (2008) 013004, arXiv:0802.0007. doi:10.1103/PhysRevD.78.013004.

[53] D. Bourilkov, R. C. Group, and M. R. Whalley, "LHAPDF: PDF use from the Tevatron to the LHC", arXiv:hep-ph/0605240.

[54] The CMS Collaboration, "Measurements of Inclusive W and Z Cross Sections in pp Collisions at $\sqrt{s} = 7$ TeV.",.

[55] The CMS Collaboration, "First Measurement of the Cross Section for Top-Quark Pair Production in Proton-Proton Collisions at $\sqrt{s} = 7$ TeV.", *Phys. Lett. B* **695** (Oct, 2010) 424–443. 26 p.

[56] T. Junk, "Confidence Level Computation for Combining Searches with Small Statistics", *Nucl. Instrum. Meth.* **A434** (1999) 435–443, arXiv:hep-ex/9902006. doi:10.1016/S0168-9002(99)00498-2.

[57] D. Piparo, G. Schott, and G. Quast, "RooStatsCms: a tool for analysis modelling, combination and statistical studies", *J. Phys. Conf. Ser.* **219** (2010) 032034, arXiv:0905.4623. doi:10.1088/1742-6596/219/3/032034.

[58] **ATLAS** Collaboration, G. Aad et al., "Search for Heavy Long-Lived Charged Particles with the ATLAS Detector in pp Collisions at $\sqrt{s} = 7$ TeV", arXiv:1106.4495.

[59] The CMS Collaboration, "Search for Heavy Stable Charged Particles in pp Collisions at $\sqrt{s} = 7$ TeV", *CMS-PAS-EXO-11-022* (2011).

[60] K. Kaschube, "Search for Gravitino Production in R-Parity Violating Supersymmetry at HERA", *Diploma Thesis* (2007).